

**Luminescent properties of  $Y_3(Al, Ga)_5O_{12}:Tb$   
thin films**

by

**Abdelrhman Yousif Mohmmmed Ahmed  
(MSc)**

A thesis submitted in fulfilment of requirement for the degree

**PHILOSOPHIAE DOCTOR**

in the

**Faculty of Natural and Agricultural Sciences**

**Department of Physics**

at the

**University of the Free State**

**Promoter: Prof. H.C. Swart**

**Co-Promoter: Prof. O.M. Ntwaeaborwa**

June 2014

## Acknowledgements

I would like to thank the Almighty Allah for everything that he has given to me, for his blessing and guidance to finish this work. I would also like to thank the following individuals and institutions:

- Prof H.C. Swart for being the best promoter and for his professional guidance ever and for giving me the freedom to do what I needed to do, I greatly appreciate his suggestions and assistance in this project. Prof, thanks for the great role that you played for securing funds for my study program. Prof, I would like to tell you that, I have learned a lot on technical aspects of research from you and I like the way you lead the group as a family.
- Special thanks to Prof O.M. Ntwaeaborwa for being my co-promoter and for his efforts to assisting me.
- My special thanks go to Dr Jaafer Mohamed Diab the dean of the Faculty of Education University of Khartoum for his support to help me start my PhD study.
- Thanks to Dr Fadlallah M. Hamouda, the head of the Physics Department, University of Khartoum, Faculty of Education.
- I would like to thanks Mrs Islah Shaban the deputy of the director of the Teaching Assistants Administration.
- I thank my colleague Dr Seed Ahmed HAA for introducing me to phosphors, and for his fruitful discussions.
- I would like to thank my colleague Mr Mubarak Yagoub for his assistance in Latex.
- Special thanks to Dr Omer AbdulAziz and his family (his wife Osila and his kids Reem and Abdul Malik) for their assistance.

- 
- Special thanks to Mr Raphael Nyenge for carefully reading the manuscript.
  - I thank all staff members of the Department of Physics (UFS) and post graduate students.
  - I would like to thank my officemate Mr Wael Tabaza and my colleagues during the PhD studies, Mr Abd Ellateef Abbass, Mr Mubarak Yagoub, Mrs Rasha Mohammed, Dr Samy Shaat.
  - My appreciations go to Dr Liza Hugo-Coetzee, Mrs Mart-Mari Biggs, Mr Pieter Barnad, Mr Luyanda Lunga Noto for their assistance in getting some results of this project.
  - I also acknowledge the support of the administrative staff in the Physics Department, namely Ms Karen Cronje and Mrs Yolandie Fick.

I would like to thank my lovely family and friends for their invaluable help and endless encouragement.

**I am greatly indebted to the African Laser Center (ALC) for financial support.**

Dedicated to the memory of my lovely father; the late  
Yousif Mohammed Ahmmed (1945-1993)

To my mother, Nasra El-Mahi, Her support,  
encouragement, and constant love have sustained me  
throughout my life

To my wife, Rasha Mohammed Jafer and my kids,  
Yasser and Fatimah Al Zahra, for their endless love,  
support and encouragement

To my Brothers and Sisters, for their respect and  
appreciation

## Abstract

The main aim of this project was to use the technique of pulsed laser deposition (PLD) to fabricate thin films from Yttrium Aluminium Gallium Oxide ( $Y_3(Al, Ga)_5O_{12}$ ) doped with  $Tb^{3+}$  ions and then to investigate the structure, the morphology and the optical properties of the fabricated films.

Initially, the structure, morphology, luminescent properties and surface state before and after 27 h of prolonged electron beam exposure of  $Y_3(Al, Ga)_5O_{12}:Tb$  phosphor powder were determined, in order to understand the material and find the necessary background that could assist in future research on this material. The electron irradiation was carried out at a base pressure of  $2.3 \times 10^{-8}$  Torr and an oxygen pressure of  $1.0 \times 10^{-6}$  Torr. New surface layers were formed after the chemisorbed species were removed as a result of electron stimulated surface chemical reactions. The rate of the removal of the chemisorbed species from the phosphors surface during prolonged electron irradiation was affected by the background working atmosphere as measured with Auger electron spectroscopy combined with cathodoluminescence (CL) spectroscopy. The CL intensity of the  $Y_3(Al, Ga)_5O_{12}:Tb$  stabilized after removal of the chemisorbed species and stayed constant during further electron irradiation, indicating that this phosphor is appropriate for the field emission display technology. There was an increase in the Al, Y, O and Tb Auger peak intensities pointing to the formation of a complicated surface structure that was probably a combination of more than one chemical compound. X-ray photoelectron spectroscopy (XPS) results suggested electron-beam induced formation of new interleave oxide layers, such as  $AlO_x$ ,  $YO_x$  and  $Y(Al, Ga)_5O_3$  on the surface. These oxide layers acted as protective layers inhibiting further CL intensity degradation during the prolonged electron irradiation. Moreover, the photoluminescence (PL) excitation and emission spectra of  $Tb^{3+}$  in the  $Y_3(Al, Ga)_5O_{12}$  phosphor were measured and analysed. The excitation spectrum was measured at an emission wavelength of 544 nm and the emission spectrum was measured at an excitation wavelength of 267

---

nm. The emission showed the well-known  ${}^5D_4 \rightarrow {}^7F_J$  ( $J = 6, 5, 4, 3$ ) transitions of the  $Tb^{3+}$  ion. The main PL emission peak was due to the  ${}^5D_4 \rightarrow {}^7F_5$  transition of  $Tb^{3+}$  with minor peaks at 489 nm ( ${}^5D_4 \rightarrow {}^7F_6$ ), 590 nm ( ${}^5D_4 \rightarrow {}^7F_4$ ) and 625 nm  ${}^5D_4 \rightarrow {}^7F_3$ .

Thin films of the  $Y_3(Al, Ga)_5O_{12}:Tb$  powder were grown on Si(100) substrates by the PLD technique using a Nd:YAG pulsed laser with a wavelength of 266 nm. The influence of the working atmosphere (base pressure,  $O_2$ , Ar and  $N_2$ ) on the morphology, structure and luminescence properties were investigated. The brightest emission was observed from the film which was deposited in the  $O_2$  atmosphere, indicating that oxygen was the best working atmosphere for growing the  $Y_3(Al, Ga)_5O_{12}:Tb$  thin films.

The as deposited  $Y_3(Al, Ga)_5O_{12}:Tb$  films were amorphous in most cases and crystallized upon heat treatment. Heat treatments were applied to the films for different annealing times and temperatures. Interesting phenomena occurred during the heat treatment which are summarized below:

Firstly, the films were annealed at 800 °C, 1000 °C and 1200 °C for 3 hrs. The influence of the annealing on the optical properties (excitation and the emission bands) and the crystal structure of the thin film were monitored. X-ray diffraction (XRD) and the XPS depth profiles indicated that there were annealing-induced changes in the crystal structure and chemical composition and consequent changes in the excitation bands. These changes (structure and composition) were attributed to interdiffusion of atomic species between the substrate and the  $Y_3(Al, Ga)_5O_{12}:Tb$  thin film. The XRD and XPS data confirm that after annealing,  $Y_3(Al, Ga)_5O_{12}:Tb$  was converted to  $Y_2Si_2O_7:Tb$ . A change in the relative ratios of the excitation band intensities was measured. Atomic force microscopy (AFM) showed that topographical changes also occurred during the annealing process. Thermoluminescence (TL) glow curves of the  $Y_3(Al, Ga)_5O_{12}:Tb$  thin films before and after annealing, indicated the presence of different types of traps resulting from the change on the structure of the

---

thin films.

Secondly, to avoid the changes on film's structure and the optical properties, the films were deposited on SiO<sub>2</sub>/Si(100) substrates first and then annealed in air at 800 °C, 900 °C and 1000 °C. AFM, XRD, PL, X-ray photoelectron spectroscopy and Nano scanning Auger electron microprobe (NanoSAM) techniques have been applied to characterize these films. The results were compared to previously investigated Y<sub>3</sub>(Al, Ga)<sub>5</sub>O<sub>12</sub>:Tb thin films on Si(100) without an oxide (SiO<sub>2</sub>) layer. No change in the PL excitation bands as the result of post annealing was observed. Enhancement of the PL intensities was observed as a function of annealing temperatures, which was attributed to the improvement of the crystallization of the annealed films. Annealing, however, caused stress in the films and aggravated cracking occurred. Diffusion of atomic species from the substrate to the film's materials occurred, leading to phase changes and changes in stoichiometry. After annealing at higher temperatures, some regions on the film's surface were enriched with Si were observed.

Thirdly, to avoid severe chemical reactions between the Si substrate and the film at higher annealing temperatures, the annealing time was shortened from 3 hrs to 1 h. The effect of annealing the films in air at 400 °C and 800 °C for 1 h was investigated. The three dimensional AFM images of the as-deposited film shows well defined spherically grains that were uniformly distributed over the surface with a root mean square (RMS) roughness value of 9 nm. After annealing at 800 °C the surface became smooth and the RMS value was reduced to 6 nm. The smooth layer was confirmed to be a surface oxide layer enriched with Ga from the images captured using the NanoSAM. The PL intensities were observed to increase as a function of annealing temperature and this was attributed to the improvement of the crystallinity of the films and a possible variation of the Ga concentration in the thin films. In addition, CL properties of the films were recorded when the films were irradiated with a beam of electrons in the vacuum chamber of the Auger electron spectrometer. The CL intensity of the deposited

---

film was recorded as a function of electron dose as well as the accelerating voltage. The CL has decreased to about 50% after 450 C/cm<sup>2</sup> electron dose whilst increased with an increase in the accelerating voltage from 1 to 3 keV.

Fourthly, the annealing effect were studied further on the films annealed at 800 °C for 1 and 2 hrs in air. AFM showed an increase in grain size with an increase in annealing time. The PL emission spectrum presented similar characteristics for all different annealing times, and the emissions are explained by the well-known  $^5D_4 \rightarrow ^7F_J$  ( $J = 6, 5, 4, 3$ ) transitions of the Tb<sup>3+</sup> ion. A new excitation band located at around 200 nm was observed from all the annealed films which pointed to a change in the chemical environment, owing to the fact that, the 5d level depends strongly on the nature of the host due to a greater radial extension of the 5d orbital. Shift in the XRD peaks position to lower diffraction angles was also observed in the XRD results compared to the pattern of the Y<sub>3</sub>(Al, Ga)<sub>5</sub>O<sub>12</sub>:Tb powder and other thin films. The new excitation band and the shift in the peak position of the XRD pattern were attributed to the enrichment of the annealed films with Ga due to spreading phenomena of the agglomerated Ga particulates during the annealing process.

## ABBREVIATIONS

- **YAG** Yttrium aluminium garnet ( $\text{Y}_3\text{Al}_5\text{O}_{12}$ ).
- **YGG** Yttrium gallium garnet ( $\text{Y}_3\text{Ga}_5\text{O}_{12}$ ).
- **PLD** Pulsed laser deposition.
- **XRD** X-ray diffraction.
- **PL** Photoluminescence.
- **CL** Cathodoluminescence.
- **AES** Auger electron spectroscopy.
- **APPH** Auger peak-to-peak heights.
- **XPS** X-ray photoelectron spectroscopy.
- **ESSCR** Electron stimulated surface chemical reaction.
- **SEM** Scanning electron microscopy.
- **AFM** Atomic force microscopy.

# Contents

<b>ABBREVIATIONS</b>	<b>viii</b>
<b>List Of Figures</b>	<b>xii</b>
<b>List Of Tables</b>	<b>xix</b>
<b>1 Introduction</b>	<b>1</b>
1.1 Overview . . . . .	1
1.2 Motivation . . . . .	2
1.3 Research aims . . . . .	3
1.4 Organisation of the thesis . . . . .	4
<b>2 Background on pulsed laser deposition and luminescent materials</b>	<b>7</b>
2.1 PLD Technique . . . . .	7
2.1.1 Ablation . . . . .	8
2.1.2 Expanding of ablation materials . . . . .	9
2.1.3 Deposition of the ablation material on a substrate . . . . .	9
2.2 Typical experimental set-up . . . . .	13
2.3 Versatility of the PLD technique . . . . .	13
2.3.1 Laser wavelength . . . . .	13
2.3.2 High vacuum (HV) and different gas atmospheres . . . . .	14
2.3.3 Stoichiometry transfer . . . . .	15
2.4 Limitations and advantages of PLD . . . . .	15
2.5 Luminescent materials . . . . .	18
<b>3 Film and powder characterization techniques</b>	<b>25</b>
3.1 The XRD technique . . . . .	25
3.2 Photoluminescence (PL) . . . . .	27
3.3 The XPS technique . . . . .	28

3.4	The AES technique . . . . .	31
3.5	The AFM technique . . . . .	36
3.6	Scanning Electron Microscopy (SEM) . . . . .	40
3.7	Cathodoluminescence (CL) . . . . .	42
<b>4</b>	<b>Surface state of <math>Y_3(Al, Ga)_5O_{12}:Tb</math> phosphor powder under electron beam bombardment</b>	<b>45</b>
4.1	Introduction . . . . .	45
4.2	Experimental . . . . .	46
4.3	Result and discussion . . . . .	47
4.3.1	Structural and morphology analysis . . . . .	47
4.3.2	PL and CL results . . . . .	49
4.3.3	AES and APPHs analysis . . . . .	56
4.3.4	XPS results . . . . .	60
4.4	Conclusion . . . . .	67
<b>5</b>	<b>The influence of working atmosphere on <math>Y_3(Al, Ga)_5O_{12}:Tb</math> thin films grown with the PLD technique</b>	<b>71</b>
5.1	Introduction . . . . .	71
5.2	Experimental . . . . .	72
5.3	Results and discussion . . . . .	73
5.4	Conclusion . . . . .	81
<b>6</b>	<b>Improved luminescence properties of pulsed laser deposited <math>Y_3(Al, Ga)_5O_{12}:Tb</math> thin films by post deposition annealing</b>	<b>83</b>
6.1	Introduction . . . . .	83
6.2	Experimental . . . . .	84
6.3	Result and discussion . . . . .	85
6.3.1	Structural and surface topography analysis . . . . .	85
6.3.2	Auger peak to peak heights (APPH) analysis . . . . .	89

6.3.3	2D NanoSAM Cross Section of annealed film . . . . .	90
6.3.4	PL result . . . . .	90
6.3.5	Cathodoluminescence (CL) . . . . .	92
6.4	Conclusion . . . . .	95
<b>7</b>	<b>Conversion of <math>Y_3(Al, Ga)_5O_{12}:Tb</math> to <math>Y_2Si_2O_7:Tb</math> thin film by annealing at higher temperatures</b>	<b>98</b>
7.1	Introduction . . . . .	98
7.2	Experimental . . . . .	100
7.3	Result and discussion . . . . .	101
7.3.1	Structural and morphology analysis . . . . .	101
7.3.2	PL and CL results . . . . .	103
7.3.3	Thermoluminescence (TL) . . . . .	109
7.3.4	XPS analysis . . . . .	113
7.4	Conclusion . . . . .	119
<b>8</b>	<b>Effect of different annealing temperatures on the optical properties of <math>Y_3(Al, Ga)_5O_{12}:Tb</math></b>	<b>122</b>
8.1	Introduction . . . . .	122
8.2	Experimental . . . . .	123
8.3	Result and discussion . . . . .	123
8.4	Conclusion . . . . .	133
<b>9</b>	<b>Effect of annealing on the structure of <math>Y_3(Al, Ga)_5O_{12}:Tb</math> thin film grown by PLD</b>	<b>135</b>
9.1	Introduction . . . . .	135
9.2	Experimental . . . . .	136
9.3	Results and discussion . . . . .	137
9.4	Conclusion . . . . .	144
<b>10</b>	<b>Summary and suggestions for future work</b>	<b>146</b>

10.1 Summary of results and significant achievements . . . . .	146
10.2 Suggestions for future work . . . . .	147

## List of Figures

1.1	Schematic sketch on PLD symbols of $Y_3(\text{Al}, \text{Ga})_5\text{O}_{12}:\text{Tb}$ phosphor in thin film form . . . . .	3
2.1	A schematic of the laser ablation process and its stages up to thin film formation [2] . . . . .	8
2.2	Photographic images of $\text{YBa}_2\text{Cu}_3\text{O}_{7-\delta}$ plume formation as a function of $\text{O}_2$ deposition pressure [8] . . . . .	10
2.3	Examples of plasma plumes produced during PLD from different targets [10] . . . . .	11
2.4	Three modes of the thin film growth processes [11]. . . . .	12
2.5	Schematic diagram of a PLD system . . . . .	14
2.6	The PLD system at the National Laser Centre (NLC, CSIR), Pretoria. . . . .	15
2.7	In-house build sample holder that was used for PLD. . . . .	16
2.8	Schematic of a large-area PLD system utilizing laser rastering over large-diameter targets [17]. . . . .	18
2.9	Different kind of phosphor materials in the day light and when excited it by ultraviolet or electron sources. . . . .	19
2.10	The arrangement of Y, O, Al and Ga described with polyhedral in $Y_3(\text{Al}, \text{Ga})_5\text{O}_{12}:\text{Tb}$ (ICSD-29248) . . . . .	20
2.11	Emission of $Y_3(\text{Al}, \text{Ga})_5\text{O}_{12}:\text{Tb}$ powder under 267 nm excitation. . . . .	22
3.1	The schematic diagram of Braggs law. . . . .	26
3.2	A photo of the Bruker AXS D8 ADVANCE X-ray diffractometer at the Department of Physics of the University of the Free State. . . . .	26
3.3	Diagram illustrates the characteristic X-ray emission obtained from a copper (Cu) target with nickel (Ni) filter [18]. . . . .	27

3.4	Cary Eclipse fluorescence spectrophotometer at the Department of Physics of the University of the Free State. . . . .	28
3.5	The schematic diagram of XPS with a survey of the $Y_3(Al, Ga)_5O_{12}:Tb$ film. . . . .	30
3.6	PHI 5400 Versaprobe scanning XPS unit at the Department of Physics of the University of the Free State. . . . .	30
3.7	Relaxation of the ionized atom by the emission of a $KL_{2,3} L_{2,3}$ Auger electron. . . . .	32
3.8	Comparison of (a) direct, and (b) differential Auger spectra for $Y_3(Al, Ga)_5O_{12}:Tb$ thin film. . . . .	33
3.9	Typical AES mapping of $Y_3(Al, Ga)_5O_{12}:Tb$ thin films with combination of O (red), Y (blue) and Ga (green). . . . .	34
3.10	PHI, model 549, AES unit at the Department of Physics of the University of the Free State. . . . .	35
3.11	The PHI 700 Auger Nanoprobe SEM unit at the Department of Physics of the University of the Free State. . . . .	35
3.12	Scheme of an atomic force microscope. . . . .	37
3.13	The force-distance curve characteristic of the interaction between the tip and sample. . . . .	38
3.14	A piezoelectric crystal create a pressure by expanding or contracting if a voltage is applied . . . . .	38
3.15	Shimadzu SPM-9600 AFM at the Department of Physics of the University of the Free State. . . . .	39
3.16	Schematic diagram of SEM and some type of signals available due to electron interaction . . . . .	41
4.1	XRD spectra of $Y_3(Al, Ga)_5O_{12}:Tb$ phosphor and standard data. . . . .	48

4.2	SEM photograph of $Y_3(Al, Ga)_5O_{12}:Tb$ phosphor with 25 kV beam energy, different field of view of (a) $10\mu m$ , (b) $5\mu m$ (c) $2\mu m$ and (d) $2\mu m$ with color. . . . .	49
4.3	$Y_3(Al, Ga)_5O_{12}:Tb$ unit cell (ICSD-29248). . . . .	50
4.4	The arrangement of Y, O, Al and Ga described with polyhedral in $Y_3(Al, Ga)_5O_{12}:Tb$ (ICSD-29248). . . . .	52
4.5	Excitation bands energies versus the gallium ion concentration in the garnet host. . . . .	53
4.6	PL emission and excitation of $Y_3(Al, Ga)_5O_{12}:Tb$ (Excitation measured at an emission wavelength of 544 nm; emission measured at an excitation wavelength of 267 nm). . . . .	54
4.7	The CL spectra of $Y_3(Al, Ga)_5O_{12}:Tb$ phosphor, before and after electron beam bombarded in an oxygen ambient pressure of $1.0 \times 10^{-6}$ Torr. (Excitation measured at an emission wavelength of 544 nm; emission measured at an excitation wavelength of 267 nm). . . . .	55
4.8	Auger spectra before and after electron beam bombardment at a base pressure of $2.3 \times 10^{-8}$ Torr. . . . .	57
4.9	CL intensity and APPH (right scale) as a function of electron beam exposure for the $Y_3(Al, Ga)_5O_{12}:Tb$ phosphor at the base pressure of $2.3 \times 10^{-8}$ Torr. . . . .	58
4.10	CL intensity and APPH (right scale) as a function of electron beam exposure for the $Y_3(Al, Ga)_5O_{12}:Tb$ phosphor at an oxygen pressure of $1.0 \times 10^{-6}$ Torr. . . . .	59
4.11	Deconvoluted O (1s), Y (3d), Al (2p) and Ga (2p) XPS peaks of $Y_3(Al, Ga)_5O_{12}:Tb$ phosphor at the base pressure of $2.3 \times 10^{-8}$ priors to [(a)(d) and (e)-(h)] and after electron beam exposure respectively . . . . .	66

5.1	XRD spectra of $Y_3(Al, Ga)_5O_{12}:Tb$ phosphor powder and thin films grown in different working atmosphere. . . . .	74
5.2	Three dimensional AFM images, for the thin film surfaces, grown in (a) base, (b) $O_2$ , (c) Ar and (d) $N_2$ atmosphere. . . . .	75
5.3	SEM images, for the thin film surfaces, grown in (a) base, (b) $O_2$ , (c) Ar and (d) $N_2$ atmosphere. . . . .	76
5.4	Different AES spectra of $Y_3(Al, Ga)_5O_{12}:Tb$ powder (1) and thin films grown in base pressure (2-4), (5) $O_2$ , (6)Ar and (7) $N_2$ atmospheres. . . . .	77
5.5	Depth profiles of the thin films structures, that were grown in (a) base, (b) $O_2$ , (c) Ar and (d) $N_2$ atmosphere. . . . .	78
5.6	Depth profile of the phosphor powder. . . . .	79
5.7	PL emission and excitation of $Y_3(Al, Ga)_5O_{12}:Tb$ thin films grown in different working atmosphere (Excitation measured at an emission wavelength of 544 nm; emission measured at an excitation wavelength of 267 nm). . . . .	80
6.1	XRD spectra of $Y_3(Al, Ga)_5O_{12}:Tb$ phosphor powder, deposited and annealed thin films. . . . .	86
6.2	AFM images of the surface of (a) $Y_3(Al, Ga)_5O_{12}:Tb$ thin films as deposited and (b) after annealed at 800° C. . . . .	87
6.3	(a and b) NanoSEM and SAM images for deposited and annealed films at 800 °C, of the combination of Al (red), Ga (green) and Y (blue) with 5 $\mu$ m field of view. . . . .	88
6.4	The AES depth profiles for the as deposited and 800° C annealed $Y_3(Al, Ga)_5O_{12}:Tb$ film. . . . .	89
6.5	(a and b) Elemental mapping of the cross sections of the annealed film at 800 °C, with the three colors: red, green and blue, representing O, Ga and Si, in 2 and 1 $\mu$ m field of view, respectively. .	91

6.6	PL emissions and PL intensity (inset) as function of annealing temperature. . . . .	92
6.7	The CIE chromaticity diagram for deposited $Y_3(Al, Ga)_5O_{12}:Tb$ film. . . . .	93
6.8	CL emission and intensity (inset) of the deposited films as a function of prolonged electron irradiation. . . . .	94
6.9	The CL emission and intensity (inset) for the deposited $Y_3(Al, Ga)_5O_{12}:Tb$ film as a function of the accelerating voltage. . . . .	95
7.1	XRD spectra of $Y_3(Al, Ga)_5O_{12}:Tb$ phosphor powder, unannealed and annealed thin films with the standard ICSD data of $\alpha$ - $Y_2SiO_7$ . . . . .	103
7.2	AFM images of the surface of (a) $Y_3(Al, Ga)_5O_{12}:Tb$ thin films as prepared and (b) after annealed at 1200 °C. . . . .	104
7.3	(a) PL emission and excitation spectra of as prepared and annealed thin films. (b) The relative ratio of the intensities of the 267:227 nm excitation bands, showing the relative change of the excitations bands from 267 nm to 227 nm.(c) Relative emission ratio intensities as a function of the different annealing temperatures of the films. . . . .	106
7.4	(a) and (b) CL intensities before and after electron beam exposure of the $Y_3(Al, Ga)_5O_{12}:Tb$ unannealed and annealed films (1200 °C), respectively. . . . .	107
7.5	CL intensities as a function of electron beam exposure for the $Y_3(Al, Ga)_5O_{12}:Tb$ unannealed and annealed films (1200 °C). . . . .	108
7.6	Change in thermally stimulated luminescence glow curves for unannealed and annealed thin films after different annealing temperatures, 800 °C, 1000 °C and 1200 °C, respectively. . . . .	111

7.7	Deconvolution of the films glow curves with a set of kinetics models for unannealed and annealed thin films after different annealing temperatures, 800 °C, 1000 °C and 1200 °C, respectively. . .	112
7.8	The XPS depth profiles for $Y_3(Al, Ga)_5O_{12}:Tb$ thin film phosphors (a) as prepared, (b-d) annealed in air at 800 °C, 1000 °C and 1200 °C. respectively. A, B and C show the beginning and end positions of the 3D XPS profiles. . . . .	116
7.9	XPS depth profiles of selected Si (2p) signals of the films (a and b) annealed at 800 °C (c and d) annealed at 1200 °C. 1st Part from A to B and 2nd Part from B to C as indicated in Figure 7.8	117
7.10	Deconvolution of selected Si (2p) signals of the film (a) annealed at 800 °C and (b) annealed at 1200 °C. . . . .	118
8.1	NanoSEM and SAM images for deposited and annealed films at 800 °C, 900 °C and 1000 °C of the combination of Si (red), Ga (green) and Al (blue) with 10 $\mu$ m field of view. . . . .	125
8.2	The depth profiles for the as deposited 800, 900 and 1000 °C annealed $Y_3(Al, Ga)_5O_{12}:Tb$ films respectively. . . . .	126
8.3	XPS depth profiles of selected O (1s) and Y(3d) signals of the films annealed at 900 °C. . . . .	127
8.4	XRD spectra of $Y_3(Al, Ga)_5O_{12}:Tb$ phosphor powder, as prepared and annealed thin films. . . . .	128
8.5	AFM images of the surface of (a) $Y_3(Al, Ga)_5O_{12}:Tb$ thin films on $SiO_2/Si$ substrate, annealed for 3 hours, (a) as deposited and (b), (c) and (d) after annealed at 800 °C, 900 °C and 1000 °C respectively. (e) and (f) images for the same materials on Si substrate annealed for 1 at 800 °C and the others at 1200 °C for 3 hrs respectively. . . . .	129

8.6	PL excitation and emission spectra of as prepared and annealed thin films for the films prepared on (a) SiO <sub>2</sub> /Si, (b) and (c) on Si substrates. The films in (a) and (b) annealed for three hours while the film in (c) annealed for 1 hour. (d) and (e) show the relative ratio of the intensities of the 267:227 nm excitation bands and the relative emission ratio intensities as a function of the different annealing temperatures, respectively. . . . .	132
9.1	(a) XRD patterns of the Y <sub>3</sub> (Al, Ga) <sub>5</sub> O <sub>12</sub> :Tb phosphor powder, and Y <sub>3</sub> (Al, Ga) <sub>5</sub> O <sub>12</sub> :Tb films as prepared and annealed at 800 °C. (b) XRD patterns of the commercial and prepared Y <sub>3</sub> (Al, Ga) <sub>5</sub> O <sub>12</sub> :Tb powder, showing the change in the peak position with different Ga concentrations. . . . .	139
9.2	Change in lattice parameter of the garnet crystal structure with different Ga concentrations. . . . .	140
9.3	AFM images of the surface of the Y <sub>3</sub> (Al, Ga) <sub>5</sub> O <sub>12</sub> :Tb films (a) as prepared and annealed at 800 °C for (b) 2 hrs and (c) 3 hrs. . .	141
9.4	PL excitation and emission of the prepared Y <sub>3-x</sub> Al <sub>y</sub> Ga <sub>z</sub> O <sub>12</sub> :Tb <sub>x=0.05</sub> powder with different Ga concentration. . . . .	142
9.5	(a) PL excitation of the Y <sub>3</sub> (Al, Ga) <sub>5</sub> O <sub>12</sub> :Tb films as prepared and annealed at 800 °C for 1 h and 2 h. (b)- (d) PL excitation of the Y <sub>3</sub> (Al, Ga) <sub>5</sub> O <sub>12</sub> :Tb powder with different Ga concentration. . . .	143

## List of Tables

4.1	Binding energies for Al (2p) XPS peaks in $Y_3(Al, Ga)_5O_{12}:Tb$ before and after electron degradation. . . . .	61
4.2	Binding energies for Y (3d) XPS peaks in $Y_3(Al, Ga)_5O_{12}:Tb$ before and after electron degradation. . . . .	61
4.3	Binding energies for O (1s) XPS peaks in $Y_3(Al, Ga)_5O_{12}:Tb$ before and after electron degradation. . . . .	62
4.4	Binding energies for Ga (2p) XPS peaks in $Y_3(Al, Ga)_5O_{12}:Tb$ before and after electron degradation. . . . .	62
4.5	Binding energies for Tb (3d) XPS peaks in $Y_3(Al, Ga)_5O_{12}:Tb$ before and after electron degradation. . . . .	62
5.1	Atomic concentrations determined from the middle of the thin film layers deposited in the different working atmosphere . . . . .	79
7.1	The kinetic parameters for the unannealed fitted peak. . . . .	113
7.2	The kinetic parameters for the annealed fitted peak (800 °C). . . . .	113
7.3	The kinetic parameters for annealed fitted peak (1000 °C). . . . .	114
7.4	The kinetic parameters for annealed fitted peak (1200 °C). . . . .	114
7.5	Binding energies for Si 2p XPS peaks in $Y_3(Al, Ga)_5O_{12}:Tb$ after heat treatment at 800 °C and 1200 °C. . . . .	119

# Chapter 1

## Introduction

### 1.1 Overview

A thin film is regarded as a layer of material ranging from a fractions of a nanometer to several micrometers in thickness. This layer is created by condensing, one-by-one, atomic, molecular, and/or ionic species of matter [1, 2]. Luminescent thin films are of great interest from both scientific and technological point of view. The research interest in luminescent thin films has been reflected by the rapid developments in a variety of thin-film luminescent devices, including flat-panel displays, light sources, solar cells and integrated optics systems [1]. Luminescent materials deposited in the form of thin films have a number of important advantages over powder phosphors of the same composition due to their good luminescence characteristics, higher image resolution from small grains, better thermal stability and good adhesion to the substrate [3]. Luminescent thin films can be prepared by a variety of deposition techniques, such as pulsed laser deposition (PLD), sputtering, spray pyrolysis, sol-gel method, etc. Of all the thin films preparation methods, the PLD technique is considered as a very effective method to grow high quality films with a complex composition. Additionally, thin films deposited by PLD can result in better crystal structure at lower temperatures than by other techniques, which is caused by the higher energy of the ablated particles in the laser-produced plasma plume [4]. Moreover, there are still other advantages of using the PLD technique making it so effective. For example, deposition processes in a controllable oxygen ambient pressure result in high controllability of the thin film chemical elemental composition and grain growth processes. Thus, in this project,  $Y_3(Al, Ga)_5O_{12}:Tb$  thin films were deposited on Si(100) substrates by PLD, and the influence of

the different working atmosphere was studied. The effect of annealing on the luminescent properties as well as crystal structure was also studied in order to improve the optical properties of the films.

## 1.2 Motivation

Over the past few years, phosphor films have attracted much attention because of their potential applications to a large variety of display devices [5]. The technology of thin film deposition has advanced dramatically during the past 30 years [6]. This advancement was driven primarily by the need for new products and devices in the electronics and optical industries. The rapid progress in solid-state electronic devices would not have been possible without the development of new thin film deposition processes, improved film characteristics and superior film qualities. Thin film deposition technology is still undergoing rapid changes which will lead to even more complex and advanced electronic devices in the future [6].

Among the deposition techniques, the PLD is one of the widely used technique in oxides thin film deposition. It offers relative simplicity in controlling the deposition rate and in obtaining the correct stoichiometric transfer of the material from the bulk to the deposited film. The properties of thin films deposited by PLD depend on a number of deposition parameters such as ambient pressure, target substrate distance, substrate temperature and each must be considered when developing a reproducible process and obtaining a high product throughput and yield from the production line.

It is well known that, among green phosphors,  $Y_3Al_5O_{12}:Tb$  has high resistivity against high-density electron bombardment. The phosphor  $Y_3(Al, Ga)_5O_{12}:Tb$  formed by partial substitution of aluminum in  $Y_3Al_5O_{12}:Tb$  with Ga, has higher efficiency and better current dependence of efficiency than  $Y_3Al_5O_{12}:Tb$  [7]. However, there are no reports on the luminescent properties of  $Y_3(Al, Ga)_5O_{12}:Tb$

phosphor in the thin film form deposited by the PLD technique. Therefore, in view of the practical application point, it is necessary to fabricate this kind of phosphor in the thin film form and to investigate its luminescent properties. Our motivation was:

- To learn how to deposit a more efficient and stable  $Y_3(Al, Ga)_5O_{12}:Tb$  thin film by the PLD technique, (Figure 1.1).

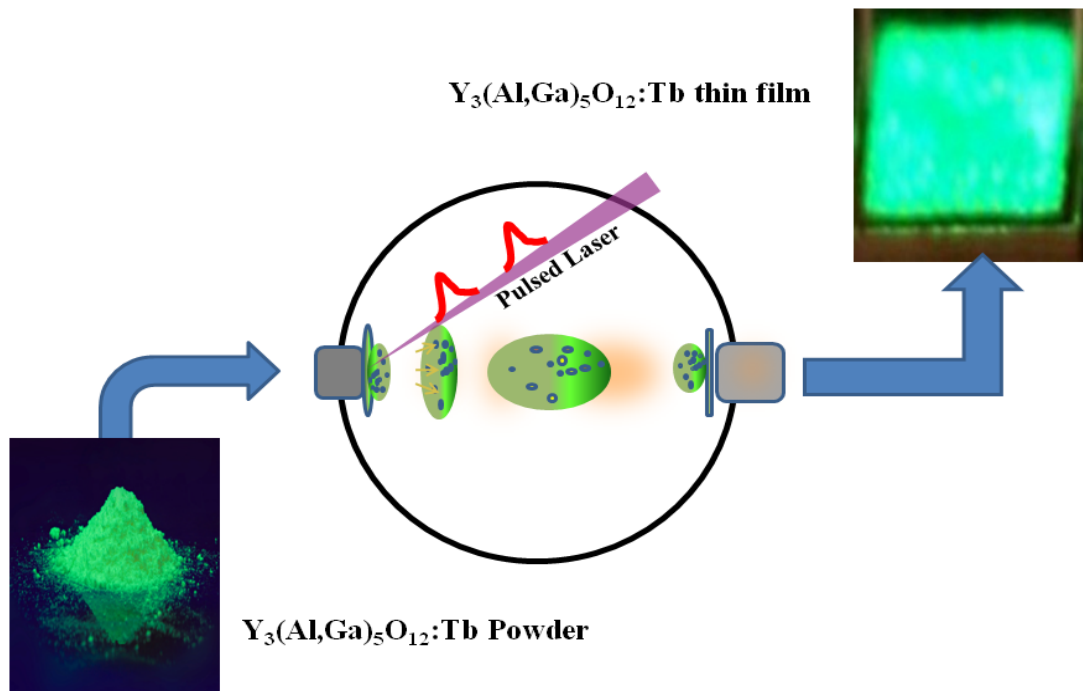


**Figure 1.1:** Schematic sketch on PLD symbols of  $Y_3(Al, Ga)_5O_{12}:Tb$  phosphor in thin film form

### 1.3 Research aims

- To characterize commercial  $Y_3(Al, Ga)_5O_{12}:Tb$  phosphor powder by using different techniques.
- To prepare  $Y_3(Al, Ga)_5O_{12}:Tb$  thin films by the PLD.

- To study the changes in morphology and luminescence properties of the thin films when changing the deposition background gas and pressure.
- To study the effect of heat treatment on the optical properties after different annealing temperatures.

### 1.4 Organisation of the thesis

The thesis is divided into ten chapters, each covering a specific subject as follows:

**Chapter (1)** gives an overview, motivation, research aims and the general structure of the thesis. **Chapter (2)** is an introduction to the PLD as well as luminescent materials. **Chapter (3)** describes the research techniques involved in this work for the phosphor powder and the thin film characterisation. **Chapter (4)** discusses mainly the surface state of  $\text{Y}_3(\text{Al}, \text{Ga})_5\text{O}_{12}:\text{Tb}$  phosphor under electron beam bombardment. **Chapter (5)** is devoted to the influence of different working atmosphere on the  $\text{Y}_3(\text{Al}, \text{Ga})_5\text{O}_{12}:\text{Tb}$  thin films. **Chapter (6)** discusses mainly the improvement of the luminescence properties of the  $\text{Y}_3(\text{Al}, \text{Ga})_5\text{O}_{12}:\text{Tb}$  thin films by post deposition annealing. **Chapter (7)** demonstrates how the thin film of  $\text{Y}_3(\text{Al}, \text{Ga})_5\text{O}_{12}:\text{Tb}$  is converted to  $\text{Y}_2\text{Si}_2\text{O}_7:\text{Tb}$  thin film by annealing at higher temperatures. **Chapter (8)** presents the results on the effect of the different annealing temperatures on the optical properties of  $\text{Y}_3(\text{Al}, \text{Ga})_5\text{O}_{12}:\text{Tb}$  thin films. **Chapter (9)** discusses the effect of the heat treatment on the structure of  $\text{Y}_3(\text{Al}, \text{Ga})_5\text{O}_{12}:\text{Tb}$  thin films. **Chapter (10)** gives the summary of the thesis results and suggestions for future work. The last part of the thesis gives a list of publications resulting from this work and the conferences/workshops presentations.

## References

- [1] Y. Zhang, J. Hao, *Journal of Materials Chemistry C* **1** (2013) 5607.
- [2] K. Wasa, M. Kitabatake, H. Adachi, *Thin film Materials Technology: Sputtering of Compound Materials*, William Andrew, Inc. 2004.
- [3] J. S. Bae, K. S. Shim, S. B. Kim, J. H. Jeong, S. S. Yi, J. C. Park, *Journal of Crystal Growth* **264** (2004) 290.
- [4] W. S. Hu, Z. G. Liu, J. Sun, S. N. Zhu, Q. Q. Xu, D. Feng, Z. M. Ji, *Journal of Physics and Chemistry of Solids* **58(6)** (1997) 853.
- [5] A. Potdevin, G. Chadeyron, S Therias, R. Mahiou, *Langmuir* **28** (2012) 13526.
- [6] K. Seshan, *Handbook of Thin-Film Deposition Processes and Techniques*, 2nd edition, Willim Andrew Publishing, 2001, Norwich, New York, U.S.A.
- [7] H. Matsukiyo, T. Suzuki, H. Yamada, H. Yamamoto, *J. of Electrochemical Society* **145** (1998) 270.
- [8] G. Li, Q. Cao, Z. Li, Y. Huang, Y. Wei, J. Shi, *Journal of Alloys and Compounds* **485** (2009) 561.
- [9] J. Y. Choe, D. Ravichandran, S. M. Blomquist, K. W. Kirchner, E. W. Forsythe, D. C. Morton, *Journal of Luminescence* **93** (2001) 119.
- [10] H. Matsukiyo, O. T. Suzuki, H. Yamada, H. Yamamoto, *Journal of The Electrochemical Society* **145** (1998) 270.
- [11] O. Katsutoshi, A. Tomohiko, K. Tsuneo, *Japanese Journal of Applied Physics* **29** (1990) 103.

## Chapter 1

---

- [12] H. Matsukiyo, T. Suzuki, H. Yamada, H. Yamamoto, Journal of Electrochemical Society **145** (1998)1.

# Chapter 2

## Background on pulsed laser deposition and luminescent materials

This chapter gives a brief description of the PLD technique which was used to grow the thin films as well as an introduction to luminescent materials.

### 2.1 PLD Technique

The development of powerful, high photon flux, Q-switched lasers has drastically changed our perception of light-matter interactions and opened new ways of implementing laser sources for the growth and processing of nanostructured materials. Therefore, the PLD has emerged as a very important growth technique in the nanotechnology era [2]. The principle of PLD is quite simple as the technique is based on physical processes that arise from the impact of high-power pulsed laser radiation on solid targets [4 - 6]. The laser irradiation induces vaporization, via heating of a target, and formation of plasma via ionization of target atoms. The mixed vapors and ions of the target material are called the plume. After the creation of the plume the material expands within a cone, whose axis is parallel to the normal vector of the target surface toward the substrate due to coulomb repulsion (for ions) and adiabatic expansion of the pressurized vapors [2]. These processes are displayed schematically in Figure 2.1. As is presented in Figure 2.1, there are many steps which can be quite complicated till the formation of the film. These steps basically are:

1. Ablation,
2. Expanding of ablation materials,
3. Deposition and movement of the ablation material on a substrate.

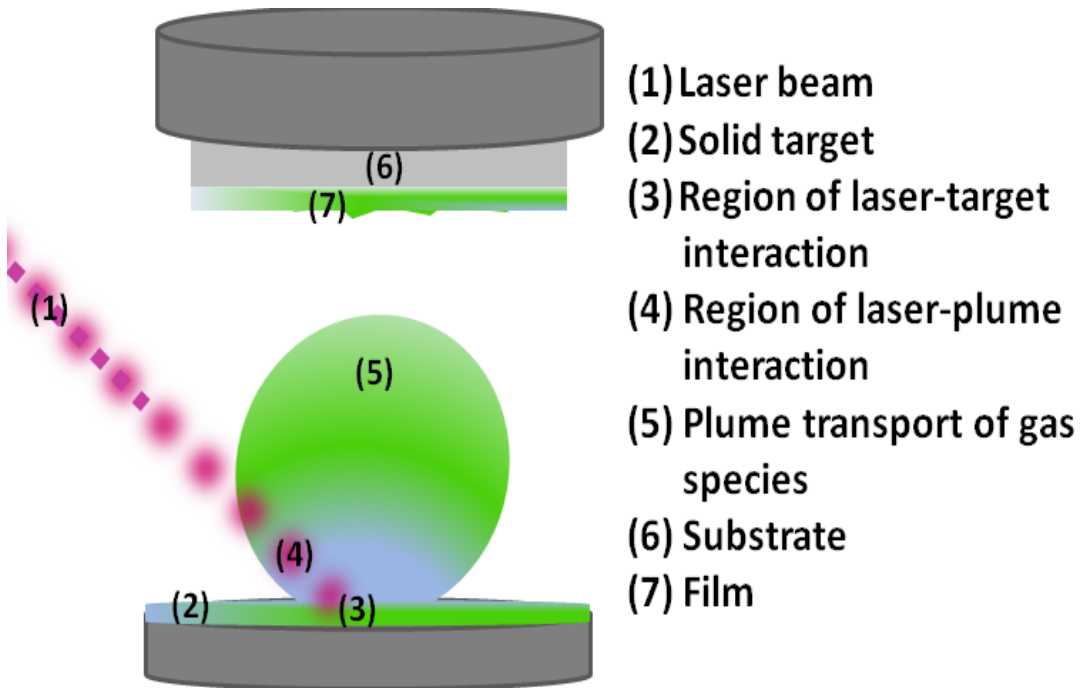


**Figure 2.1:** A schematic of the laser ablation process and its stages up to thin film formation [2]

### 2.1.1 Ablation

Generally ablation is removal of material from the surface of an object by vaporization, chipping, or other erosive processes [1]. The ablation in laser deposition is the laser energy gets coupled into the target material, subsequent material removal. There are many models for ablation [2]

**Photo-thermal ablation:**

Occurs when the laser is absorbed by the lattice of the material as heat before the materials bonds are broken. The absorbed energy serves to heat the target, resulting in the melting of the target and subsequent material vaporization.

**Photo-chemical ablation:**

Occurs when the laser is absorbed directly by the electronic bands, resulting in the immediate breaking of these bonds.

### Hydro-dynamical ablation:

Hydro-dynamical ablation refers to the processes in which the target surface melts forming small droplets of material. This process causes a bulk material, particulates, or droplets to be ejected from the target. The particles are ejected in a liquid state and can be identified by their spherical shape [2, 3].

### 2.1.2 Expanding of ablation materials

Expanding of the ejected particles and vapor travel toward the substrate. The expansion and shape of the plume depends on the surrounding gas pressure. Ambient gas molecules will retard the plume, resulting in greater particle interaction within the plume before interaction with the substrate. Lower kinetic energies of the incident particles are expected for higher gas pressures [7]. Figure 2.2 represent the effect of different O<sub>2</sub> deposition pressures ranging from 120 to 1200 mTorr on the plume shape as studied by T.Haugan et al [8]. Generally, the ablation plume takes a  $\cos^n(\theta)$  shape. Higher n, modeling a more directional plume, resulting from higher laser energy and a lower surrounding gas pressure [9]. The visible light of the plume is due to fluorescence and recombination processes in the plasma. Photographs of different plume's light from different materials are presented in Figure 2.3 [10].

### 2.1.3 Deposition of the ablation material on a substrate

Deposition of a film takes place via nucleation and growth processes. The general picture of step-by-step growth process emerging from the various experimental and theoretical studies can be presented as follows [11]:

1. The unit species, on impacting the substrate, lose their velocity component normal to the substrate (provided the incident energy is not too high) and are physically adsorbed on the substrate surface.

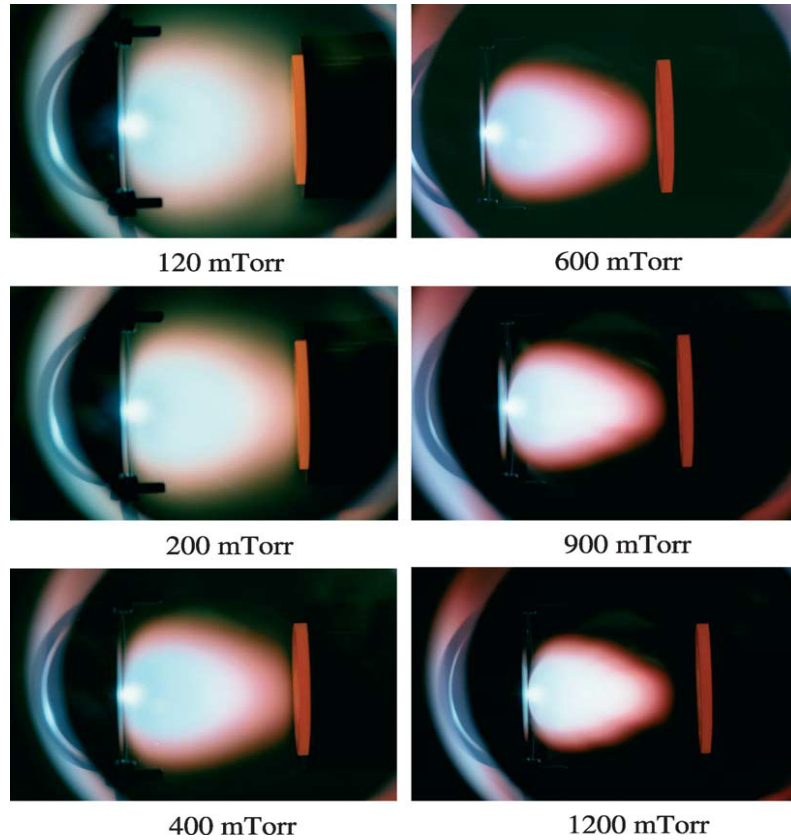


**Figure 2.2:** Photographic images of YBa<sub>2</sub>Cu<sub>3</sub>O<sub>7-δ</sub> plume formation as a function of O<sub>2</sub> deposition pressure [8]

2. The adsorbed species are not in thermal equilibrium with the substrate surface. In this process they interact among themselves, forming bigger clusters.
3. The clusters or the nuclei are thermodynamically unstable and may tend to desorb in time depending on the deposition parameters. If the deposition parameters are such that a cluster collides with other adsorbed species before getting desorbed, it starts growing in size. After reaching a certain critical size, the cluster becomes thermodynamically stable. This step involving the formation of stable, chemisorbed, critical-sized nuclei is called the **nucleation stage**.

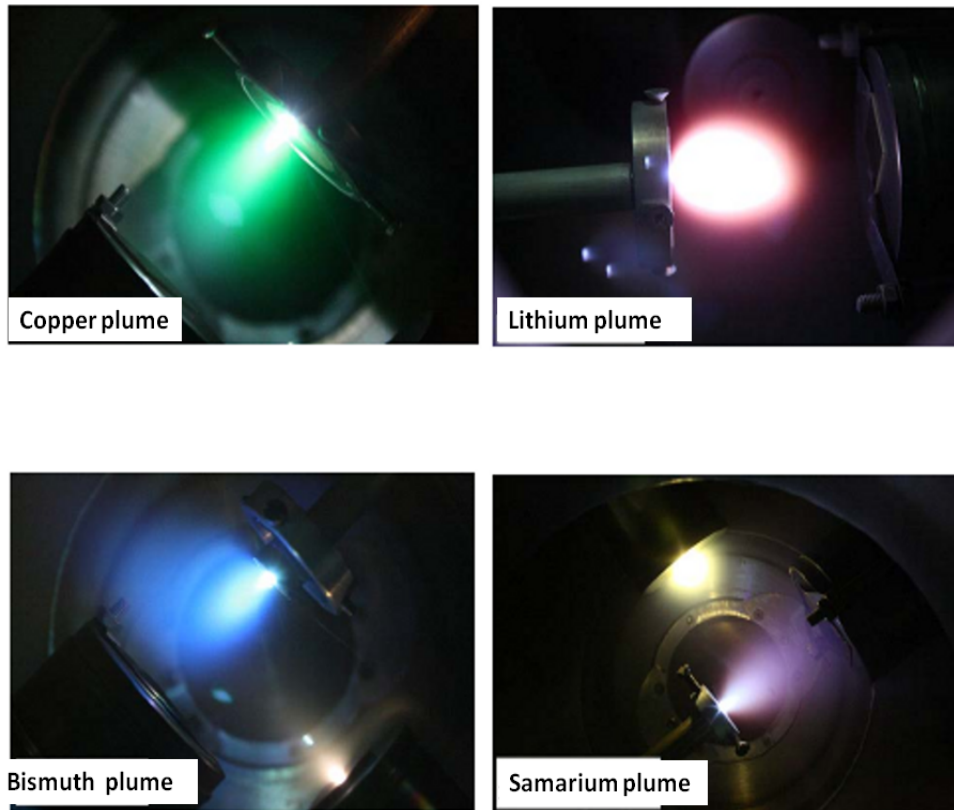


**Figure 2.3:** Examples of plasma plumes produced during PLD from different targets [10]

4. The critical nuclei grow in number as well as in size until a saturation nucleation density is reached. The rate of later growth at this stage is much higher than the perpendicular growth. The grown nuclei are called **islands**.
5. The next stage in the process of film formation is **coalescence stage**, in which the small islands start coalescing with each other in an attempt to reduce the substrate surface area. This tendency to form bigger islands is termed **agglomeration**.
6. Larger islands grow together, leaving channel and holes of uncovered substrate. The structure of the films at this stage changes from a discontinuous

island type to a porous network type. Filling of the channels and holes forms a completely continuous film.

The growth process may thus be summarized as:

1. Island type (called Volmer-Weber type),
2. Layer type (called Frank-van der Merwe type),
3. Mixed type (called Stranski-Krastanov type).

All this growth depends on the thermodynamic parameters of the deposit and the substrate surface. These growth types/models are illustrated in Figure 2.4

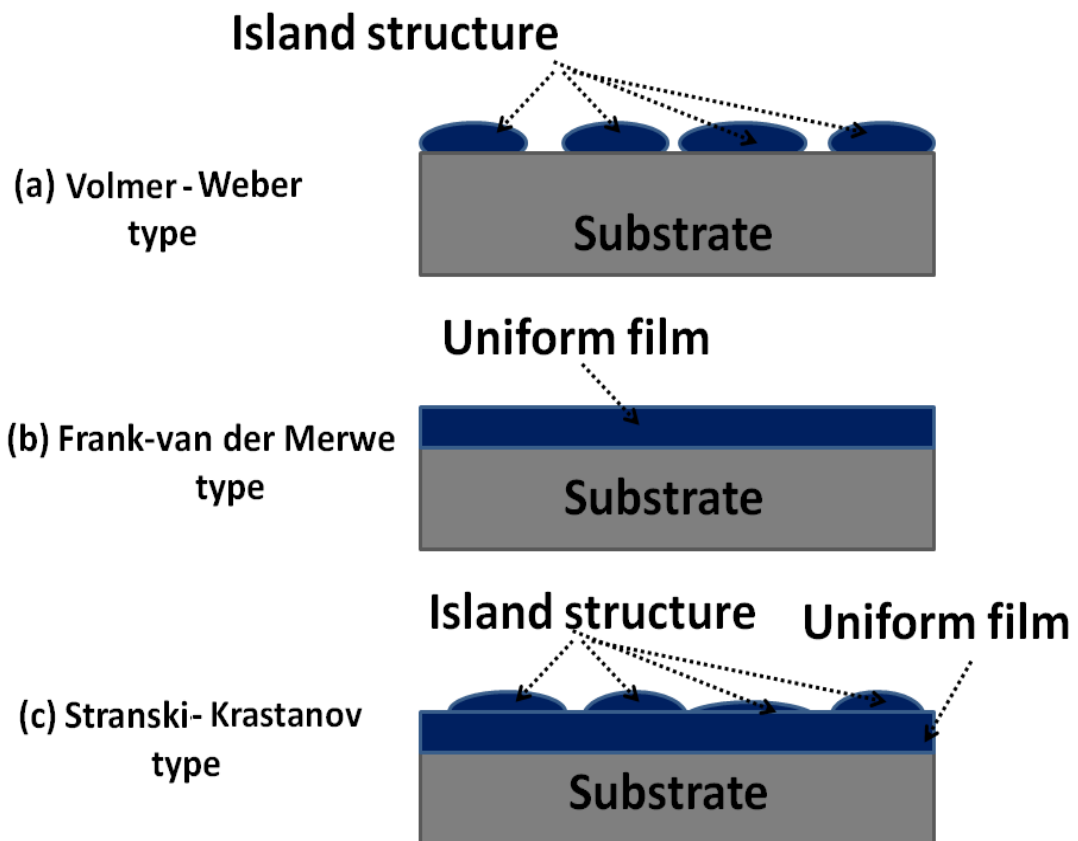


Figure 2.4: Three modes of the thin film growth processes [11].

## 2.2 Typical experimental set-up

The deposition system is comprised of the following elements, chamber, target manipulation, substrate holder with heater, pump, gas flow and vacuum gauging. A typical set-up for PLD is schematically shown in Figure 2.5. In an ultrahigh vacuum (UHV) chamber, elementary or alloy targets are struck at an angle of  $45^\circ$  by a pulsed and focused laser beam. The atoms and ions ablated from the target are deposited on substrates. Mostly, the substrates are attached with the surface parallel to the target surface at a target-to-substrate distance of typically 2-10 cm. Figure 2.6 shows, the PLD system at the National Laser Centre (NLC, CSIR), Pretoria which was used for this project. Moreover, Figure 2.7 shows the in-house build sample holder which was used as target when the powder was pressed without binders.

## 2.3 Versatility of the PLD technique

During PLD, many experimental parameters can be changed, which then have a strong influence on the film properties. First, the laser parameters such as the laser fluence, wavelength, pulse duration and repetition rate can be altered. Secondly, the preparation conditions, including target-to-substrate distance, substrate temperature, background gas and pressure, may be varied, which all influence the film growth. In the following sections, we focus on the most critical of these parameters.

### 2.3.1 Laser wavelength

The useful range of laser wavelength for thin film growth by PLD lies between 200 nm and 400 nm. This is because most materials exhibit strong absorption in this spectral region [6]. The absorption coefficients tend to increase as one

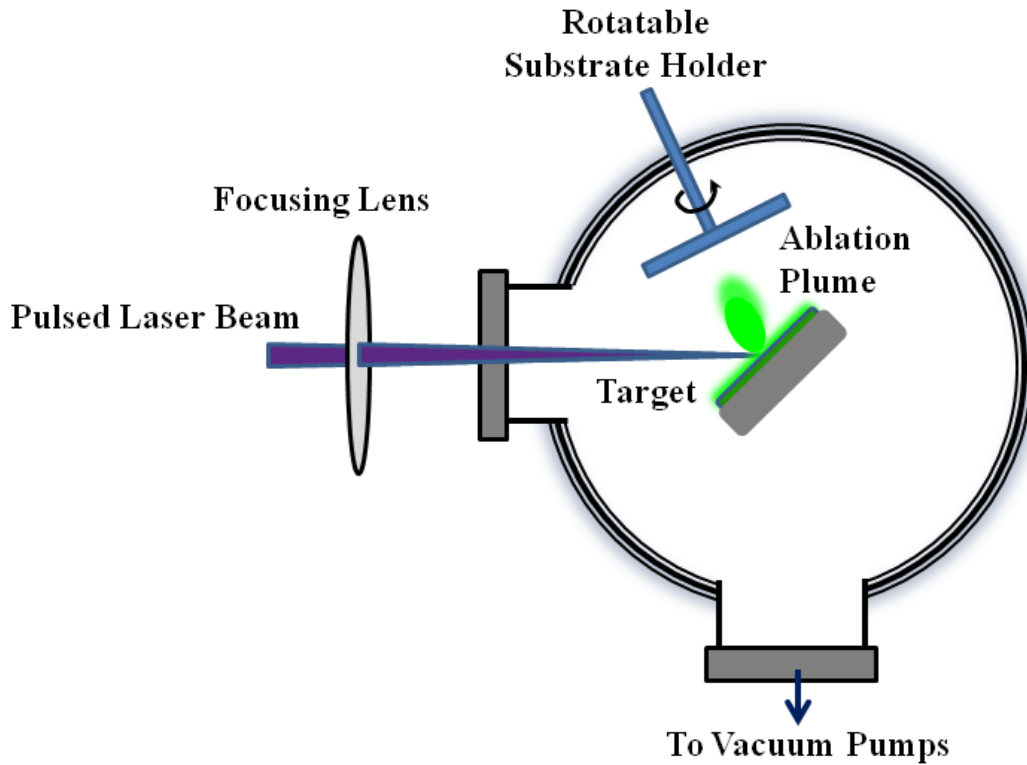


**Figure 2.5:** Schematic diagram of a PLD system

moves to the short wavelength end of this range and the penetration depths into the target materials are correspondingly reduced. This is a favourable situation because thinner layers of the target surface are ablated as one moves closer to the 200 nm mark [6]. The  $\text{Nd}^{3+}$ :YAG laser with a wavelength of 266 nm was used as the deposition source in this project.

### **2.3.2 High vacuum (HV) and different gas atmospheres**

A background gas can be utilized to reduce the kinetic energy of the plume species and to increase the number of chemical reactions between the plume and gas.

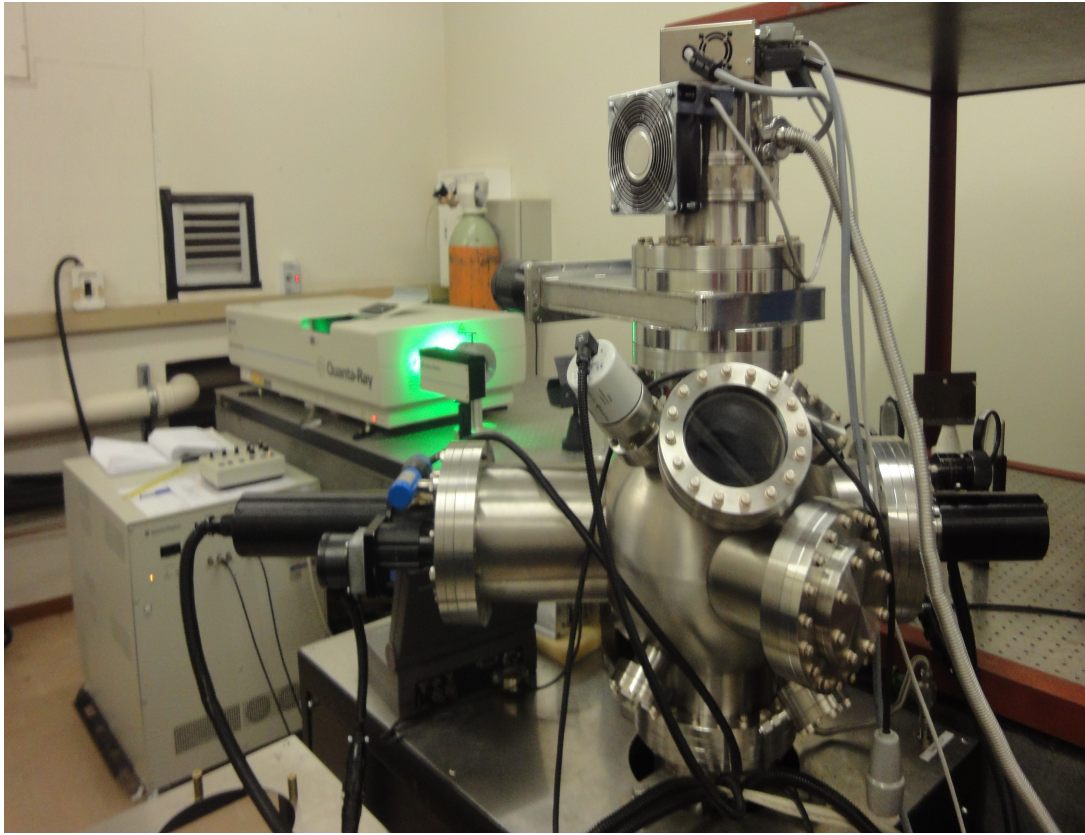


**Figure 2.6:** The PLD system at the National Laser Centre (NLC, CSIR), Pretoria.

### 2.3.3 Stoichiometry transfer

One of the most important and enabling characteristics in PLD is the ability to realize stoichiometric transfer of ablated material from multiple targets for many materials. This arises from the nonequilibrium nature of the ablation process itself due to absorption of high laser energy density by a small volume of material.

## 2.4 Limitations and advantages of PLD

Some advantages [12]:



**Figure 2.7:** In-house build sample holder that was used for PLD.

1. Conceptually simple: a laser beam vaporizes a target surface, producing a film with the same composition as the target.
2. Versatile: many materials can be deposited in a wide variety of gases over a broad range of gas pressures.
3. Fast: high quality sample can be grown reliably in 10 to 30 minutes.

Some limitations:

1. Particulates:

The micrometer and sub-micrometer sized particulates which are present on both surface and inside of the films structure, stand as the main drawback of the PLD, in view of technological applications. The origin of these particulates was associated with different physical mechanisms that are initiated during the laser radiation-target material interaction, such as [13, 14]:

- (a) Gas phase condensation (clustering) of the evaporated material;
- (b) Liquid phase expulsion, under the action of the recoil pressure of the ablated substance (vapour and plasma);
- (c) Blast-wave explosion at the liquid (melt)-solid interface;
- (d) Hydrodynamic instabilities developing across the liquid targets surface.

2. Composition and thickness depend on deposition conditions:

The composition and thickness depend on many deposition conditions. The processing parameters, such as wavelength, energy and shape of the laser pulse, process atmosphere, substrate temperature and other parameters. Therefore, for favourable film with specific composition and thickness, optimization of these parameter are required [15].

3. Difficult scale-up to large wafers:

Is one problem with PLD where the material flux is both directional and has a small radius [16]. Figure 2.8 shows developments in the PLD system to overcome the small area of the thin film. Figure 2.8 shows a schematic of such a system. A mirror held in a kinematic mirror mount rasters the incident laser across a large-diameter rotating ablation target, using a programmable linear actuator. The substrate is located just offset from the target and is, of course, rotated as well [17].

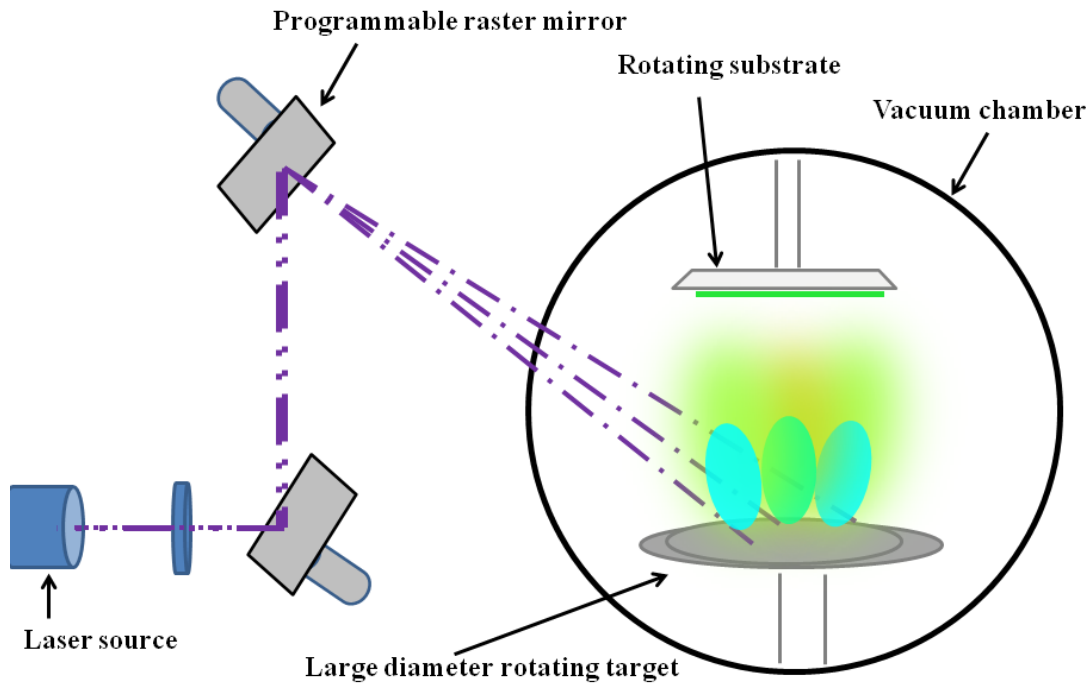


**Figure 2.8:** Schematic of a large-area PLD system utilizing laser rastering over large-diameter targets [17].

## 2.5 Luminescent materials

These are solid materials that emit light, or luminesce, when exposed to radiation such as ultraviolet light or an electron beam. Hundreds of thousands of luminescent minerals have been synthesized, each one having its own characteristic color of emission and period of time during which light is emitted after excitation ceases [18]. Figure 2.9 display different kinds of luminescent materials during the day light and when they were excited by electrons or ultraviolet (UV) radiation.

Luminescent materials consists of two parts:

1. **Host lattice:**

A host is regarded as the "home" of optically active ions. It is necessary to optimize the distribution of the activators and prevent rapid non-radiative

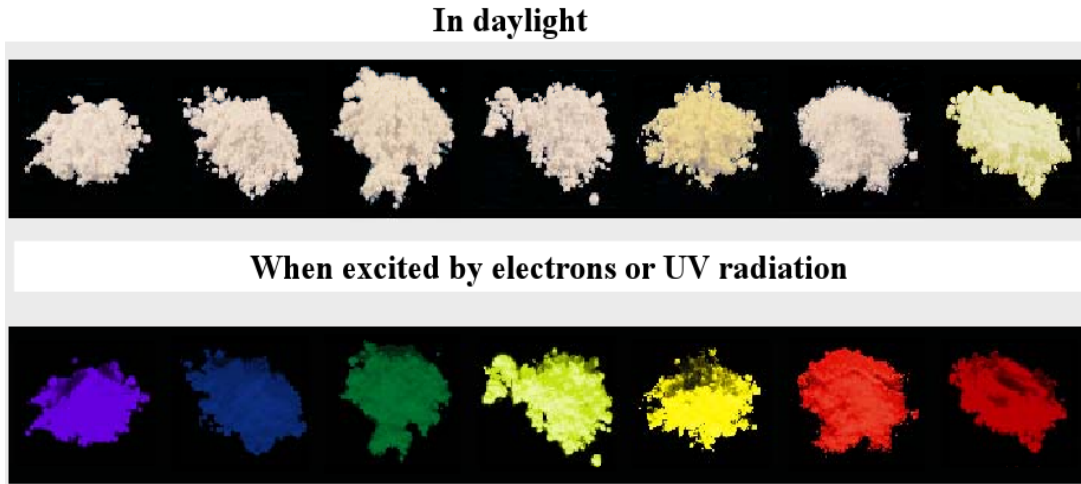


**Figure 2.9:** Different kind of phosphor materials in the day light and when excited it by ultraviolet or electron sources.

processes from occurring. Since dopant ions in a solid host are impurities embedded in the host lattice, the host ions are substitutionally replaced by dopant ions. Therefore, the host lattice determines the distance between the dopant ions as well as their relative spatial position. The host materials generally require close lattice matches, and the valence of the host cation should be the same or similar to those of dopant ions in order to prevent the formation of crystal defects and lattice stresses arising from doping [19].

In this project, yttrium aluminium garnet  $\text{Y}_3\text{Al}_5\text{O}_{12}$  material, usually abbreviated as YAG, was used as host. This material has widely been used as a host lattice for lanthanide ions to produce phosphors emitting a variety of colors, especially in the green emission range [20 - 21]. It can withstand a high-energy electron beam and has been considered as an ideal candidate to prepare display phosphors. YAG is a body-centered cubic lattice, space group Ia3d. In the YAG crystal the  $\text{Al}^{3+}$  ions are surrounded by  $\text{O}^{2-}$  ions in a tetrahedral and octahedral arrangements leading to  $\text{AlO}_5^{-4}$  and  $\text{AlO}_9^{-9}$  anionic clusters respectively.  $\text{Y}^{3+}$  ions are surrounded by eight  $\text{O}^{2-}$  ions

forming a decahedron (distorted cube). Furthermore, YAG is a host with excellent structural compatibility. Inner  $Y^{3+}$  and  $Al^{3+}$  can to a certain extent be substituted by many kinds of cations with different sizes and valency. A portion of Al substituted by Ga leading to  $Y_3(Al_{1-y}, Ga_y)_5O_{12}$  structure, where eight oxygen ions are nearest neighbors of  $Y^{3+}$  they belong to two different anionic groups  $(Al_{1-y}, Ga_y)_5^{4-}$  and  $(Al_{1-y}, Ga_y)_9^{6-}$  [21] as presented in Figure 2.10.

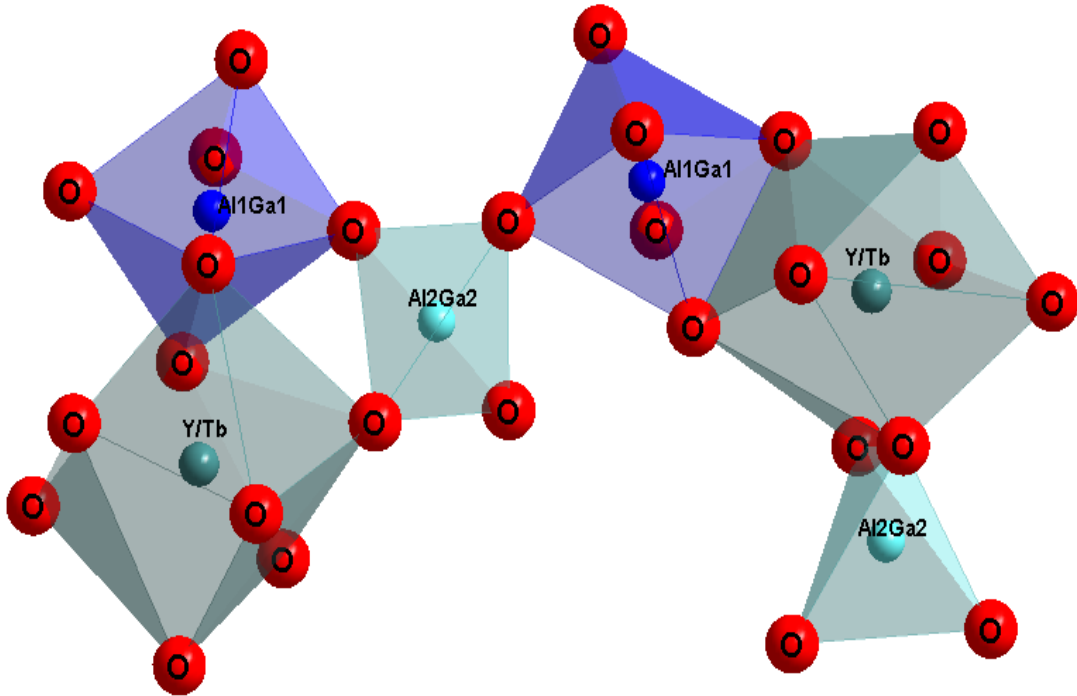


**Figure 2.10:** The arrangement of Y, O, Al and Ga described with polyhedral in  $Y_3(Al, Ga)_5O_{12}:Tb$  (ICSD-29248)

## 2. A luminescent center:

A luminescent center is the heart of the phosphor that luminesces when energy has been absorbed [22]. The luminescent impurities are incorpo-

rated intentionally into a host lattice with the optimal concentration. The appropriate luminescent center can be selected according to the emission color, ionic valence, atomic radius and the efficiency. The rare-earth or lanthanide elements ( $\text{Ce}^{3+}$ ,  $\text{Pr}^{3+}$ ,  $\text{Nd}^{3+}$ ,  $\text{Sm}^{3+}$ ,  $\text{Sm}^{2+}$ ,  $\text{Eu}^{3+}$ ,  $\text{Eu}^{2+}$ ,  $\text{Gd}^{3+}$ ,  $\text{Tb}^{3+}$ ,  $\text{Dy}^{3+}$ ,  $\text{Er}^{3+}$ ,  $\text{Ho}^{3+}$ ,  $\text{Tm}^{3+}$ ,  $\text{Yb}^{3+}$ ,  $\text{Yb}^{2+}$ ) as luminescence centers have been confidently detected and interpreted [23].

Some of these elements exhibit luminescence originating from electronic transitions from one f-orbital electron to another f-orbital electron state. This luminescence showing very sharp emission lines due to the f-orbitals are shielded from the crystal field by outer  $5s^2$  and  $5p^6$  shell orbitals. This shielding is the reason that the rare-earth have very interesting luminescence properties.

In this project,  $\text{Tb}^{3+}$  ion was used as the luminescent center with the luminescence spectra consisting of many lines due to  $^5\text{D}_j - ^7\text{F}_j$  transitions. The intensity of the emissions from  $^5\text{D}_3$  decreases with increasing  $\text{Tb}^{3+}$  concentration due to cross-relaxation [23]. Among the emission lines from the  $^5\text{D}_4$  state, the  $^5\text{D}_4 - ^7\text{F}_5$  emission line at approximately 544 nm is the strongest in nearly all host crystals when the  $\text{Tb}^{3+}$  concentration is high. The reason is that this transition has the largest probability for both electric-dipole and magnetic-dipole induced transitions. The  $\text{Tb}^{3+}$  emission has a broad excitation band in the region from 220 to 300 nm originating from the  $4f^8 - 4f^7 5d^1$  transition [23]. Figure 2.11 shows the emission of  $\text{Y}_3(\text{Al}, \text{Ga})_5\text{O}_{12}:\text{Tb}$  powder under 267 nm excitation.

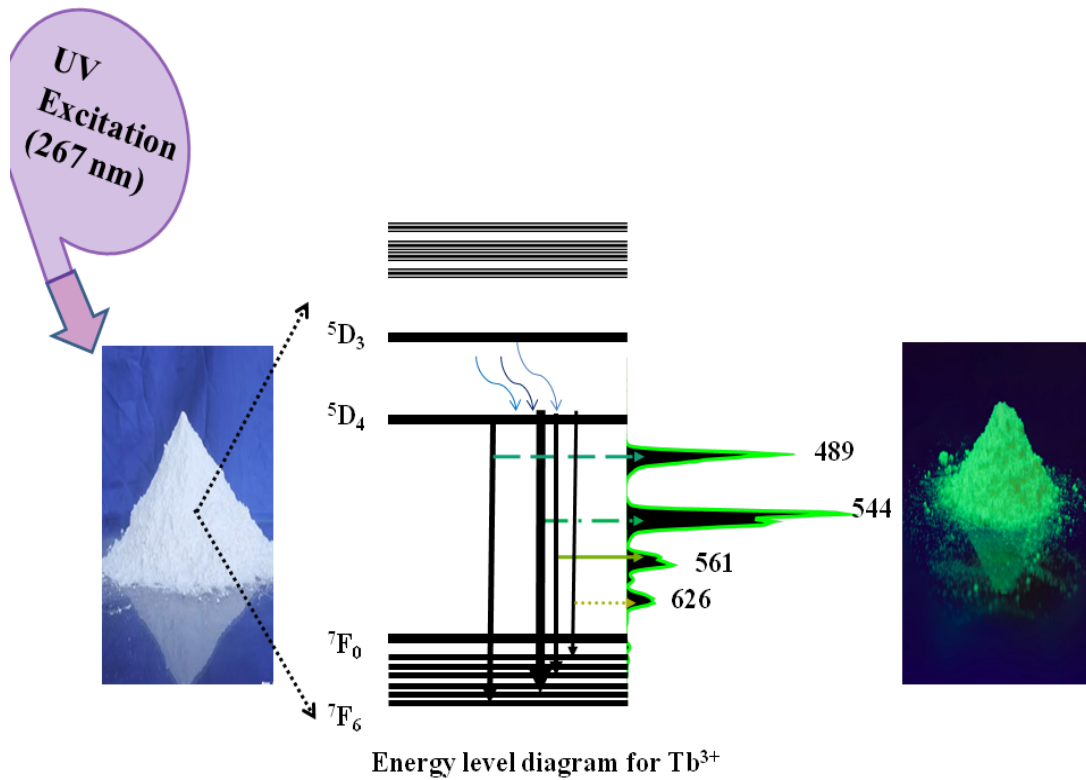


**Figure 2.11:** Emission of Y<sub>3</sub>(Al, Ga)<sub>5</sub>O<sub>12</sub>:Tb powder under 267 nm excitation.

## References

- [1] <http://en.wikipedia.org/wiki/Ablation> (accessed 3.12.2013).
- [2] S. Logothetidis, Nanostructured materials and their applications, Springer-Verlag Berlin Heidelberg (2012).
- [3] E. Morintale, C. Constantinescu, M. Dinescu, Physics AUC **20** (2010) 43.
- [4] D. Chrisey, G. K. Hubler, Pulsed laser deposition of thin films, Wiley, New York **154-155** (1994).
- [5] X. Yang, Y. Tang, M. Yu, Q. Qin, Thin Solid Films **358** (2000)187.

- [6] D. B. Chrisey, G. K. Hubler, Pulsed laser deposition of thin film, Naval research laboratory, Washington, D. C. John wiley& sons, Inc. 1994
- [7] M. S. Rogers, Laser-material Interaction: From Applications of Pulsed Laser Deposition to the Fundamental Heat Affected Zone, UMI Microform International 2008.
- [8] T. Haugan, P. N. Barnes, L. Brunke, I. Maartense, J. Murphy, Physica C **397** (2003) 47.
- [9] A. V. Bulgakov, N. M. Bulgakova, Journal of Physics D: Applied Physics **31** (1998) 693.
- [10] E. Morintale1, C. Constantinescu, M. Dinescu, Physics AUC **20** (2010) 43.
- [11] K. Wasa, M. Kitabatake, H. Adachi, Thin film Materials Technology: Sputtering of Compound Materials, William Andrew, Inc. 2004.
- [12] K. K. Chattopadhyay, A. N. Banerjee, Introduction to Nanoscience and Nanotechnology, PHI Learning Private Limited, New Delhi 2009.
- [13] E. Gyorgy, I.N. Mihailescu, M. Kompitsas, A. Giannoudakos, Applied Surface Science **195** (2002) 270.
- [14] E. Gyorgy, I. N. Mihailescu, M. Kompitsas, A. Giannoudakos, Thin Solid Films **446** (2004) 178.
- [15] G. Korotcenkov, Chemical Sensors: Fundamentals of Sensing Materials, Momentum Press, LLC. 2010.
- [16] D. P. Norton, Pulsed Laser Deposition of Complex Materials: Progress Towards Applications, John Wiley & Sons, Inc. 2007.

- [17] R. Eason, Pulsed Laser Deposition of Thin Films: Applications-Led Growth of Functional Materials, John Wiley & Sons, Inc. (2007).
- [18] <http://global.britannica.com/EBchecked/topic/457505/phosphor> (accessed 07.10.2013).
- [19] Y. Zhang, J. Hao, Journal of Materials Chemistry C **1** (2013) 5607
- [20] Z. N. Fei, L. Y. Xiang, Y. X. Feng, Chinese Physical letter **25** (2008) 703.
- [21] A. Mayolet, W. Zhang, E. Simoni, J. C. Krupa, P. Martin, Journal of Optical Materials **4** (1995) 757.
- [22] B. L. Brakefield, S. Gollub, D. G. Walker, Journal of Young Scientists **3** (2013).
- [23] M. Gaft, R. Reisfeld, G. Panczer, Modern Luminescence Spectroscopy of Minerals and Materials, Springer-Verlag Berlin Heidelberg 2005.

## Chapter 3

### Film and powder characterization techniques

This chapter gives a brief account of the characterization techniques including X-ray Diffraction (XRD) for structural analysis; the photoluminescence (PL) and cathodoluminescence (CL) spectroscopies for luminescence measurements; atomic force microscopy (AFM) and scanning electron microscopy (SEM), for morphological and topographical analysis; Auger electron spectroscopy (AES) and X-ray photoelectron spectroscopy (XPS) for elemental composition analyses.

#### 3.1 The XRD technique

The powders and the thin films layers were studied by the XRD technique which is used to identify the crystalline phases present in the materials. In this technique a monochromatic X-ray beam with wavelength  $\lambda$ , on the order of lattice spacing  $d$ , is projected onto a crystalline material at an angle  $\theta$ , XRD peaks are produced by constructive interference of monochromatic beam scattered from each set of lattice planes at specific angles. Constructive interference gives the diffraction peaks according to Braggs law (equation 3.1) which is illustrated in Figure 3.1 [1]

$$2d_{hkl} \sin \theta_{hkl} = n\lambda \quad (3.1)$$

By varying the angle  $\theta$ , the Braggs Law condition is satisfied by different  $d$ -spacing in polycrystalline materials. Plotting the angular position and intensities of the resultant diffracted peaks of radiation produces a pattern, which is the characteristic of the material. Figure 3.1 shows the characteristic pattern of the  $Y_3(Al, Ga)_5O_{12}:Tb$  powder.

In this study, The Bruker AXS D8 ADVANCE X-ray diffractometer (Figure 3.2) with a Cu anode produce X-rays with a wavelength of  $\lambda = 1.5406 \text{ \AA}$  was used.

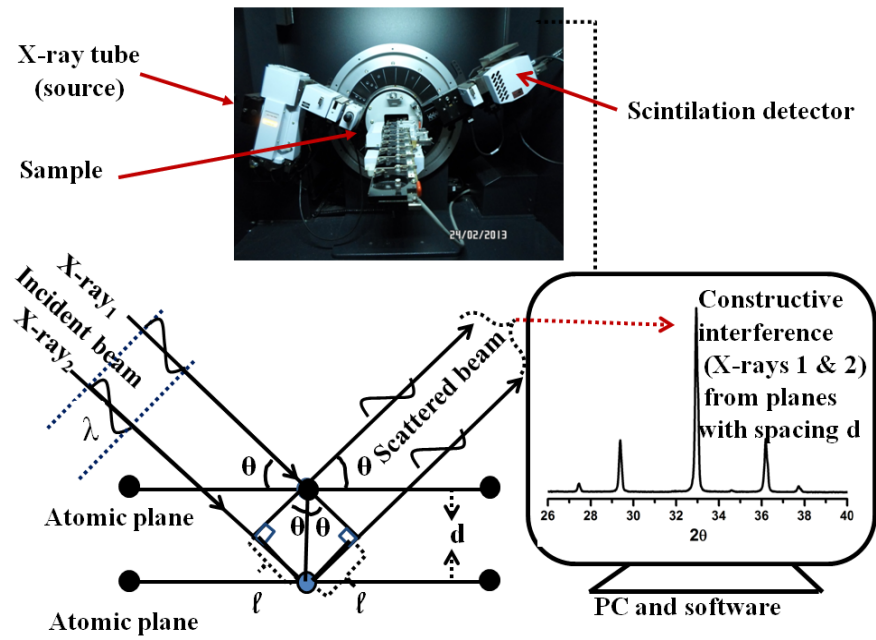


**Figure 3.1:** The schematic diagram of Bragg's law.



**Figure 3.2:** A photo of the Bruker AXS D8 ADVANCE X-ray diffractometer at the Department of Physics of the University of the Free State.

For monochromatic x-rays, Nickel was used as a filter which is strongly absorbs the x-rays below  $1.5 \text{ \AA}$  (Figure 3.3). Moreover, the system was operated at a voltage of 40 kV and a current of 40 mA.

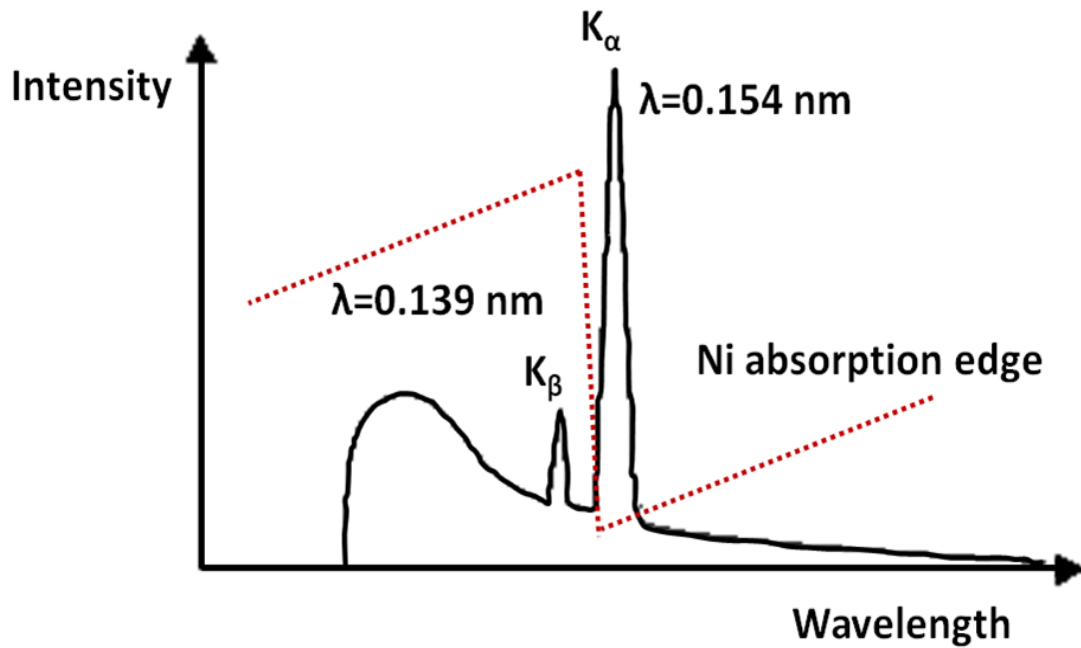


**Figure 3.3:** Diagram illustrates the characteristic X-ray emission obtained from a copper (Cu) target with nickel (Ni) filter [18].

### 3.2 Photoluminescence (PL)

The PL means persisting light emission from a substance after the exciting radiation has ceased. This light can be detected and recorded using the PL spectroscopy technique. Two types of luminescence spectra can be distinguished: excitation and emission. In the case of an excitation spectrum, the wavelength of the exciting light is varied while the intensity of the emitted light are fixed at specific emission wavelength. On contrary for the emission case, the wavelength of the emission light is varied and the intensity of the excited light is fixed at a specific excited wavelength. The emission and excitation spectra for the

powder and thin film samples, in this project, are recorded using a Cary Eclipse fluorescence spectrophotometer as presented in Figure 3.4. Moreover, the PL measurements were recorded at room temperature using a monochromatized Xenon flash lamp as an excited source.



**Figure 3.4:** Cary Eclipse fluorescence spectrophotometer at the Department of Physics of the University of the Free State.

### 3.3 The XPS technique

The XPS technique, also known as Electron Spectroscopy for Chemical Analysis (ESCA), is a powerful technique widely used for the surface analysis of materials. At low energy resolution it provides qualitative and quantitative information on the elements present. At high energy resolution it gives information on

the chemical state and bonding of those elements [2, 3]. In this technique the sample is irradiated with monochromatic X-rays and the resulting intensities and kinetic energies (KE) of the photoelectrons ejected from the surface are recorded as illustrated in Figure 3.5. From the KE it is possible to calculate the corresponding binding energies (BE) from knowledge of the incident photon energy ( $h\nu$ ) and the work function of the spectrometer ( $\Phi_s$ ) as it is shown in equation (3.2) [2, 4]

$$\text{KE} = h\nu - \text{BE} - \Phi_s \quad (3.2)$$

Since the binding energies of core electrons are characteristic for elements in a certain chemical environment, XPS allows for a determination of the atomic compositions of a sample. The shifts in the binding energies also provide information regarding the chemical state of elements being analyzed. A depth profile of the sample in terms of XPS quantities can be obtained by combining a sequence of ion gun etch cycles interleaved with XPS measurements from the current surface. An ion gun is used to etch the material for a period of time before being turned off whilst XPS spectra are acquired. Each ion gun etch cycle exposes a new surface and the XPS spectra provide the means of analyzing the composition of these surfaces [3].

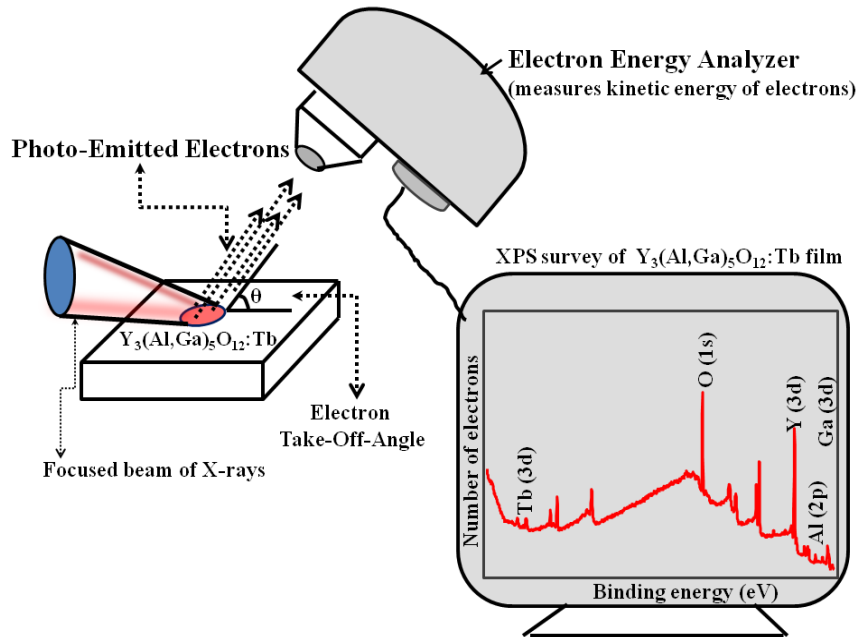


**Figure 3.5:** The schematic diagram of XPS with a survey of the  $Y_3(Al, Ga)_5O_{12}:Tb$  film.



**Figure 3.6:** PHI 5400 Versaprobe scanning XPS unit at the Department of Physics of the University of the Free State.

The XPS measurements in this study were performed on a PHI 5400 Versaprobe scanning XPS (Figure 3.6). The XPS surveys were done with 100  $\mu\text{m}$ , 25 W and 15 kV Al monochromatic X-ray beam. The depth profiles were done with 2 kV, 2  $\mu\text{A}$   $2 \times 2$  mm raster-Ar ion gun of sputtering rate of about 8.5 nm per min.

### 3.4 The AES technique

The AES is an analytical technique used to determine the elemental composition and the chemical state of the atoms in the surface of a solid material. The use of AES involves precise measurements of a number of emitted secondary electrons as a function of kinetic energy. Auger electrons are produced when incident radiation interacts with an atom, and a secondary electron is generated. As a result, a vacancy will be left in an ionized atom's electron shell. To fill this vacancy, an electron from a higher energy outer shell can drop down to fill the vacancy. This creates exceeding energy in the atom which can be corrected by emitting an outer electron, defined as an Auger electron, Figure 3.7 illustrate the emission of a specific Auger electron via a  $\text{KL}_{2,3} \text{L}_1$  transition. Furthermore, Auger kinetic energy (KE) is given by

$$\text{KE} = E_{\text{K}} - E_{\text{L}_1} - E_{\text{L}_{2,3}} - \Phi \quad (3.3)$$

Where, the notation K,  $\text{L}_1$  and  $\text{L}_{2,3}$  refers to location of core hole (1s), origin of relaxing electron (2s) and Auger electron (electron that leaves ion) respectively, and  $\Phi$  represents the work function of the analyzer material.

Because the transition probabilities between singly ionized and doubly ionized state of the atom [5], equation (3.3) is not so simple.

By use of the expression (3.3) the Auger kinetic energy KE is over estimated by

Chung and Jenkins [6] as:

$$KE(Z) = E_K(Z) - 0.5[E_{L_1}(Z) + E_{L_1}(Z + \Delta)] - 0.5[E_{L_{2,3}}(Z) + E_{L_{2,3}}(Z + \Delta)] - \Phi \quad (3.4)$$

where  $Z$  is the atomic number of the atom involved, The  $\Delta$  term appears because the energy of the final doubly ionized state is somewhat larger than the sum of the energies for individual ionization of the same levels.

Auger electrons have a characteristic energy unique to the element from which they are emitted and can be used to give compositional information about the target sample [1, 7, 8]. The intensity and energy distribution of the Auger electrons which are recorded in the experiment usually contain not only Auger electrons but all the other emitted electrons, the Auger peaks being superimposed, as weak features, on an intense background. For this reason the differential spectrum is often recorded rather than the direct energy spectrum. Comparison of direct and differential Auger spectra for  $Y_3(\text{Al, Ga})_5\text{O}_{12}:\text{Tb}$  thin film are represented in Figure 3.8.

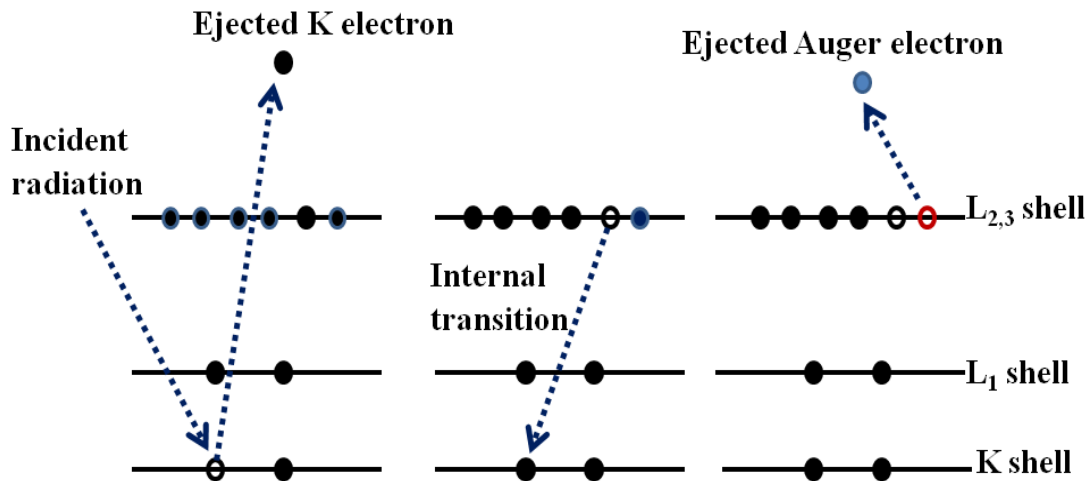


**Figure 3.7:** Relaxation of the ionized atom by the emission of a  $KL_{2,3} L_{2,3}$  Auger electron.

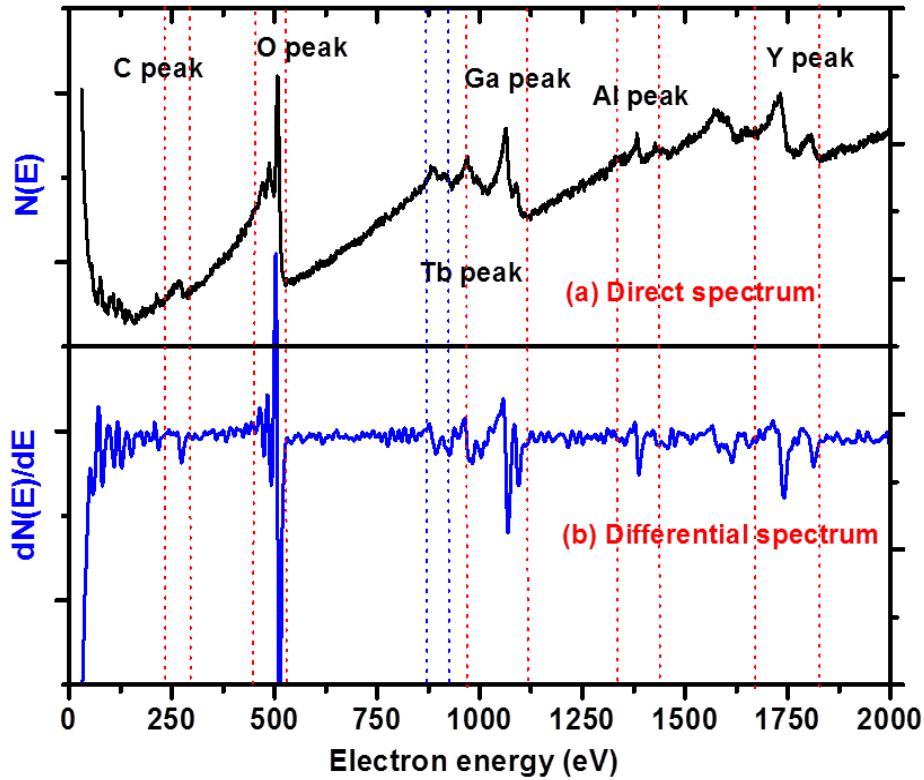


**Figure 3.8:** Comparison of (a) direct, and (b) differential Auger spectra for  $Y_3(Al, Ga)_5O_{12}:Tb$  thin film.

Auger depth profiling is also possible by recording the Auger peak-to-peak height (APPH's) of the Auger signals as a function of sputter erosion depth. With AES it is also possible to produce high resolution chemical maps which have important applications in identifying the precise chemical nature of particles or small features. Typical AES mapping of  $Y_3(Al, Ga)_5O_{12}:Tb$  thin films are presented in Figure 3.9 with a combination of O (red), Y (blue) and Ga (green). Quantification of the major and minor elements are also possible by using the appropriate Auger relative sensitivity factors, although it is less accurate but is highly useful. The atomic concentration ( $C_x$ ) of an element  $x$  in a sample is given by [9]

$$C_x = \frac{(APPH)_x / (APPH)_x^\infty}{\sum_i (APPH)_i / (APPH)_i^\infty} \quad (3.5)$$

here  $(\text{APPH})_i^\infty$  is the Auger signal from a pure elemental standard measured under identical conditions, also known as sensitivity factor.

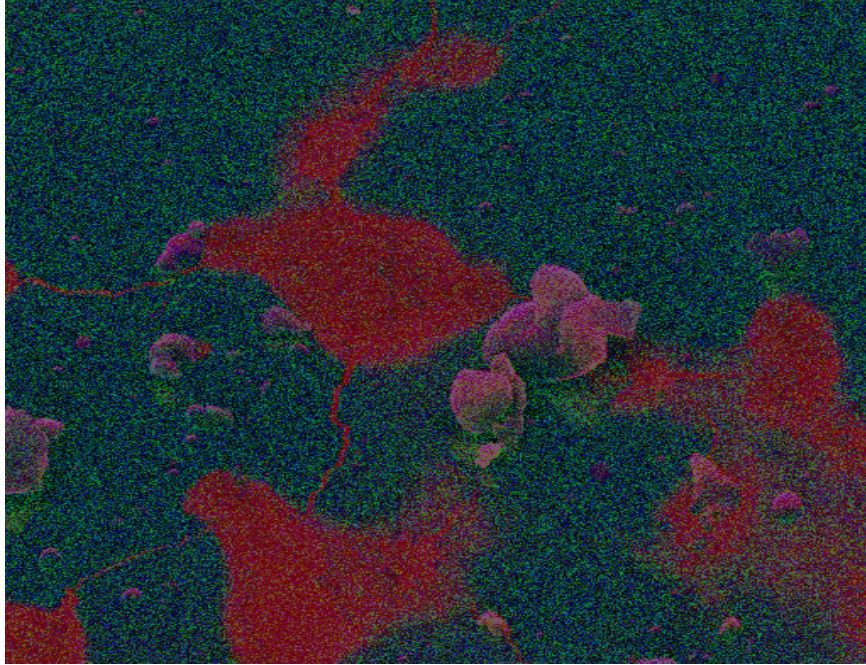


**Figure 3.9:** Typical AES mapping of  $\text{Y}_3(\text{Al, Ga})_5\text{O}_{12}:\text{Tb}$  thin films with combination of O (red), Y (blue) and Ga (green).

The Auger measurements in this study were performed on a PHI, model 549 (Figure 3.10), AES and PHI 700 nano scanning Auger electron microprobe (NanoSAM) (Figure 3.11). For the measurement that was done in PHI 549 system, the phosphor was subjected to an electron beam of current density of  $38.1 \text{ mA cm}^{-2}$ , with a working beam voltage of 2 keV and a beam current of  $10 \mu\text{m}$ . The electron beam irradiation was prolonged for 27 hrs at a background pressure of  $2.3 \times 10^{-8}$  Torr and an  $\text{O}_2$  pressure of  $1 \times 10^{-6}$  Torr. For the measurement that was done in NanoSAM system, the images and the AES surveys were done with 25 kV and 10 nA electron beam. The depth profiles sputtered with 2 kV  $2 \mu\text{A}$  ion beam,  $2 \times 2 \text{ mm}$  raster area and the sputter rate of about 8.5 nm per min.

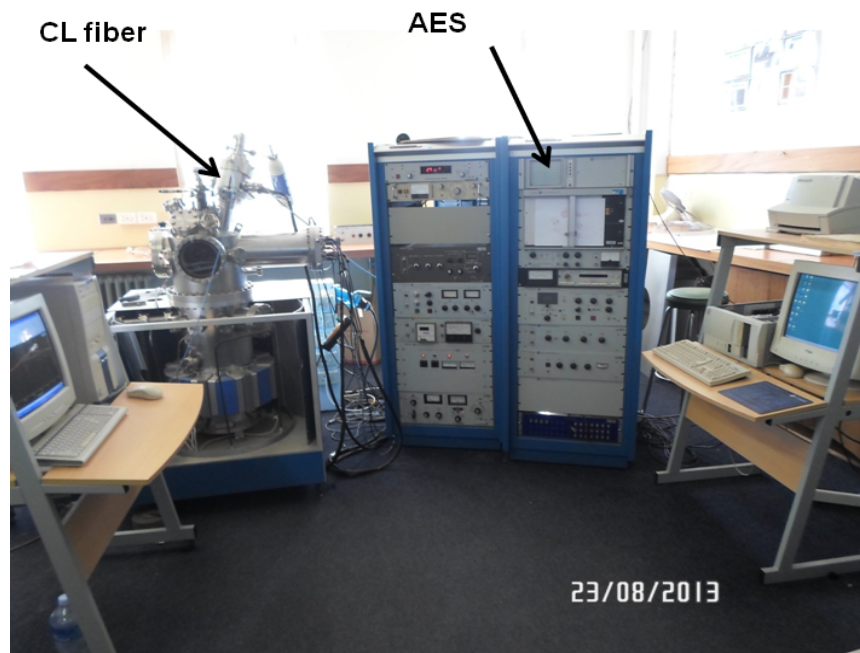


**Figure 3.10:** PHI, model 549, AES unit at the Department of Physics of the University of the Free State.



**Figure 3.11:** The PHI 700 Auger Nanoprobe SEM unit at the Department of Physics of the University of the Free State.

### 3.5 The AFM technique

The AFM is a powerful tool allowing a variety of surfaces to be imaged and characterized at the atomic level [10]. The AFM raster scans a sharp probe over the surface of a sample and measures the changes in Van der Waals force between the probe tip and the sample. Figure 3.12, illustrates the working concept for an atomic force microscope. A cantilever with a sharp tip is positioned above a surface. Depending on this separation distance, long range or short range forces will dominate the interaction as is it shows in Figure 3.13. This force is measured by the bending of the cantilever by an optical lever technique: a laser beam is focused on the back of a cantilever and reflected into a photodiode. By calculating the difference signal in the photodiode quadrants, the amount of deflection  $[(A+B)-(C+D)]$  can be correlated with a height. Because the cantilever obeys Hooke's Law for small displacements, the interaction force between the tip and the sample can be determined from the equation [11],

$$F = -KZ \tag{3.6}$$

Where  $F$  is Van der Waals force,  $K$  is spring constant (stiffness) of the cantilever and  $Z$  is cantilever deflection.

The movement of the tip or sample in the  $x$ ,  $y$ , and  $z$ -directions is controlled by a piezoelectric crystal which creates a voltage if pressure is applied, or in reverse, can create a pressure by expanding or contracting if a voltage is applied (See Figure 3.14 ). Using the contraction and expansion of the crystal, the configuration in a scanner allows for the controlled movement on the order of a fraction of a nanometre [12].

There are many modes in AFM, for an example, in constant force mode (or contact mode) the feedback system provides a constant value of the cantilever bend, and consequently, of the interaction force. Thus, deflection signal is kept on the present value. Change of topography affects the deflection signal. To

keep it constant, the feedback system changes voltage applied to the Z-electrode of the scanner. Thus, changes of this voltage will be proportional to the surface topography.

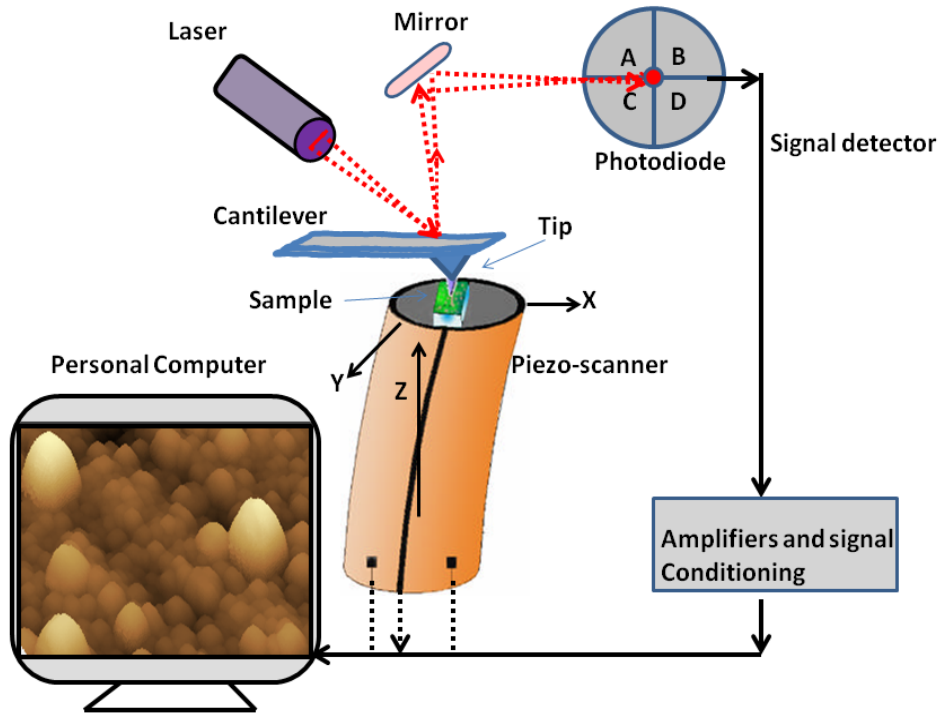


**Figure 3.12:** Scheme of an atomic force microscope.

In this work, the surface topography and roughness were examined from images captured in contact mode using a Shimadzu SPM-9600 AFM as is shown in Figure 3.15. The root mean square (RMS) roughnesses were estimated by analyzing the topography scans of the films surfaces using commercial software.

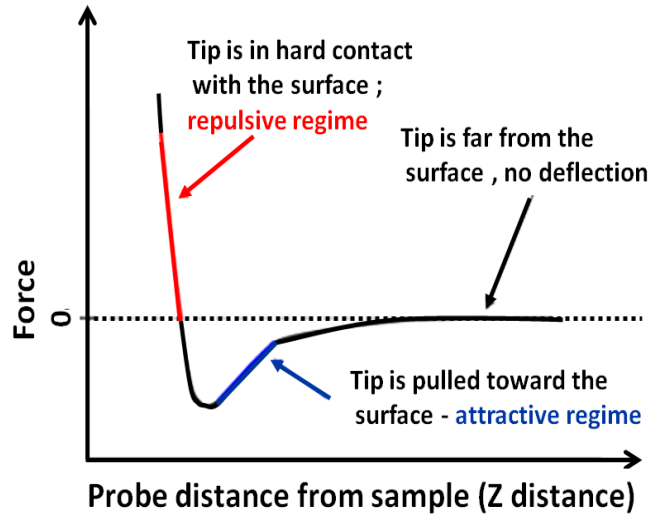


**Figure 3.13:** The force-distance curve characteristic of the interaction between the tip and sample.

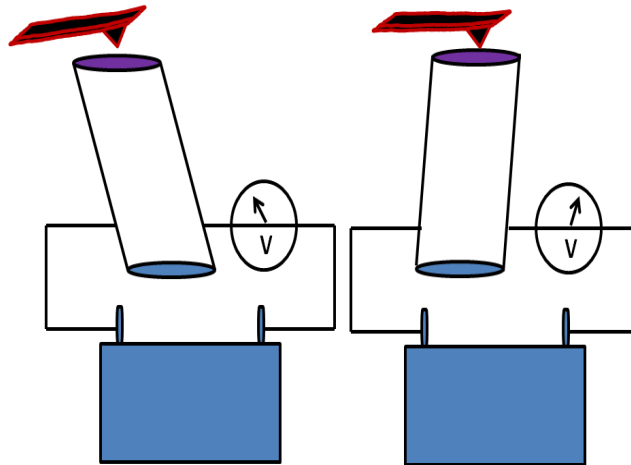


**Figure 3.14:** A piezoelectric crystal create a pressure by expanding or contracting if a voltage is applied



**Figure 3.15:** Shimadzu SPM-9600 AFM at the Department of Physics of the University of the Free State.

## 3.6 Scanning Electron Microscopy (SEM)

Electron microscopes are scientific instruments that use a beam of energetic electrons to examine objects on a very fine scale. The characteristic information that can be achieved by SEM are topography and morphology information. The topography means the surface features of an object or "how it looks" i.e. texture, whereas morphology means the shape and size of particles making up the object.

The principle of SEM is based on the interaction of an incident electron beam and the solid specimen. Figure 3.16 shows a simple explanation of SEM where the electron beams are emitted from a electron gun and are accelerated towards the specimens surface. The electron beam is focused by condenser lenses and is deflected by pairs of coils in the objective lens in raster fashion over the specimens surface. Electron bombardment can produce a wide variety of emissions from the specimen, including Auger electrons, backscattered electrons, secondary electrons, cathodoluminescence and X-rays etc. Backscattered and secondary electrons are used for generating the surface images. The most common imaging mode monitors low energy secondary electrons. Due to their low energy, these electrons originate within a few nanometres from the surface [13, 14]. The SEM measurements in this study were performed on a PHI 700 nano scanning Auger electron microprobe (NanoSAM) (Figure 3.11). The SEM images were done with 25 kV and 10 nA electron beam.

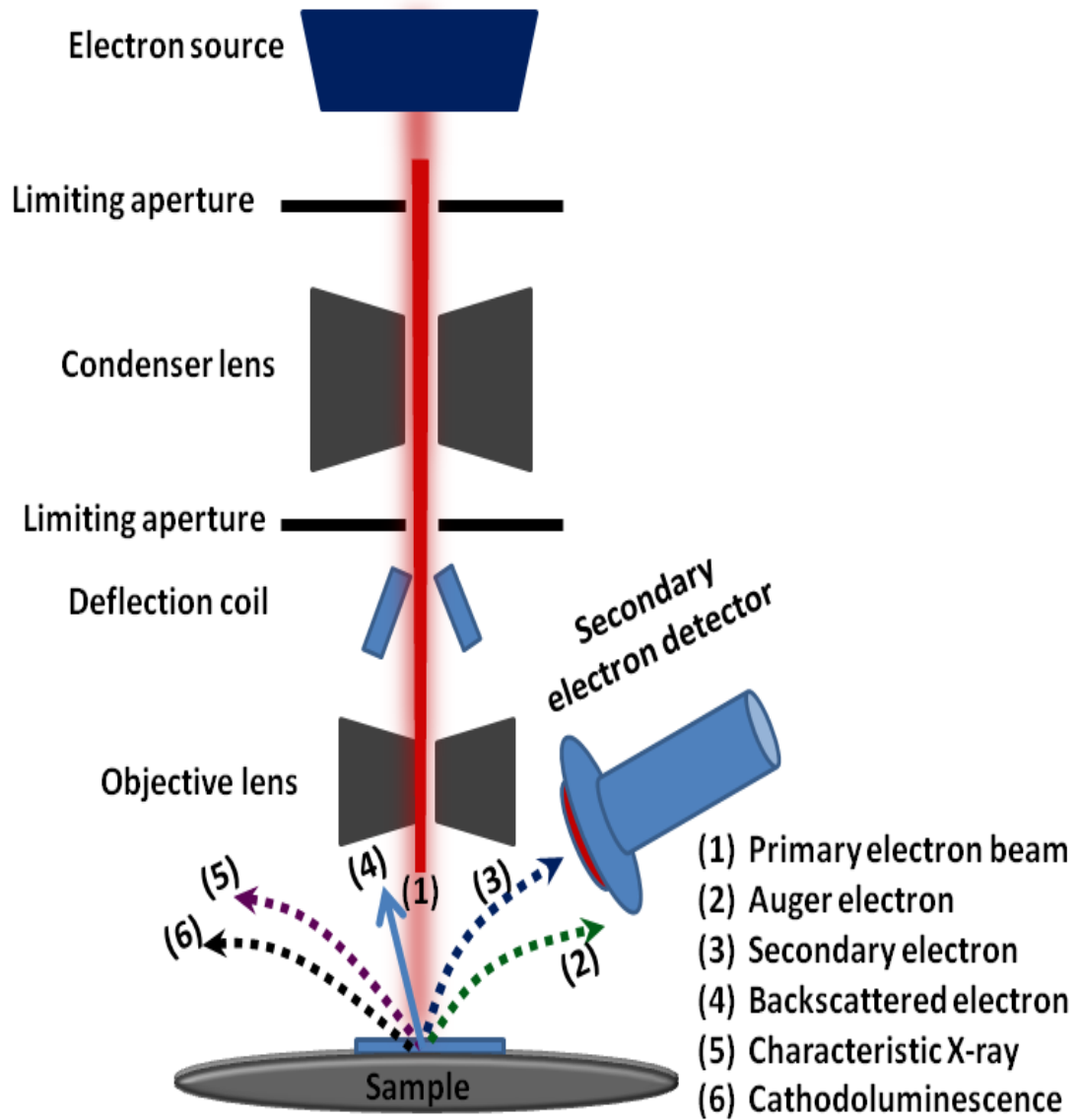


**Figure 3.16:** Schematic diagram of SEM and some type of signals available due to electron interaction

### 3.7 Cathodoluminescence (CL)

Cathodoluminescence (CL) refers to emission of characteristic light by a substance that is under bombardment by electrons, where the cathode is the source of the electrons as presented in Figure 3.16. This effect is produced in materials with at least some semiconductor properties when incident electrons knock a photoelectron into the "conduction band" of a material resulting in a positively charged "hole." The free electrons recombine with the holes to produce radiated light or heat in the sample. CL can be an intrinsic property of a material or the result of luminescent centers produced by trace impurities often rare-earth elements [15],  $Tb^{3+}$  for example produces green emission. The CL data were collected with a S200/PC2000/USB2000/HR2000 spectrometer type using OOI Base 32 computer software (See Figure 3.10). The powders were pressed into small holes of less than 1 mm that were drilled into a Cu sample holder. The phosphor was subjected to an electron beam of current density of  $38.1 \text{ mA cm}^{-2}$ , with a working beam voltage of 2 keV and a beam current of  $10 \mu\text{m}$ .

The next chapters contain the results obtained from this study. The chapters are presented in the form of papers and some repetition, especially in the introduction and experimental procedures may occur.

### References

- [1] J. F. Watts, J. Wolstenholme, An introduction to surface analysis by XPS and AES, 2003, John Wiley & Sons Ltd.
- [2] J. F. Moulder, W. F. Stickle, P. E. Sobol, K. D. Bomben, Handbook of X-ray Photoelectron Spectroscopy, 1995 (Japan: ULVAC-PHI, Inc. 370 Enzo, Chigasaki 253).

- [3] <http://www.dl.ac.uk/NCESS/xps/xps.htm> (accessed 22. 08. 2013).
- [4] <http://www.aystorm.com/techniques/xps.html> (accessed 22. 08. 2013).
- [5] F. P. Larkins, Applications of Surface Science, **13** (1982) 4.
- [6] L. H. Jenkins, M. F. Chung, Surface Science **28** (1971) 409.
- [7] <http://www.aystorm.com/auget.html> (accessed 22. 08. 2013).
- [8] J. L. Ong, L. C. Lucas, Biomaterials **19** (1998) 455.
- [9] J. M. Walls, Methods of Surface Analysis, Cambridge University Press **1** (1989), Issue 12.
- [10] A. Vilalta-Clemente, K. Gloystein, Physics of Advanced Materials, Winter School 2008.
- [11] <http://chemgroups.northwestern.edu/odom/nano-characterization/AFM%20more%20info.pdf> (accessed 26.08. 2013).
- [12] [http://www.weizmann.ac.il/Chemical\\_Research\\_Support/surflab/peter/afmworks/](http://www.weizmann.ac.il/Chemical_Research_Support/surflab/peter/afmworks/) (accessed 26.08. 2013).
- [13] R. F. Egerton, Physical Principles of Electron Microscopy: An Introduction to TEM, SEM, and AEM (Hardcover- April 25, 2008).
- [14] L. Reimer, P.W. Hawkes, Scanning Electron Microscopy: Physics of Image Formation and Microanalysis (Springer Series in Optical Sciences) (Hardcover- Oct 16, 1998).
- [15] B. G. Yacobi, D.B. Holt, Cathodoluminescence Microscopy of Inorganic Solids, 1990, New York
- [16] T. Yoshitake, T. Hara, K. Nagayama, Diamond and Related Materials **12** (2003) 306.

## Chapter 3

---

- [17] M. N. R. Ashfold, F. Claeysens, G. M. Fuge, Simon J. Henley, *Journal of Chemical Society Reviews* **33** (2004)23.
- [18] <http://www.doitpoms.ac.uk/tlplib/xray-diffraction/printall.php> (accessed 23.08.2013).
- [19] <http://www.phosphor-technology.com/products/crt.htm> (accessed 22. 08. 2013).

# Chapter 4

## Surface state of $\text{Y}_3(\text{Al}, \text{Ga})_5\text{O}_{12}:\text{Tb}$ phosphor powder under electron beam bombardment

### 4.1 Introduction

A broad range of applications of luminescent materials in display technologies such as television screens and fluorescent lamps have attracted attention and have encouraged researchers to improve and investigate the fundamental properties of these materials. Amongst the various aspects that need more attention are luminous efficiency and lifetime of the phosphors used in flat panel screens. Significantly improved performance of displays demands high quality phosphors with sufficient brightness and long term stability. Many researchers are using rare-earths doped oxides as opposed to sulfides to prepare thermally and chemically stable phosphors that can be used in various display applications such as field emission displays (FEDs) [1], plasma display panels (PDPs) [2], cathode ray tubes (CRT) [3]. Phosphors play a key role in the performances of these devices, their quantum efficiency and stability over time need to be investigated and improved. Sulfide-based phosphors represent one class of phosphors, but there are several problems associated with them [4 – 6]. When they are irradiated with an electron beam, they may decompose and generate gases, such as  $\text{SO}_2$  [7] and  $\text{H}_2\text{S}$  that are detrimental to emitter tips of FEDs. Several rare earth-doped oxide materials have been studied as possible FED phosphors [8]. Amongst these luminescent materials, Yttrium Aluminum Garnet, with the chemical formula of  $\text{Y}_3\text{Al}_5\text{O}_{12}$  and usually abbreviated as YAG, doped with rare-earth elements shows great luminescent properties [9 – 11]. In particular, YAG:Tb is one of the promising phosphor candidates that may be used in above-mentioned and other applications [11] and has been studied extensively due to its well-known

green emission [12]. Furthermore, YAG is a host with excellent structural compatibility. Inner  $Y^{3+}$  and  $Al^{3+}$  can to a certain extent be substituted by many kinds of cations with different sizes and valency. Many researchers investigated the effect of doping other ions into the host structure [13]. As reported in [14 – 16], the brightness and the saturation characteristics of YAG were improved by the replacement of a portion of Al with Ga. On the other hand, this partial replacement with Ga slightly increases the degradation of the luminescence efficiency due to electron irradiation as reported by Katsutoshi et al. [14]. It was shown by Swart et al. and Holloway et al. [4 – 7] that by using CL spectroscopy, AE spectroscopy and XP spectroscopy during prolonged electron irradiation, electron stimulated surface chemical reactions (ESSCRs) occurred on the surface of several phosphors, which led to the formation of non-luminescent layers. In this study, the changes on the surface state and luminous efficiency of  $Y_3(Al, Ga)_5O_{12}:Tb$  during electron irradiation were monitored by using a combination of techniques including scanning electron microscopy (SEM), XRD, PL, CL, AES and XPS.

## 4.2 Experimental

Commercially available  $Y_3(Al, Ga)_5O_{12}:Tb$  phosphor powders, obtained from Phosphor Technology with CIE coordinates: ( $x = 0.355, y = 0.557$ ) and non-uniform particles with median particle size of  $4 \mu m$  were used in this study [17]. The phosphor powder was characterized by XRD for their phase purity and crystallinity. XRD analysis was carried out using a Bruker AXS D8 ADVANCE X-ray diffractometer, with a  $CuK_{\alpha 1}$  ( $1.5406 \text{ \AA}$ ) in the  $2\theta$  range from  $15^\circ - 90^\circ$ , with a counting time of 1 s for each step size of  $0.0189^\circ$ . The PL properties of the phosphors were measured using a Carry eclipse spectrophotometer at room temperature using a monochromatized Xenon flash lamp as an excited source. The morphology and chemical composition analyses were carried out using a PHI

700 nano scanning Auger electron microprobe (NanoSAM) and a PHI, model 545, Auger electron spectroscope (AES), respectively. The degradation Auger data were collected in a vacuum chamber using the PHI, model 545, AES unit. An Ocean Optics PC2000 Spectrometer and OOI Base32 computer software were used to record the CL data from the powder sample. The Auger and CL data were recorded simultaneously using the same electron beam. The phosphor has been subjected to an electron beam current density of  $38.1\text{mA}\cdot\text{cm}^{-2}$  with a working beam voltage of 2 keV and a beam size spot of  $10\ \mu\text{m}$ . The electron beam irradiation was prolonged for more than 27 h at a background pressure of  $2.3 \times 10^{-8}$  Torr and an  $\text{O}_2$  pressure of  $2.3 \times 10^{-2}$  Torr. The XPS measurements were carried out with a PHI 5000 Versaprobe-Scanning ESCA Microprobe. The surveys were done with a  $100\ \mu\text{m}$ , 25 W, 15 kV beam using monochromatic Al  $K_\alpha$  radiation ( $h\nu = 1486.6\ \text{eV}$ ). For higher resolution spectra the hemispherical analyzer pass energy was maintained at 11.8 eV (C1s, Al2p, O1s, Tb3d, Y3d and Ga2p) for 50 cycles. Measurements were performed using either a 1 eV/step and 45 min. acquisition times (binding energies ranging from 0-1400 eV) for survey scans or a 0.1 eV/step and 20-30 min. Measurements were made before and after a prolonged electron bombardment. The pressure during acquisition was typically lower than  $1.0 \times 10^{-7}$  Torr. MULTIPAK software [18] was used for the deconvolution of the peaks.

## 4.3 Result and discussion

### 4.3.1 Structural and morphology analysis

The XRD pattern of the  $\text{Y}_3(\text{Al}, \text{Ga})_5\text{O}_{12}:\text{Tb}$  phosphor plus the profile of the ICSD data file are shown in Figure (4.1). The pattern is in agreement with the cubic (Ia-3d(230)) phase [19, 21] of the  $\text{Y}_3(\text{Al}, \text{Ga})_5\text{O}_{12}:\text{Tb}$  phosphor and is identical to the referenced ICSD data file No.029250 [19], with the main peak



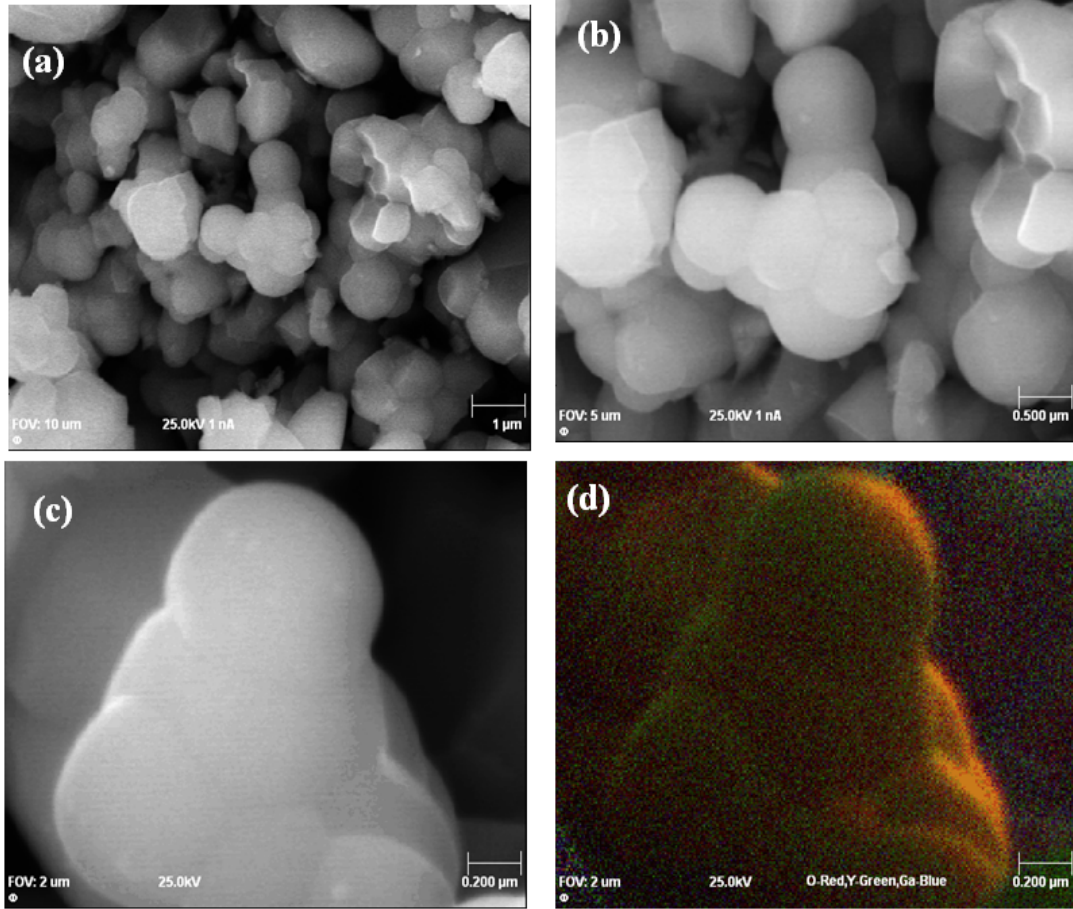


**Figure 4.2:** SEM photograph of  $Y_3(Al, Ga)_5O_{12}:Tb$  phosphor with 25 kV beam energy, different field of view of (a)  $10\mu m$  , (b)  $5\mu m$  (c)  $2\mu m$  and (d)  $2\mu m$  with color.

ions surrounded by  $O^{2-}$  ions in the dodecahedral arrangement, whilst both  $Al^{3+}$  and  $Ga^{3+}$  are surrounded by  $O^{2-}$  ions in a tetrahedral and octahedral arrangement. Eight oxygen ions are nearest neighbors of Y or Tb which belongs to two different groups:  $(Al_1Ga_1)_6^{9-}$  and  $(Al_1Ga_1)_4^{5-}$  [21] as shown in Figure 4.4.

### 4.3.2 PL and CL results

Mayolet et al. [21] studied the  $4f^75d$  configuration in  $Y_3(Al_x, Ga_y)_5O_{12}:Tb$  and they concluded that there are five excitation band energies ( $E_1, E_2, E_3, E_4$  and  $E_5$ )

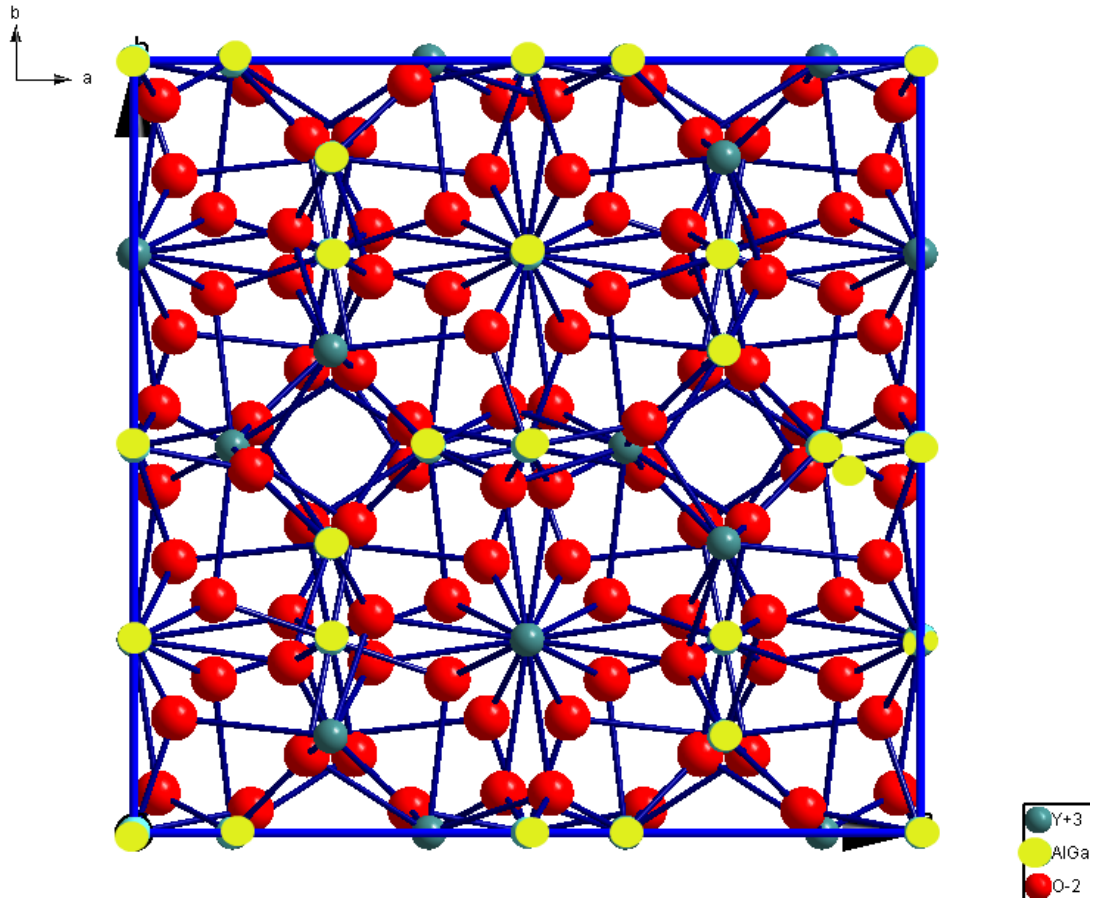


Figure 4.3:  $\text{Y}_3(\text{Al}, \text{Ga})_5\text{O}_{12}:\text{Tb}$  unit cell (ICSD-29248).

which clearly depend strongly on different concentrations of Ga. The energy level changes for different concentrations of Ga, as redrawn from Ref. [21], are presented in Figure 4.5. Their results may be summarized as follows:

1. For a high Al composition: the  $E_1, E_2, E_3$  and  $E_4$ , excitation bands, correspond to the excitation of the  $4f^7 5d$  states of  $\text{Tb}^{3+}$  whereas,  $E_5$  is hidden by the inter-band transition  $E_g$  in the host.
2. For a high Ga composition:  $E_1, E_2, E_{3,4}$  ( $E_3, E_4$  collapse) and  $E_5$  (shoulder) correspond to the excitation of a  $4f^8 4f^7 \rightarrow 5d$  transition of  $\text{Tb}^{3+}$  ions.

If the peak positions, as determined from the excitation spectra, are known for the different excitation bands, it may be used to estimate the relative Ga:Al

concentration of the  $Y_3(Al, Ga)_5O_{12}:Tb$  phosphor. Figure 4.6 shows the PL excitation and emission spectra of  $Tb^{3+}$  in the  $Y_3(Al, Ga)_5O_{12}:Tb$  phosphor. The excitation spectrum was measured at an emission wavelength of 544 nm and the emission spectrum was measured at an excitation wavelength of 267 nm. The excitation spectrum consists of three ultraviolet (UV) bands which are assigned to  $E_1$ ,  $E_2$  and  $E_3$  (316, 267 and 227 nm respectively) excitation bands, respectively.  $E_2$  was used as the excitation wavelength of the PL emission spectrum. The determined energy values of the excitation bands are plotted in Figure 4.5. The Ga to Al is estimated to be 7:13 (35% Ga : 65% Al). The  $Tb^{3+}$  ion ( $4f^8$ ) can be raised to the  $4f^75d$  configuration if excited by UV radiation to feed the  $^5D_3$  or/and  $^5D_4$  ground configuration multiplets [21]. The last relaxation step occurs through emission of the visible radiation. In the  $Y_3(Al, Ga)_5O_{12}:Tb$  phosphor, the main PL emission peak was due to the  $^5D_4 \rightarrow ^5F_5$  transition of  $Tb^{3+}$  and was measured at a wavelength of 544 nm with minor peaks at 489 nm ( $^5D_4 \rightarrow ^5F_6$ ), 590 nm ( $^5D_4 \rightarrow ^5F_4$ ) and 625 nm ( $^5D_4 \rightarrow ^5F_3$ ) [11, 22]. Figure 4.7 shows the CL emission spectrum of the  $Y_3(Al, Ga)_5O_{12}:Tb$  phosphor, excited with a 2 keV electron beam, before and after electron irradiation ( $3000\text{ C/cm}^{-2}$ ) at an oxygen pressure of  $1.0 \times 10^{-6}$  Torr. The CL emission spectra are similar to those of the PL with a main peak at 544 nm, suggesting that the electron beam did not change the electron energy level configuration or transitions of the activator ion in the phosphor. A slight increase in the CL intensity was obtained after prolonged electron irradiation. A relative increase of about 8% and 10% in the CL measured with respect to the starting CL intensity were  $10^{-8}$  and  $10^{-6}$  Torr samples, respectively, see also CL changes in Figures 4.9 and 4.10.

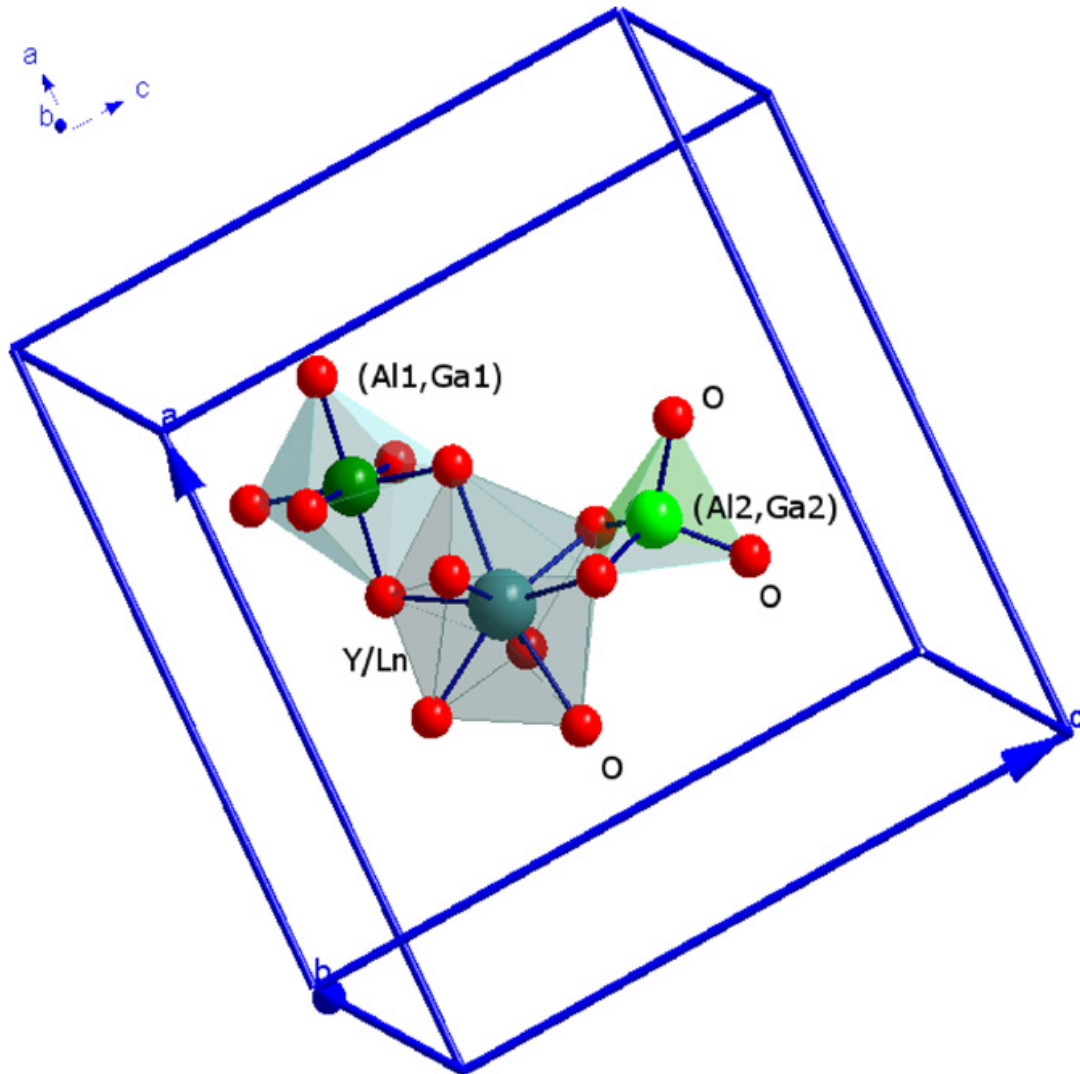


**Figure 4.4:** The arrangement of Y, O, Al and Ga described with polyhedral in  $Y_3(Al, Ga)_5O_{12}:Tb$  (ICSD-29248).

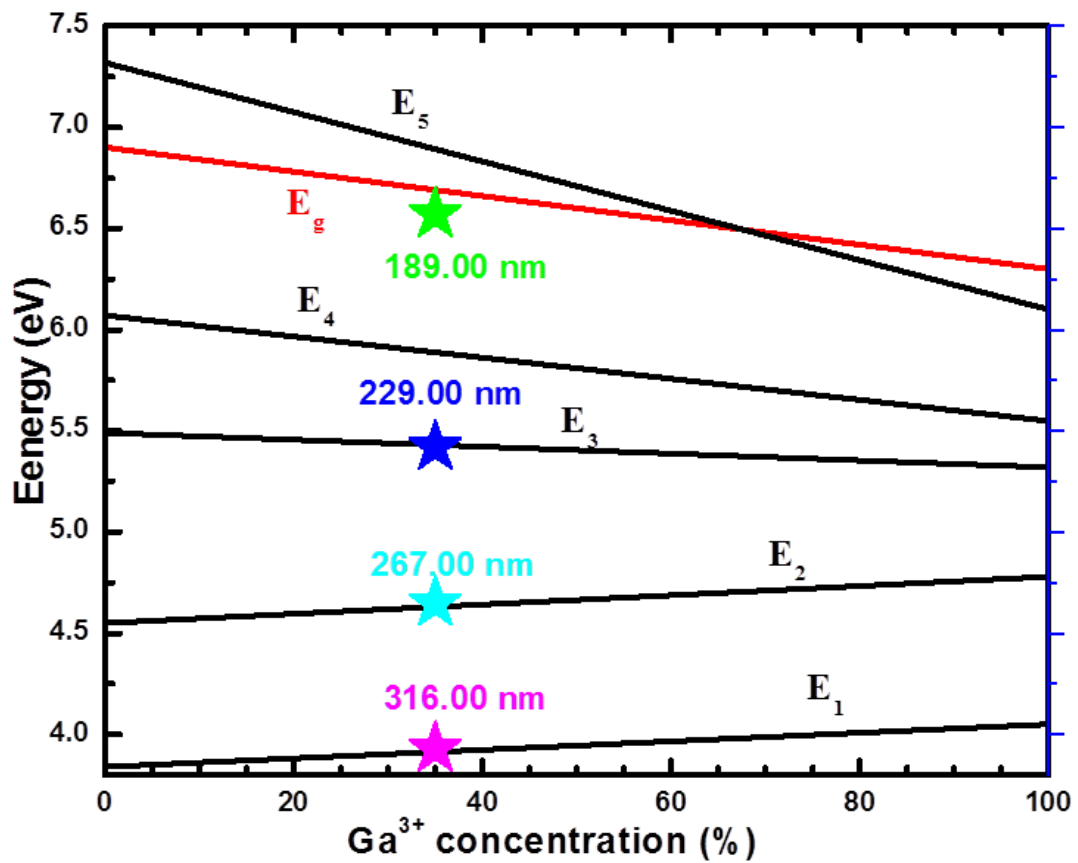


**Figure 4.5:** Excitation bands energies versus the gallium ion concentration in the garnet host.

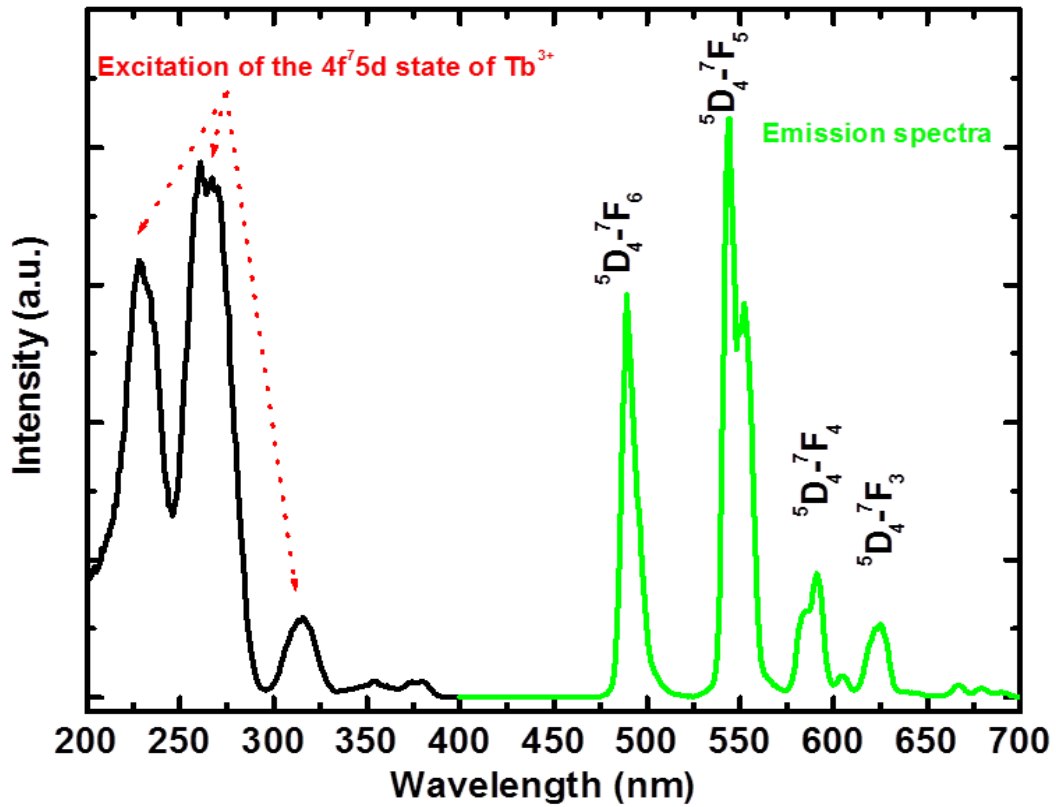


**Figure 4.6:** PL emission and excitation of Y<sub>3</sub>(Al, Ga)<sub>5</sub>O<sub>12</sub>:Tb (Excitation measured at an emission wavelength of 544 nm; emission measured at an excitation wavelength of 267 nm).

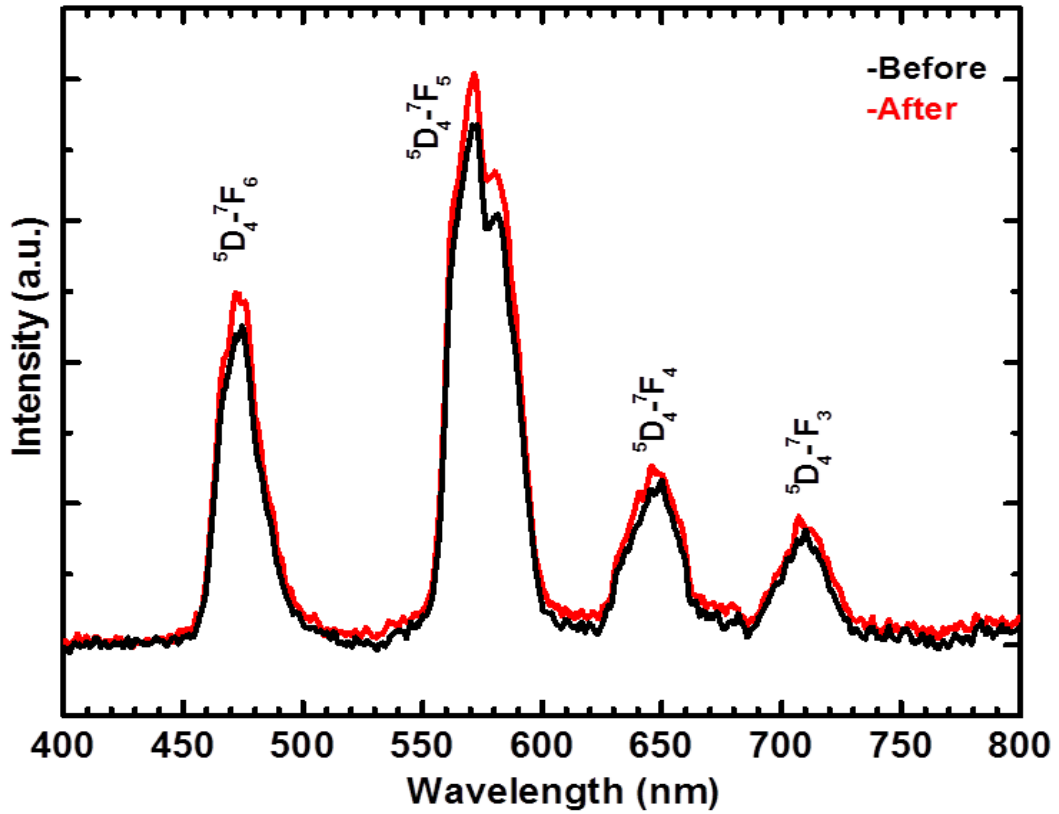


**Figure 4.7:** The CL spectra of  $\text{Y}_3(\text{Al, Ga})_5\text{O}_{12}:\text{Tb}$  phosphor, before and after electron beam bombardment in an oxygen ambient pressure of  $1.0 \times 10^{-6}$  Torr. (Excitation measured at an emission wavelength of 544 nm; emission measured at an excitation wavelength of 267 nm).

### 4.3.3 AES and APPHs analysis

The Auger spectra of the  $Y_3(Al, Ga)_5O_{12}:Tb$  phosphor, before and after electron beam irradiation at an oxygen pressure of  $1 \times 10^{-6}$  Torr are presented in Figure 4.8. Overlapping of Al, Y and Tb Auger peaks was monitored in the 59 to 160 eV energy range, O and Ga were at 510 eV and 1070 eV respectively [23]. All were related to the phosphor; in addition C, Cl, N and Cu elements were also detected. The C, Cl and N were attributed to adventitious impurity species on the surface due to handling and exposure to atmospheric pressure. The Cu was measured from the Cu sample holder. It is clear that after electron exposure, the Al, Y and O Auger peaks intensity have changed and the impurity species were almost completely removed from the surface, indicating that a new surface structure has been formed during prolonged electron irradiation. Figures 4.9 and 4.10 shows the individual Auger peak to peak heights (APPHs) and CL intensity measured at 544 nm as function of electron dose, monitored at the base pressure of  $2.3 \times 10^{-8}$  Torr. It is clear that the CL intensity and O APPH slightly increased during the removal of C and N. An initial increase in the CL intensity followed by the stabilization in CL were also observed up to an electron dose of  $3000 \text{ C/cm}^2$  at an oxygen pressure of  $1 \times 10^{-6}$  Torr, Figure 4.10. This behavior was probably due to the electron irradiation of the surface of the sample in these specific ambient conditions, which caused changes in the surface chemistry of the sample. The adventitious C and N desorbed from the surface as a result of the electron beam exposure. Furthermore, C was removed from the surface at a much higher rate in the oxygen ambient, compared with the results obtained at the base pressure of  $2.3 \times 10^{-8}$  Torr as shown in Figures 4.9 and 4.10. The reduction in the C peak intensity can be interpreted by using the postulated mechanism of the electron stimulated surface chemical reactions (ESSCRs) on the phosphor surface as demonstrated by Swart et al. [24] and Sebastian et al. [25]. In the ESSCRs process, the electron beam dissociate the

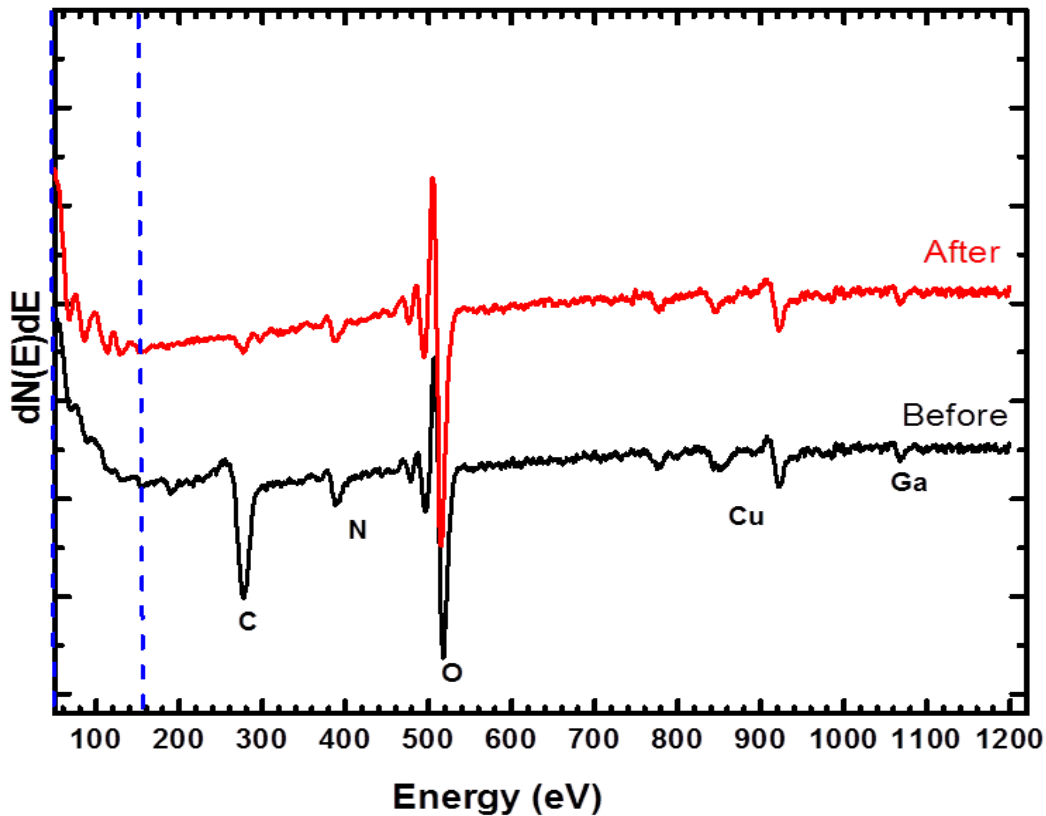


**Figure 4.8:** Auger spectra before and after electron beam bombardment at a base pressure of  $2.3 \times 10^{-8}$  Torr.

$O_2$  and other residual gases adsorbed on the surface from molecular species to atomic/ionic species [24 – 27], the water vapor dissociated as  $H_2O \rightarrow 2H^+ O^-$ , which subsequently react with C to form volatile compounds ( $CO_x$ ,  $CH_4$ , etc.). The removal of Cl and N from the phosphors surface may also be explained by similar reactions. It is clear, taking Figure 4.8 also into account, that it was not only C and N that were removed from the surface but other chemical changes were also taking place during prolonged electron irradiation. Normally a non luminescent surface layer formed during prolonged electron irradiation which lead to a decrease in CL intensity [6, 7, 24, 25].

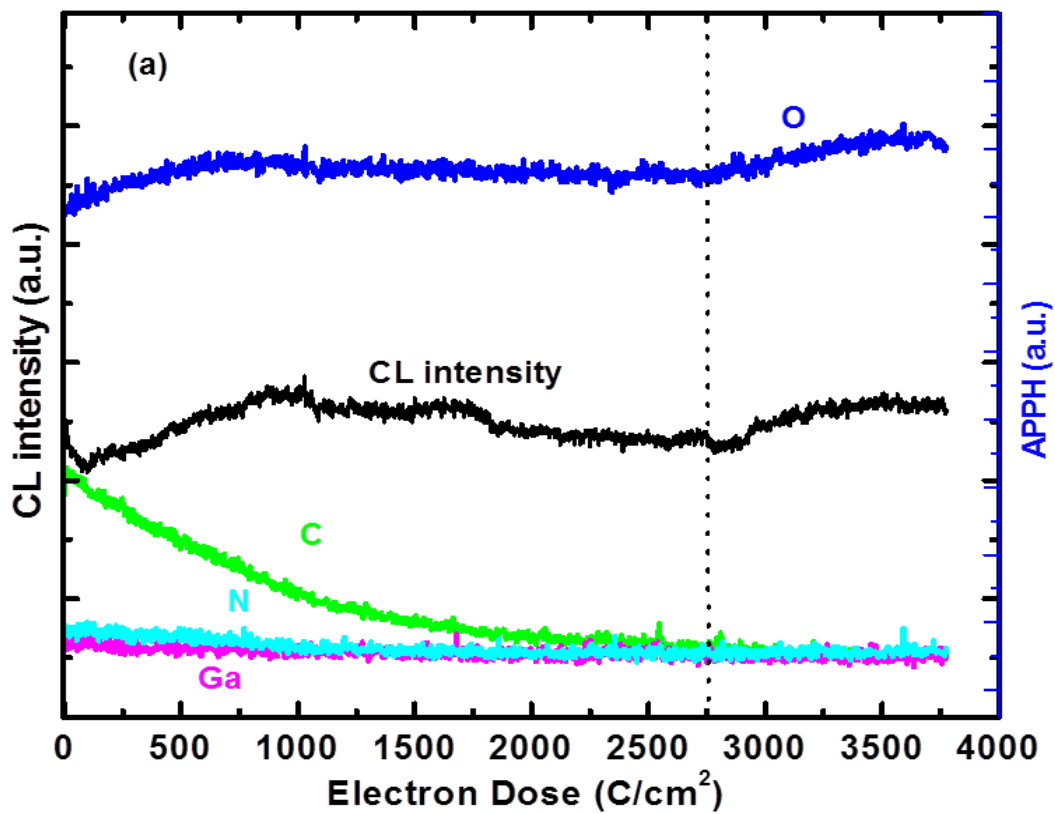


**Figure 4.9:** CL intensity and APPH (right scale) as a function of electron beam exposure for the  $\text{Y}_3(\text{Al, Ga})_5\text{O}_{12}:\text{Tb}$  phosphor at the base pressure of  $2.3 \times 10^{-8}$  Torr.

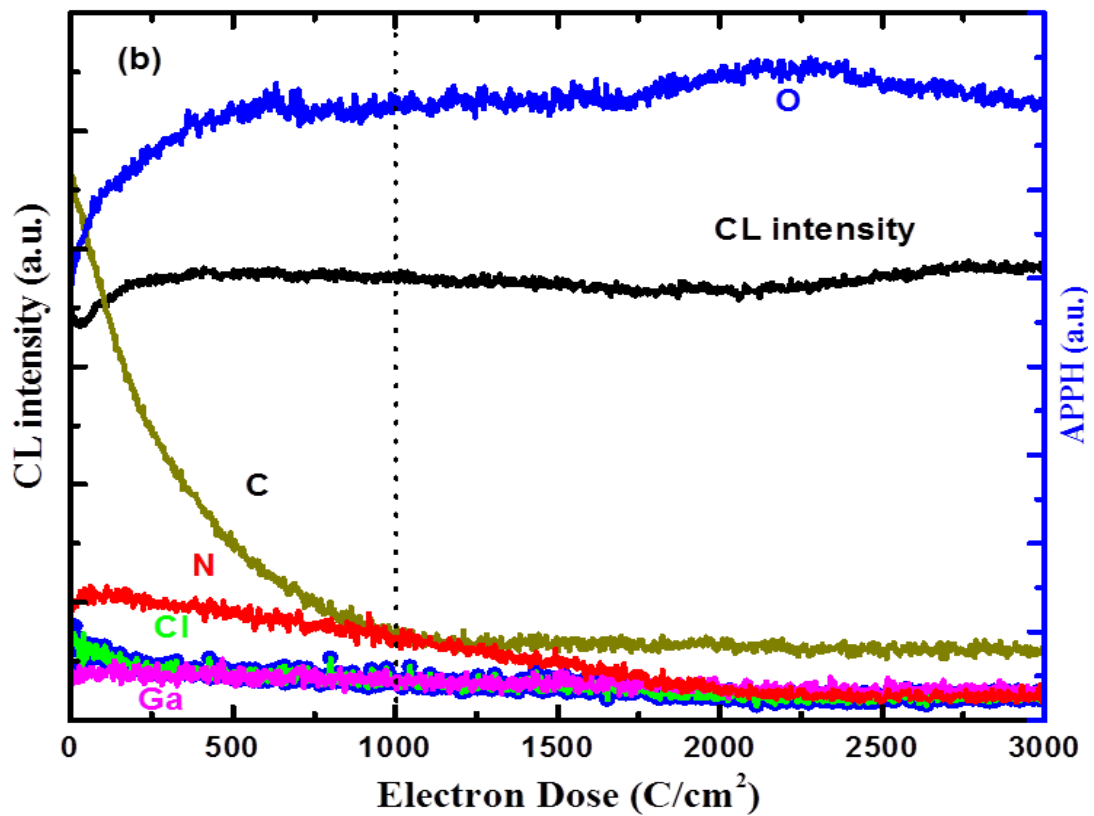


**Figure 4.10:** CL intensity and APPH (right scale) as a function of electron beam exposure for the  $Y_3(Al, Ga)_5O_{12}:Tb$  phosphor at an oxygen pressure of  $1.0 \times 10^{-6}$  Torr.

A decrease in the secondary electron emission (not shown) was also observed before and after electron irradiation, in this case, indicating that the work function of the material also has changed due to the new species that have formed on the surface, leaving more energetic electrons in the phosphor material to excite the material with a consequent increase in the CL emission. It is possible that a tradeoff between the non luminescent layer and the change in work function lead to a stable CL intensity in this case. Small changes in CL due to charging of the surface and change in work function were also previously measured by Nagpure et al. [28].

### 4.3.4 XPS results

An XPS study was carried out on the  $Y_3(Al, Ga)_5O_{12}:Tb$  phosphor before and after electron beam exposure ( $0-3000\text{ C/cm}^2$ ) to confirm the surface chemical changes on the phosphor surface during prolonged electron irradiation. The high resolution scans of O 1s, Al 2p, Y 3d, Ga 2p3 and Tb 3d peaks are presented in Figure 4.11 before and after electron irradiation. The XPS deconvoluted fits were done while keeping the structure of the  $Y_3(Al, Ga)_5O_{12}$  presented in Figure 4.3 and 4.4 in mind. The binding energies, prior to and after electron beam exposure of the deconvoluted peaks of the  $Y_3(Al, Ga)_5O_{12}$  system are listed in tables 7.5, 4.2, 4.3, 4.4 and 4.5.

Figures 4.11((a), (b), (c) and (d)) present O (1s), Al (2p), Y (3d) and Ga (2p) XPS peaks for the  $Y_3(Al, Ga)_5O_{12}$  systems prior to electron beam exposure, respectively. The O (1s) is deconvoluted into three peaks, due to two oxygen sites in the octahedral and the tetrahedral arrangement around Al/Ga and the other peak for the dodecahedral arrangement around Y/Tb in the  $Y_3(Al, Ga)_5O_{12}$  system (see Figures. 4.3 and 4.4). The Y (3d) peak, was split into two peaks Y (3d<sub>5/2</sub>) and Y (3d<sub>3/2</sub>) due to the spin orbit coupling (the interaction of the electron angular momentum due to its spin with its orbital angular momentum),

## Chapter 4

---

Table 4.1: Binding energies for Al (2p) XPS peaks in  $Y_3(Al, Ga)_5O_{12}:Tb$  before and after electron degradation.

Al (2p) Binding energies (BE) (eV)				
Undegraded	73.7 and 74.3	-	-	75.65
Possible component	Octahedral and tetrahedral arrangement in $Y_3(Al, Ga)_5O_{12}$ [32]			Chemisorbed species
Degraded peak	73.7 and 74.3	71.6, 71.47	72.95, 72.94 [30]	76.0
Possible component	Octahedral and tetrahedral arrangement in $Y_3(Al, Ga)_5O_{12}$ [32]	$AlO_x$ [32]	$Y(Al, Ga)O_3$	Chemisorbed species

Table 4.2: Binding energies for Y (3d) XPS peaks in  $Y_3(Al, Ga)_5O_{12}:Tb$  before and after electron degradation.

Y (3d) Binding energies (BE) (eV)			
Undegraded	157.6 and 7159.6	-	
Possible component	Y(3d5/2) and Y(3d3/2) (dodecahedral arrangement) in $Y_3(Al, Ga)_5O_{12}$ [28]		
Degraded peak	157.6 and 159.7	158.7 and 160.6	156.05 and 158.1
Possible component	Y(3d5/2) and Y(3d3/2) (dodecahedral arrangement) in $Y_3(Al, Ga)_5O_{12}$ [28]	Y(3d5/2) and Y(3d3/2) in $Y(Al, Ga)O_3$	Y(3d5/2) and Y(3d3/2) $YO_x$

## Chapter 4

Table 4.3: Binding energies for O (1s) XPS peaks in  $Y_3(Al, Ga)_5O_{12}:Tb$  before and after electron degradation.

O (1s) Binding energies (BE) (eV)				
Undegraded	529.95, 530.7 and 531.7	-	-	
Possible component	O in $Y_3(Al, Ga)_5O_{12}$			
Degraded peak	530.1, 530.8 and 531.9	530.3 and 531.6	531.9	529.2
Possible component	O (1s) in $Y_3(Al, Ga)_5O_{12}$	O(1s) in $Y(Al, Ga)O_3$	O (1s) in $AlO_x$	O (1s) in $YO_x$

Table 4.4: Binding energies for Ga (2p) XPS peaks in  $Y_3(Al, Ga)_5O_{12}:Tb$  before and after electron degradation.

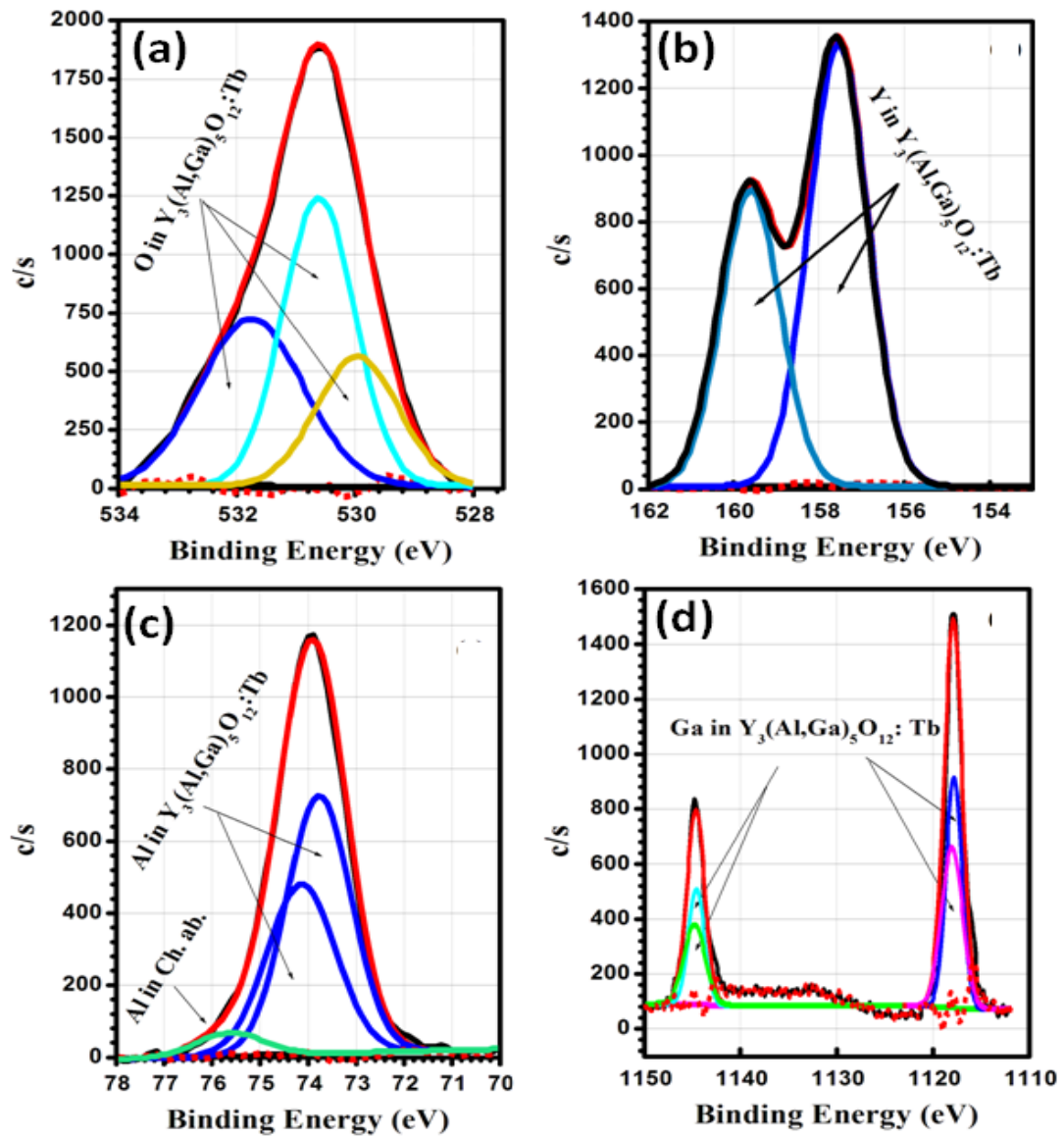
Ga (2p) Binding energies (BE) (eV)	
Undegraded	(1118.0 and 1118.2) and (1144.8 and 1145.0)
Possible component	Ga (2p <sub>3/2</sub> ) and Ga (2p <sub>1/2</sub> ) with Al in octahedral and tetrahedral arrangement in $Y_3(Al, Ga)_5O_{12}$
Degraded peak	(1118.0, 1116.2, 1116.90 [32]) and (1145.0, 1145.2, 1143.0)
Possible component	Ga (2p <sub>3/2</sub> ) and Ga (2p <sub>1/2</sub> ) with Al in octahedral and tetrahedral arrangement in $Y_3(Al, Ga)_5O_{12} + Y(Al, Ga)O_3$

Table 4.5: Binding energies for Tb (3d) XPS peaks in  $Y_3(Al, Ga)_5O_{12}:Tb$  before and after electron degradation.

Tb(3d) Binding energies (BE) (eV)	
Undegraded and degraded peaks	1276.2 and 1241.5

ascribe to the dodecahedral arrangement in the  $Y_3(Al, Ga)_5O_{12}$  systems. The Al (2p) is deconvoluted into three peaks; two of them represent octahedral and tetrahedral arrangement and the other is ascribed to chemisorbed species. The Ga (2p) deconvoluted into two peaks ascribed to Ga with Al in octahedral and tetrahedral arrangement in the  $Y_3(Al, Ga)_5O_{12}$  structure. The XPS peaks for the  $Y_3(Al, Ga)_5O_{12}$  systems after electron beam exposure, shown in Figures 4.11 ((e), (f), (g) and (h)), clearly indicated that new chemical species have formed during electron irradiation. A minimum of four additional peaks in O (1s) and two additional peaks in both Y (3d) and Al (2p) and one additional peak in Ga (2p) were needed to obtain the best fit for these XPS peaks. The four additional peaks in the O (1s) peak after electron irradiation maybe explained as representative of O (1s) in  $AlO_x$  with  $0 \leq x < 2$  (531.9 eV), two peaks for O (1s) in  $Y(Al, Ga)O_3$  (YAP) (530.3 eV and 531.6 eV) and the other for O (1s) in  $YO_x$  (529.2 eV). The extra fitted peaks in the Y (3d) peak are from the splitted 3d peaks of  $Y(Al, Ga)O_3$  (YAP) and  $YO_x$ . The two extra new peaks in the Al (2p) peak are from the Al (2p) in  $Y(Al, Ga)O_3$  (YAP) and the other from Al (2p) in  $AlO_x$  with  $0 \leq x < 2$ . The extra peak in Ga (2p) is ascribed to Ga with Al in  $Y(Al, Ga)O_3$ . No clear shifts were measured for the Tb (3d) peaks prior and after electron beam exposure. Hoque et al. [26] also found a peak at 72.2 eV which was attributed to  $AlO_x$  and two peaks at 71.2 and 71.7 eV due to the 2p<sub>3/2</sub> and 2p<sub>1/2</sub> metallic Al. Dhlamini et al. [27] have measured similar results on  $SiO_2$ . During prolonged electron irradiation  $SiO_2$  was dissociated into  $SiO_x$  with  $0 < x < 2$ . A similar trend with the dissociation of the  $Y(Al, Ga)O_3$  into species such as  $AlO_x$  and  $YO_x$  and then the formation of  $Y(Al, Ga)O_3$  and  $Al_2O_3$ . In summary the  $Y_3(Al, Ga)_5O_{12} : Tb$  systems is a complex oxide and therefore the reason for the complicated fit of all the XPS peaks. The different phases are situated in different chemical environments. Pawlak et al. [29] investigated pure single crystals and powdered samples of  $Y_3Al_5O_{12}$  (YAG) and YAG crystals doped with several rare earth elements and a transition metal. The variation in the XPS

peaks for all the main elements forming the garnet structure were observed due to different structural environments. No match between the binding energies exhibited by the simple  $\text{Y}_2\text{O}_3$  and  $\text{Al}_2\text{O}_3$  and complex  $\text{Y}_3\text{Al}_5\text{O}_{12}$  oxides was found. The reasons for these differences have been extensively studied in related materials, and some explanation were provided. The ionic state is defined as the case where there is a total transfer of electrons from an electropositive atom (e.g. Y) to an electronegative one (e.g. O) to produce units such as  $\text{M}^+ \text{O}^-$ , then it must be noted that no oxide system can totally achieve this state. Thus, to describe correctly the bonding of all oxides, some degree of covalency, albeit a relatively small one, must be included. This degree has been found to vary from oxide to oxide. They have also employed XPS to investigate  $\text{YAlO}_3$  doped with several rare earth elements and showed the variation of the peaks positions due to the different doped ions of varying oxidation states and they described it as a function of the structural environment and the oxidation state of the doping ions [30]. In our case XPS indicates that a possible explanation for the changing of the phosphors surface is that during the electron beam exposure of the  $\text{Y}_3(\text{Al}, \text{Ga})_5\text{O}_{12}:\text{Tb}$  phosphor surface chemical reactions occurred which separated the original phosphor into a  $\text{Y}(\text{Al}, \text{Ga})\text{O}_3$  structure and yttrium and aluminum oxide layers, a similar type of interleaved structure described in the literature as the Ruddlesden-Popper phases [31]. This interleaved structure may further complicate the binding energies of the electrons in the structure due to screening and charge density exchange between the different layers.



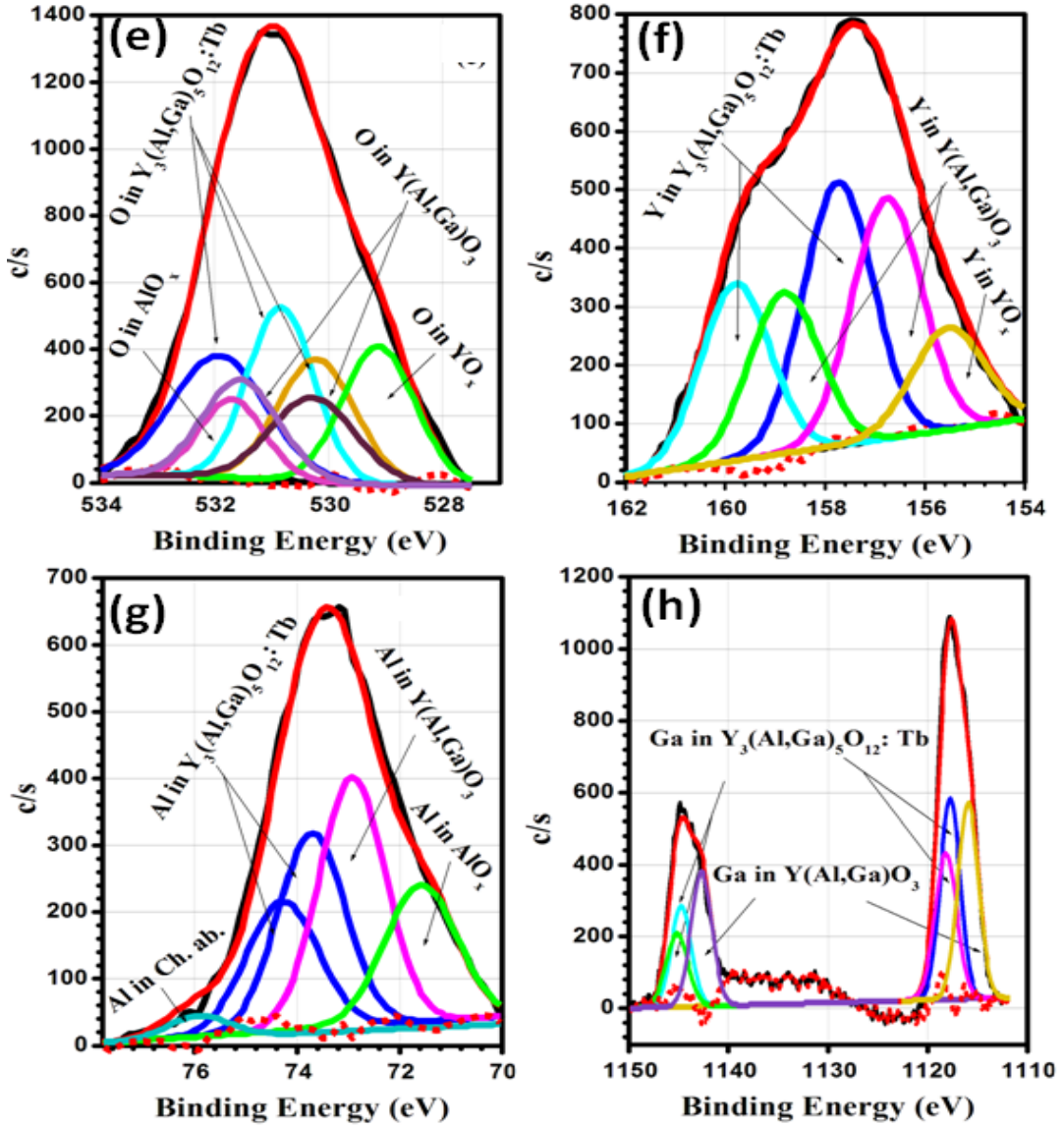


Figure 4.11: Deconvoluted O (1s), Y (3d), Al (2p) and Ga (2p) XPS peaks of  $Y_3(Al, Ga)_5O_{12}:Tb$  phosphor at the base pressure of  $2.3 \times 10^{-8}$  prior to [(a)(d) and (e)-(h)] and after electron beam exposure respectively

### 4.4 Conclusion

The surface state of  $Y_3(\text{Al}, \text{Ga})_5\text{O}_{12}:\text{Tb}$  phosphor was determined before and after more than 27 h of prolonged electron beam exposure at a base pressure of  $2.3 \times 10^{-8}$  Torr and an oxygen pressure of  $1.0 \times 10^{-6}$  Torr. Chemically adsorbed species such as C and N were removed from the surface by ESSCRs and new species were formed on the surface during prolonged electron irradiation. The CL intensity of the  $Y_3(\text{Al}, \text{Ga})_5\text{O}_{12}:\text{Tb}$  stabilized after removal of the chemisorbed species and stayed constant during further prolonged electron irradiation. A complicated surface structure formed in which chemical species such as  $Y(\text{Al}, \text{Ga})\text{O}_3$ ,  $\text{AlO}_x$  and  $\text{YO}_x$  were present. The layers acted as a protective layer for further degradation.

### References

- [1] M. H. Lee, S. G. Oh, S. C. Yi, D. S. Seo, J. S. Yoo, *Journal of the Electrochemical Society* **147** (2000) 3139.
- [2] G. C. Kim, S. I. Mho, H. L. Park, *Journal of Materials Science Letters* **14** (11) (1995) 805.
- [3] L. Ozawa, *Journal of Chemical Physics* **51** (1997) 107.
- [4] B. L. Abrams, P. H. Holloway, *Journal of Chemical Reviews* **104** (12) (2004) 5783.
- [5] V. Kumar, V. Mishra, M. M. Biggs, I. M. Nagpure, O. M. Ntwaeaborwa, J. J. Terblans, H. C. Swart, *Journal of Applied Surface Science* **256** (2010) 1720.
- [6] H. C. Swart, L. Oosthuizen, P. H. Holloway, G. L. P. Berning, *Surface and Interface Analysis* **26** (1998) 339.

- [7] H. C. Swart, J. J. Terblans, E. Coetsee, V. Kumar, O. M. Ntwaeaborwa, M. S. Dhlamini, J. J. Dolo, *Surface and Interface Analysis* **42 (6-7)** (2010) 922.
- [8] P. J. Marsh, J. Silver, A. Vecht, A. Newport, *Journal of Luminescence* **97** (2002) 229.
- [9] L. Zhang, X. Haiping, Q. Yang, W. Dongjie, J. Haochuan, *Journal of Rare Earths* **28** (2010) 236.
- [10] Z. Nan-Fei, L. Yong-Xiang, Y. Xiao-Feng, *Chinese Physics Letters* **25** (2008) 703.
- [11] H. H. Kwak, S. J. Kim, H. H. Yoon, S. J. Park, H. W. Choi, *Journal of Electroceramics* **23** (2009) 397.
- [12] J. Y. Choe, D. Ravichandran, S. M. Blomquist, K. W. Kirchner, E. W. Forsythe, D. C. Morton, *Journal of Luminescence* **93** (2001) 119.
- [13] Z. Mu, Y. Hu, H. Wu, C. Fu, F. Kang, *Journal of Alloys and Compounds* **509 (22)** (2011) 6476.
- [14] O. Katsutoshi, A. Tomohiko, K. Tsuneo, *Japanese Journal of Applied Physics* **29** (1990) 103.
- [15] H. Matsukiyo, H. Toyama, Y. Ueharab, H. Yamamotoc, *Journal of Luminescence* **229** (1997) 72.
- [16] Q. Li, F. Qiu, J. Zhang, X. Pu, X. Liu, W. Zhang, *Journal of Alloys and Compounds* **474** (2009) 441.
- [17] <http://www.phosphor-technology.com/products/crt.htm> (accessed 09.06.2011).

- [18] Multipak Version **9**, Physical Electronics, Inc., Chanhassen, USA, 2006-2010.
- [19] M. Marezio, J. P. Remeika, P. D. Dernier, *Acta Crystallographica* **24** (1968) 1670 (ICSD-29248).
- [20] K. Brandenburg, DIAMOND-2.0 Visual Crystal Structure Information System, Crystal Impact Distribution, Bonn, Germany, 1998.
- [21] A. Mayolet, W. Zhang, E. Simoni, J. C. Krupa, P. Martin, *Journal of Optical Materials* **4** (1995) 757.
- [22] J. Y. Choe, D. Ravichandran, S. M. Blomquist, D. C. Morton, K. W. Kirchner, M. H. Ervin, U. Lee, *Journal of Applied Physics Letters* **78** (2001) 24.
- [23] G. A. Hirata, O. A. Lopez, L. E. Shea, J. Y. Yi, T. Cheeks, J. McKittrick, J. Siqueiros, M. Avalos-Borja, A. Esparza, C. Falcony, *Journal of Vacuum Science and Technology A* **14** (1996) 1694.
- [24] H. C. Swart, J. S. Sebastian, T. A. Trottier, S. L. Jones, P. H. Holloway, *Journal of Vacuum Science and Technology A* **14** (**3**) (1996) 1697.
- [25] J. S. Sebastian, H. C. Swart, T. A. Trottier, S. L. Jones, P. H. Holloway, *Journal of Vacuum Science and Technology A* **15** (1997) 2349.
- [26] E. Hoque, J. A. DeRose, P. Hoffmann, B. Bhushan, H. J. Mathieu, *Journal of Physical Chemistry C* **111** (2007) 3956.
- [27] M. S. Dhlamini, J. J. Terblans, O. M. Ntwaeaborwa, H. C. Swart, *Surface Review and Letters* **14** (**4**) (2007) 697.
- [28] I. M. Nagpure, Shreyas S. Pitale, E. Coetsee, O. M. Ntwaeaborwa, J. J. Terblans, H. C. Swart, *Applied Surface Science* **257** (2011) 10147.

- [29] D. Pawlak, K. Wozniak, Z. Frukacz, T. Barr, D. Fiorentino, S. Seal, *Journal of Physical Chemistry B* **103** (1999) 1454.
- [30] D. Pawlak, K. Wozniak, Z. Frukacz, T. Barr, D. Fiorentino, S. Hardcastle, *Journal of Physical Chemistry B* **103** (1999) 3332.
- [31] S. N. Ruddlesden, P. Popper, *Acta Crystallographica* **11** (1958) 54.
- [32] NIST X-ray Photoelectron Spectroscopy Database, Version 3.5, <http://srdata.nist.gov/xps/> (accessed 21.11.2011).

# Chapter 5

## The influence of working atmosphere on $Y_3(\text{Al}, \text{Ga})_5\text{O}_{12}:\text{Tb}$ thin films grown with the PLD technique

### 5.1 Introduction

PLD is a widely used technique to grow thin films for a variety of applications. The major advantage of the PLD is the ability to transfer the material stoichiometrically from a multi-component ablation target to the growing film [1 - 3]. However, it is well known that such favourable results do not occur under all experimental conditions. Therefore different deposition parameters for each kind of material need to be optimized to get the films with the desired properties. Parameters that may play a role are target-substrate distance, different working atmosphere, substrate temperature, laser pulse energy density and pulse repetition rate [2, 4]. Compared to powders that are widely used in conventional displays, thin phosphor films have advantages such as superior thermal conductivity, a high degree of uniformity, a better thermal adhesion to the substrate. In addition, the uniform thickness combined with smoother surface morphology and smaller grain size makes it possible to obtain smaller pixel spot size for achieving higher resolution [5]. Yttrium aluminium garnet  $Y_3\text{Al}_5\text{O}_{12}$  material has been widely studied for different applications, by changing the dopants, the materials can be used to produce phosphors for a full-color display. It can withstand a high-energy electron beam and has been considered as an ideal candidate to prepare display phosphors [6, 7]. The brightness and the saturation characteristics of  $Y_3\text{Al}_5\text{O}_{12}:\text{Tb}$  were improved by substitution of a portion of Al with Ga resulting in a  $Y_3(\text{Al}, \text{Ga})_5\text{O}_{12}:\text{Tb}$  phosphor, that shows very good CL stability during prolonged electron bombardment, indicating that it is a promising phosphor candidate for field emission displays (FEDs) or other

light emitting devices [7]. Thin films of  $Y_3Al_5O_{12}:Tb$  phosphor have already been fabricated by the PLD technique and has been proposed for practical application [1] but there are no reports on  $Y_3(Al, Ga)_5O_{12}:Tb$  thin films fabricated by PLD. In this study all the deposition parameters were kept constant except the working atmosphere. The working atmospheres used were base pressure, oxygen, and argon and nitrogen pressures.

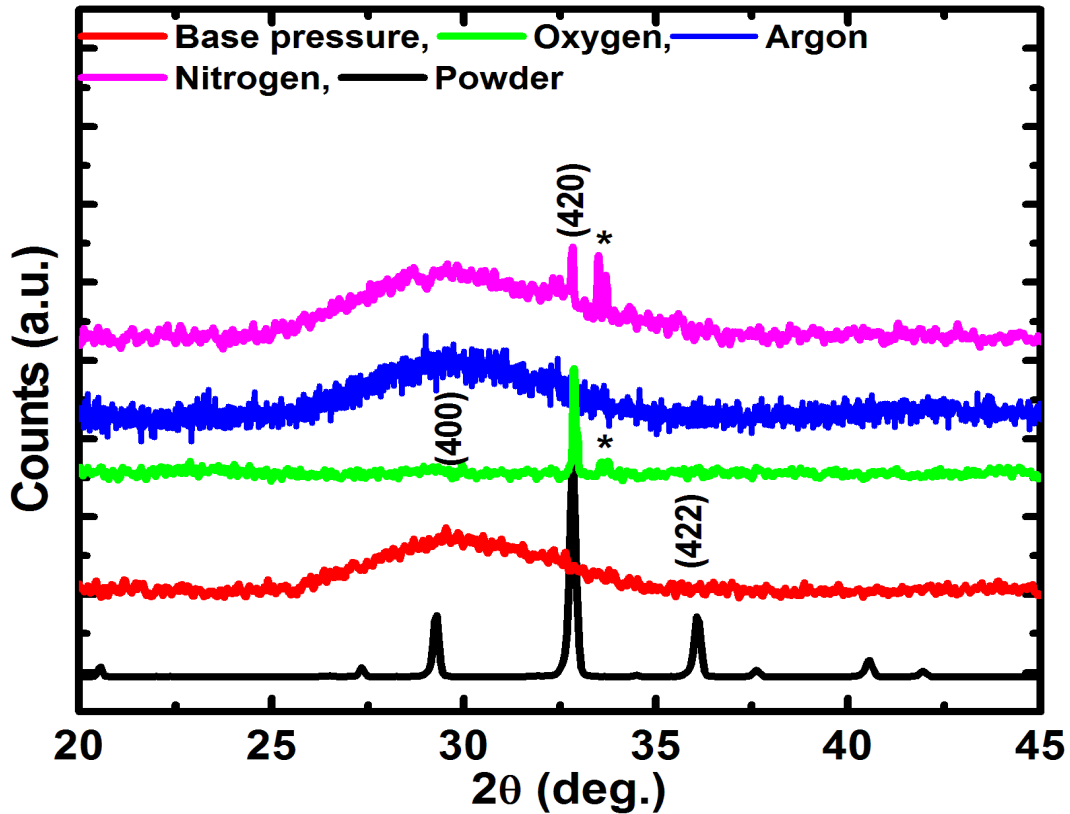
## 5.2 Experimental

Phosphor powder of  $Y_3(Al, Ga)_5O_{12}:Tb$ , obtained from Phosphor Technology [8] was directly pressed without binders into a homemade sample holder and was used as an ablation target. The target was annealed at 600 °C for 2 hrs in air and was then placed inside the PLD system on a rotating target holder. Si (100) wafers were ultrasonically cleaned sequentially in ethanol for 15 min, were transferred to an ultrasonic water bath and then dry blown with nitrogen ( $N_2$ ) gas. The films deposited in the different gas atmospheres were then deposited after the deposition chamber was evacuated to a base pressure of  $1.4 \times 10^{-6}$  mbar and then backfilled to a deposition pressure of  $2.7 \times 10^{-2}$  mbar for each gas ( $O_2$ ,  $N_2$  and Ar), except for the film deposited at the base pressure, where the chamber pressure was  $6.6 \times 10^{-6}$  mbar during the deposition process. A Nd:YAG 266 nm pulsed laser was used to ablate the phosphor pellet in the different working atmospheres. The laser frequency and fluence were 10 Hz and  $0.767 \text{ J/cm}^2$  respectively. The substrate temperature was fixed at 400 °C and the target to substrate distance was 6 cm. XRD analysis was carried out using a Bruker AXS D8ADVANCE diffractometer, using a  $Cu K_{\alpha 1}$  ( $1.5406 \text{ \AA}$ ) radiation in the  $2\theta$  range from  $15^\circ - 50^\circ$ , with a counting time of 1 s for each step size of  $0.015^\circ$ . The PL properties of the thin films were measured using a Carry eclipse spectrophotometer at room temperature using a monochromatized Xenon flash lamp as an excitation source. The surface morphology and roughness were ex-

amined by atomic force microscopy (AFM) with a Shimadzu SPM-9600 set in contact mode. The root mean square (RMS) roughness values were calculated from the height values from the AFM images using commercially available software. Chemical composition analyses and depth profiles were carried out using a PHI 700 nano scanning Auger electron microprobe (NanoSAM), surveys were done with 25 kV, 10 nA electron beam and a 2 kV Ar ion gun was used and the sputtering rate was 27 nm/min.

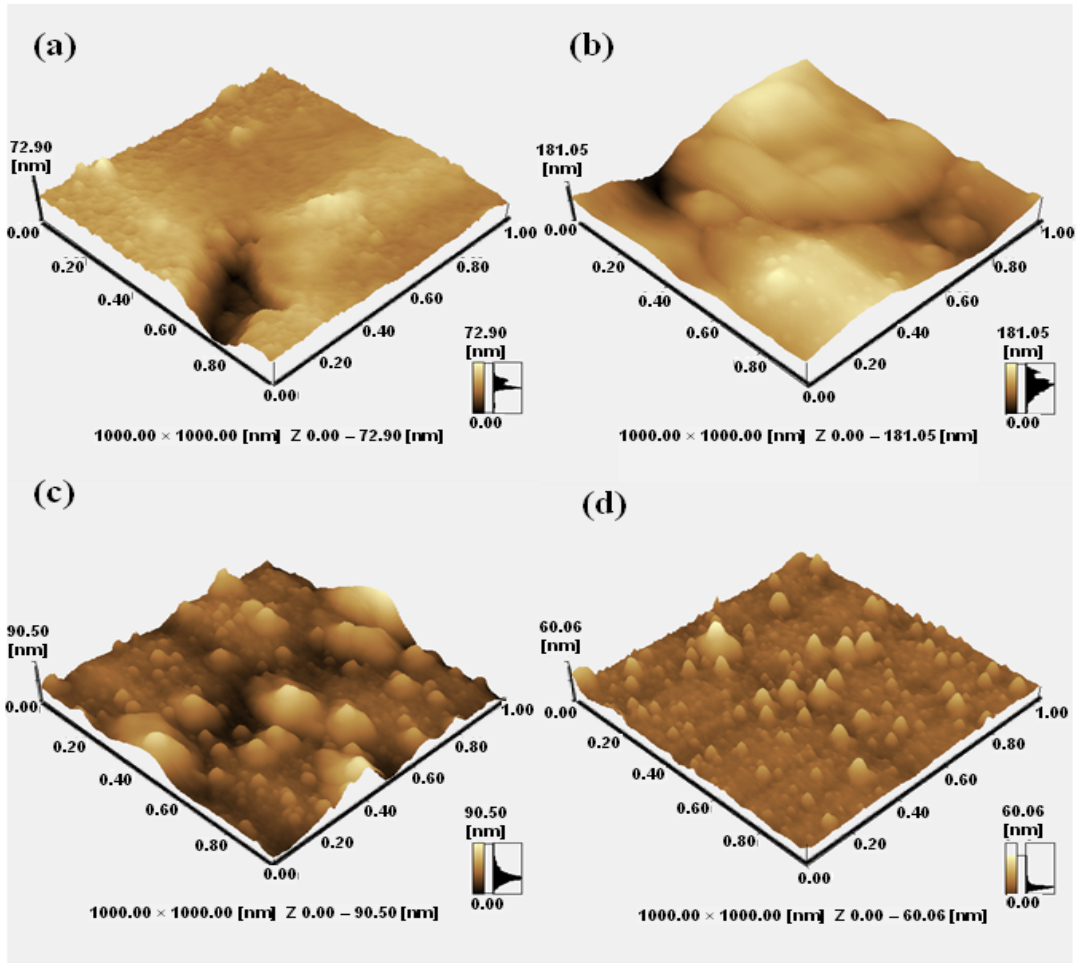
### 5.3 Results and discussion

Figure 5.1 shows the XRD patterns of  $Y_3(\text{Al}, \text{Ga})_5\text{O}_{12}:\text{Tb}$  powder and the films grown in the different working atmospheres. For the films prepared at base pressure and in Ar and  $\text{N}_2$  broad diffraction peaks located at  $2\theta = 29.55^\circ$  were observed, indicating that amorphous structures were formed during the deposition process. The XRD from the  $\text{O}_2$  atmosphere deposition shows only the (420) peak of  $Y_3(\text{Al}, \text{Ga})_5\text{O}_{12}$  [7] and peaks which are labelled with an asterisk (\*) can be associated with diffraction from the Si substrate. The deposition layer therefore has a (420) preferential orientation. The substrate peaks are not consistent but have been obtained in several other measurements in the past. The XRD of the Ar sample also has a (420) peak. Jiwei et al. [9], Jong-Ho Park et al. [11] and Naohiro et al. [12] reported that some peaks of the  $Y_2\text{O}_3:\text{Tb}$  cubic structure are in the range of these broad peaks. Figure 5.2 (a)-(d) shows three dimensional AFM images of the films. The film grown in base pressure in Figure 5.2 (a) shows undefined grain boundaries and a uniform surface with root mean square (RMS) roughness around 6 nm. The RMS was calculated without inserting the larger defect in the surface that can be seen in the figure. On the contrary, Figure 5.2 (b) presents the surface of the film grown in the  $\text{O}_2$  atmosphere, where large agglomerated grains with defined grain boundaries and roughness of about 30 nm were obtained. Figure 5.2 (c) exhibits the surface



**Figure 5.1:** XRD spectra of  $Y_3(Al, Ga)_5O_{12}:Tb$  phosphor powder and thin films grown in different working atmosphere.

topography of the Ar atmosphere thin film showing a smooth surface between spaced bigger grains with roughness of about 12 nm. The roughness of the  $N_2$  film shown in Figure 5.2 (d), is about 5 nm with a well defined grain distribution but it seems that the film was not continuous. It can be concluded that the surface roughness, grain shape and size were influenced by the deposition environment. The surface morphology of the films prepared in the different working atmosphere, can be seen from the SEM images in Figure 5.3(a)-(d). Figure 5.4 (1)-(7) show the AES spectra of (1) the  $Y_3(Al, Ga)_5O_{12}:Tb$  powder (2-4) the thin films that were grown in base pressure, (5)  $O_2$ , (6) Ar and (7)  $N_2$  pressure. The spectra were recorded at the indicated positions on the SEM images. Spherical particles appeared on the smooth surface of the  $Y_3(Al, Ga)_5O_{12}:Tb$



**Figure 5.2:** Three dimensional AFM images, for the thin film surfaces, grown in (a) base, (b)  $O_2$ , (c) Ar and (d)  $N_2$  atmosphere.

films. Some areas of the substrates surface were not completely covered with the thin film that was prepared in base pressure, Figure 5.3 (a). It can probably be referred to as the Volmer-Weber growth mode [13] where the energy due to the creation of interface is higher than the surface energy of the substrate and film. On the contrary, all the other substrate surfaces were covered with the deposited material for the films that were grown in (b)  $O_2$ , (c) Ar and (d)  $N_2$ . The AES spectra in Figure 5.4 confirm the presence of all the major elements, namely Yttrium (Y), Aluminium (Al), Gallium (Ga) and Oxygen (O) in the

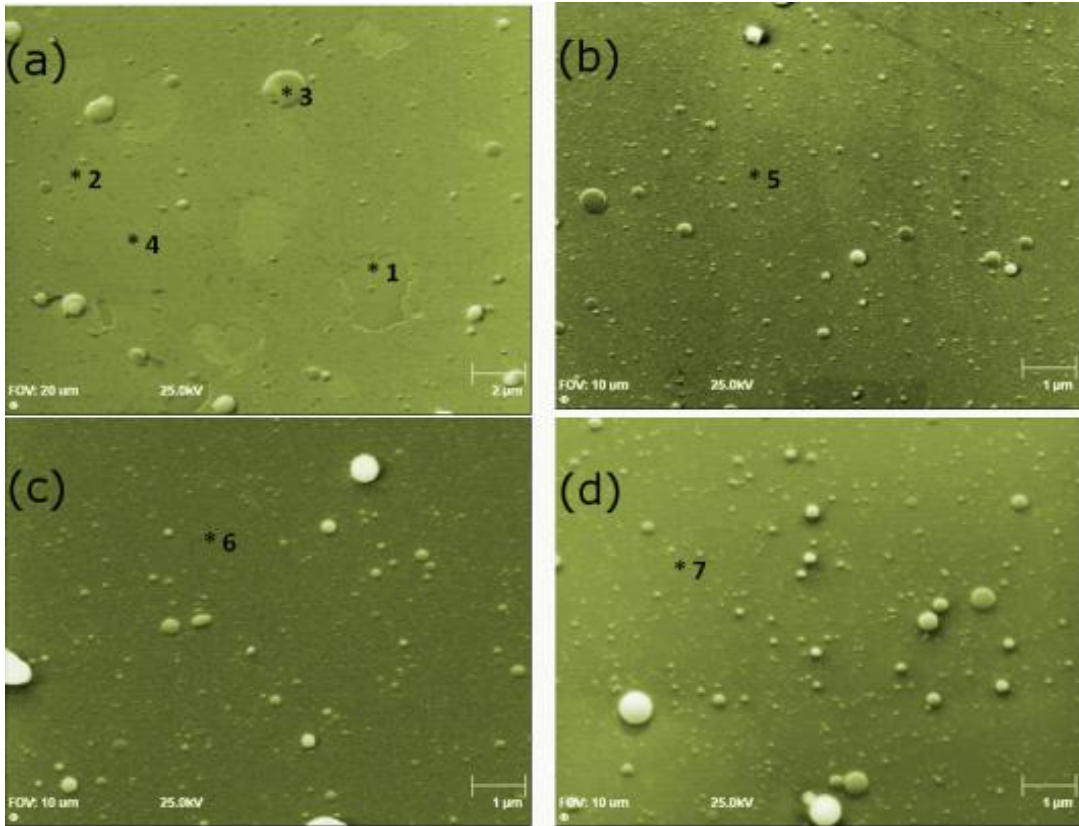


**Figure 5.3:** SEM images, for the thin film surfaces, grown in (a) base, (b)  $O_2$ , (c) Ar and (d)  $N_2$  atmosphere.

$Y_3(Al, Ga)_5O_{12}:Tb$  phosphor target and in the thin films [1, 7]. Figure 5.5 (a)-(d) show the compositional depth profiles of the thin film layers grown at (a) base pressure, (b) in  $O_2$ , (c) in Ar and (d) in  $N_2$ . The difference in atomic concentration, of films deposited in the different atmospheres, of each chemical element determined from the middle of the films is presented in table 5.3. The film grown in the  $O_2$  atmosphere is enriched in oxygen with respect to the films grown at the base, Ar and  $N_2$  atmospheres. It seems that during transport of the ablation material a depletion of some of the oxygen occurred. In the presence of the  $O_2$  atmosphere, however, some of these are replaced leading to a thin film stoichiometry that is most similar to the original phosphor as shown in Figure 5.6 and table 5.3. The thickness of the films were determined from the AES

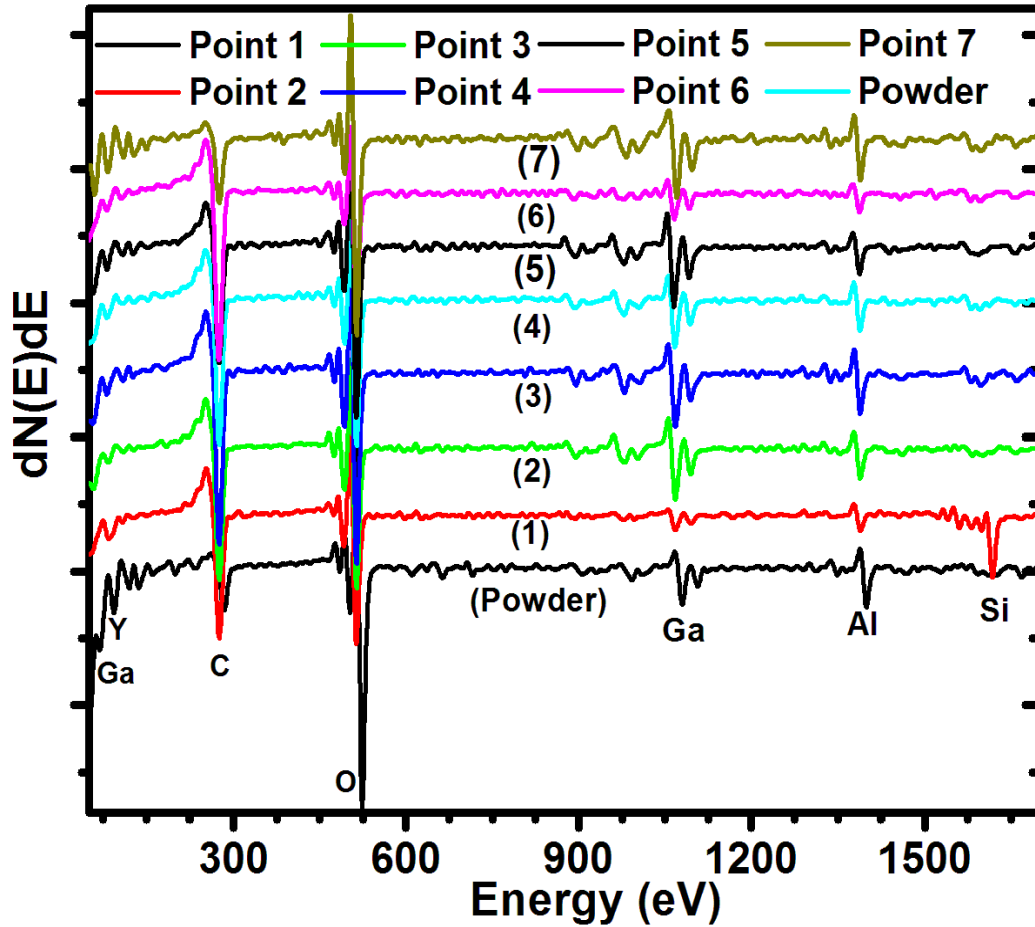


**Figure 5.4:** Different AES spectra of  $\text{Y}_3(\text{Al, Ga})_5\text{O}_{12}:\text{Tb}$  powder (1) and thin films grown in base pressure (2-4), (5)  $\text{O}_2$ , (6)  $\text{Ar}$  and (7)  $\text{N}_2$  atmospheres.

depth profiles to be approximately 55, 45, 40 and 30 nm for the films prepared in the base pressure,  $\text{O}_2$ ,  $\text{Ar}$  and  $\text{N}_2$  atmospheres respectively.

The PL emission characteristics for the thin films are illustrated in Figure 5.7. They all show typical emission spectra of  $\text{Tb}^{3+}$  ions due to the 5d-4f transitions from the excited  $^5\text{D}_4$  level to  $^7\text{F}_j$  ( $j=6-4$ ) levels of the ground state with the main peak at a wavelength of 544 nm ( $^5\text{D}_4 \rightarrow ^7\text{F}_5$ ) and minor peaks at 489 nm ( $^5\text{D}_4 \rightarrow ^7\text{F}_6$ ), 590 nm ( $^5\text{D}_4 \rightarrow ^7\text{F}_4$ ) and 625 nm ( $^5\text{D}_4 \rightarrow ^7\text{F}_3$ ) [7, 10]. The effect of different working atmosphere on the intensity can clearly be noticed in Figure

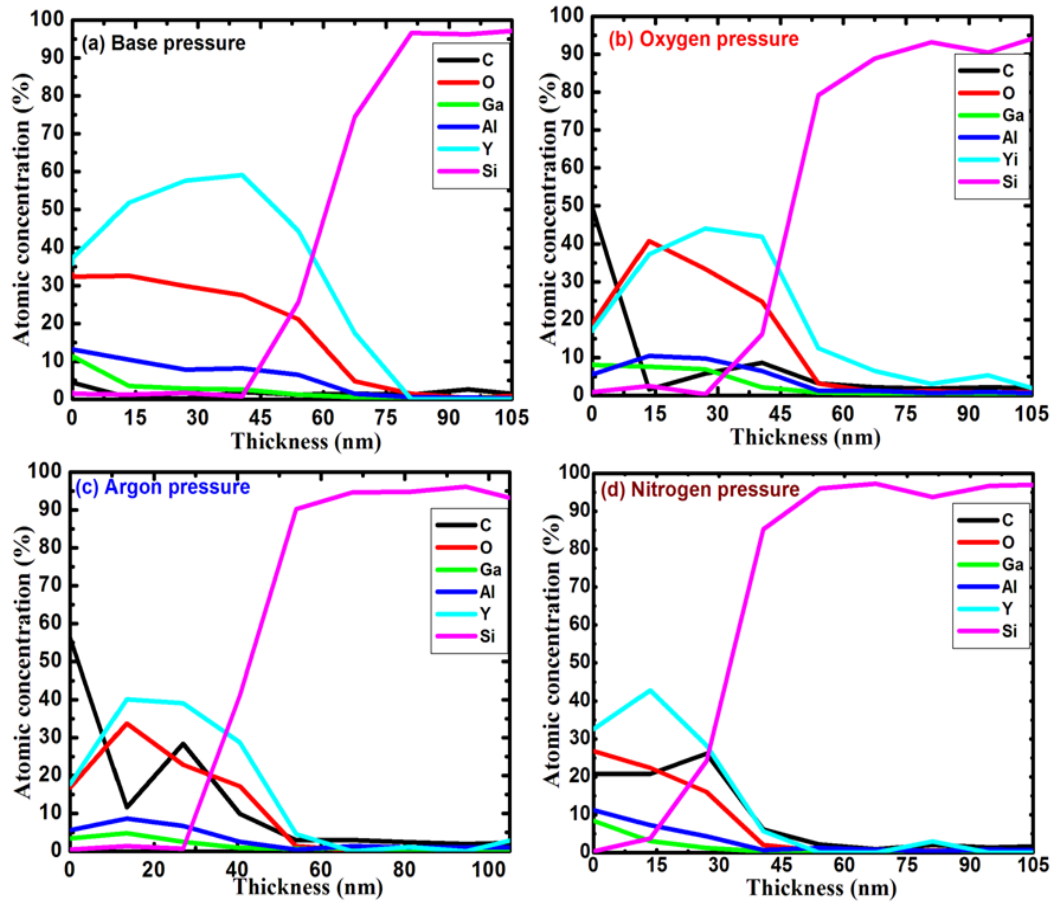


**Figure 5.5:** Depth profiles of the thin films structures, that were grown in (a) base, (b) O<sub>2</sub>, (c) Ar and (d) N<sub>2</sub> atmosphere.

5.7. The highest luminescent emission intensity was obtained from the thin film grown in the O<sub>2</sub> working atmosphere.

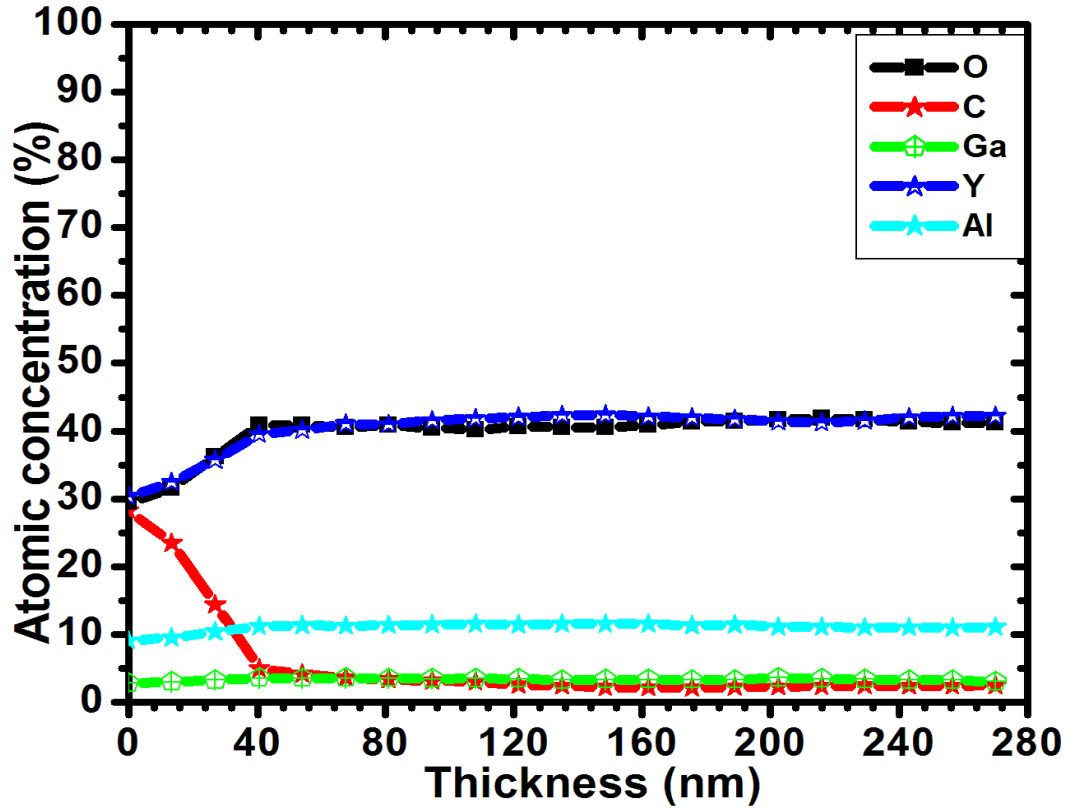
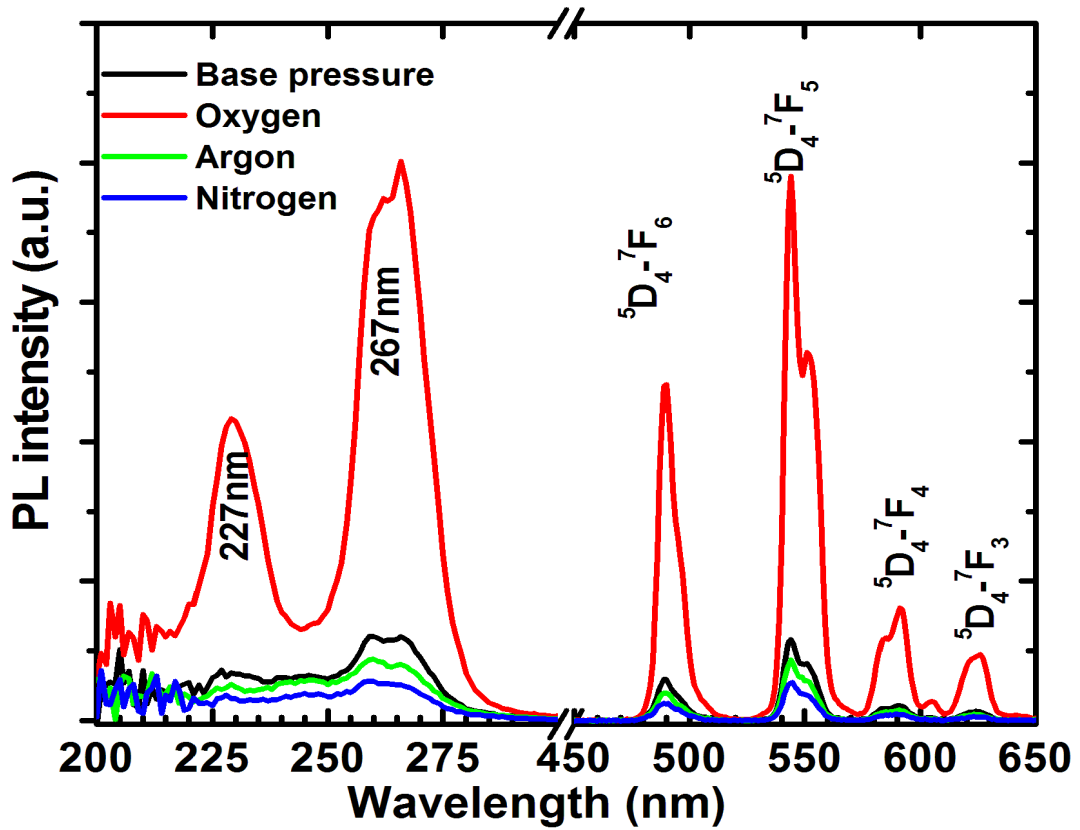


Figure 5.6: Depth profile of the phosphor powder.

Table 5.1: Atomic concentrations determined from the middle of the thin film layers deposited in the different working atmosphere

Working atmosphere	Atomic concentrations (%) at middle of the thin film layers					
	O	Y	Al	Ga	C	Si
Base pressure	30	57	8	3	0.2	1.5
Oxygen	37	40	10	7	4	1
Argon	28	40	7	4	20	1
Nitrogen	23	41	8	3	21	3
Powder	42	40	12	4	2	-



**Figure 5.7:** PL emission and excitation of  $Y_3(\text{Al}, \text{Ga})_5\text{O}_{12}:\text{Tb}$  thin films grown in different working atmosphere (Excitation measured at an emission wavelength of 544 nm; emission measured at an excitation wavelength of 267 nm).

## 5.4 Conclusion

Our results show that there is a clear correlation among the deposition atmosphere, structural properties of the thin films and their luminescent properties. The highest luminescent emission intensity was obtained from the film grown in the O<sub>2</sub> working atmosphere. Deposition in vacuum gives a smoother surface with roughness value around 6 nm and deposition in oxygen gave large agglomerated grains with defined grain boundaries and roughness of about ~30 nm.

## References

- [1] G. A. Hirata, O. A. Lopez, L. E. Shea, J. Y. Yi, T. Cheeks, J. McKittrick, J. Siqueiros, M. Avalos-Borja, A. Esparza, C. Falcony, *Journal of Vacuum Science and Technology A* **14** (1996) 1694.
- [2] M. S. HEGDE *Journal of Indian Academic Science* **113** (2001) 445.
- [3] C. B. Arnold, M. J. Aziz, *Journal of Applied Physics A* **69** (1999) S23.
- [4] T. Haugan, P. N. Barnes, L. Brunke, I. Maartense, J. Murphy, *Physica C* **397** (2003) 47.
- [5] P. Y. Jia, J. Lin, X. M. Han, M. Yu, *Journal of Thin Solid Films* **483** (2005) 122.
- [6] Y. C. Kanga, W. Lenggoroa I, S. B. Parkb, K. Okuyama, *Journal of Materials Research Bulletin* **35** (2000) 789.
- [7] A. Yousif, H. C. Swart, O. M. Ntwaeaborwa, *Applied Surface Science* **258** (2012) 6495.
- [8] <http://www.phosphor-technology.com/products/crt.htm> (accessed 24.04.2012).

- [9] J. Wang, H. Song, B. Sun, X. Ren, B. Chen, W. Xu, Journal of Chinese Physics Letters **379** (2003) 507.
- [10] G. Li, Q. Cao, Z. Li, Y. Huang, Y. Wei, J. Shi, Journal of Alloys and Compounds **485** (2009) 561.
- [11] J. Park , N. G. Back, M. Kwak, B. Jun, B. Choi, B. Moon, J. Jeong, S. Yi, J. Kim, Journal of Materials Science and Engineering C **27** (2007) 998.
- [12] N. Ishiwada, T. Ueda, T. Yokomori, Journal of Luminescence **26** (2011) 381.
- [13] E. John R, Pulsed Laser Deposition of Thin Films Applications-led Growth of Functional Material Wiley & Sons, (2007) Hoboken, New Jersey.

## Chapter 6

### Improved luminescence properties of pulsed laser deposited $Y_3(Al, Ga)_5O_{12}:Tb$ thin films by post deposition annealing

#### 6.1 Introduction

Luminescent films play an important role in high resolution display devices such as cathode-ray tubes (CRTs), electroluminescent devices, plasma display panels, and field emission displays (FEDs). Displays based on thin film phosphors are characterized by high contrast and resolution, good thermal conductivity as well as a high degree of uniformity and better adhesion [1 – 3]. Most phosphor materials consist of multi-components and their luminescence efficiency is largely affected by the right stoichiometry and crystallinity. One of the most important parameters in the deposition of a phosphor thin film is the stoichiometric materials transfer from the target material to the substrate. It is well known that the pulsed laser deposition (PLD) can produce a wide variety of complex compounds with controlled composition and properties [2].  $Y_3Al_5O_{12}$  has widely been used as a host lattice for lanthanide ions to produce phosphors emitting a variety of colors, especially in the green emission range [3, 6]. As reported by A.Yousif et. al. [5], the brightness and the saturation characteristics of  $Y_3Al_5O_{12}$  were improved by the replacement of a certain percentage of Al with Ga. On the other hand, this substitution slightly increases the degradation rate of the luminescence intensity during prolonged electron irradiation as reported by Katsutoshi et al. [7]. However,  $Y_3(Al, Ga)_5O_{12}:Tb$  phosphor powder, shows very good CL stability, during prolonged electron bombardment, indicating that, it is a promising candidate for FEDs and other lighting applications [5]. In this study, pulsed laser deposited  $Y_3(Al, Ga)_5O_{12}:Tb$  thin films were grown with fixed processing conditions (substrate temperature, target to

substrate distance, oxygen working atmosphere, etc.). Structural, PL and CL properties of the  $Y_3(Al, Ga)_5O_{12}:Tb$  thin films annealed at different temperatures are presented. The improvement of the luminescent properties that was attributed to improved crystallinity and stability of the films during electron beam irradiation was recorded.

## 6.2 Experimental

A commercial  $Y_3(Al, Ga)_5O_{12}:Tb$  powder phosphor, obtained from Phosphor Technology [8] was pressed without binders using an in-house built sample holder and was used as an ablation target. The target was annealed at 300 °C for 8 hrs in air to get rid of all adventitious water containing species that might be present in the pellet and was then placed inside the chamber of the PLD system on a rotating target holder that can also move linearly (up and down). Note that the rotational as well as linear motion of the target rod restricted the laser ablation induced degradation of the target surface. Si (100) wafers used as substrates were cleaned with ethanol for 15 min, in an ultrasonic water bath and then blown dry with nitrogen ( $N_2$ ) gas. The deposition chamber was evacuated to a base pressure of  $2.8 \times 10^{-5}$  mbar and then backfilled with  $O_2$  to a pressure of  $3.9 \times 10^{-2}$  mbar. The  $Y_3(Al, Ga)_5O_{12}:Tb$  target was ablated in the  $O_2$  working atmosphere using a 266 nm Nd:YAG pulsed laser. The laser frequency, number of pulses fluence, substrate temperature and target-to-substrate distance were fixed at 10 Hz, 10000, 0.767 J/cm<sup>2</sup>, 300 °C and 4.5 cm, respectively. The deposited thin films were annealed for 1 hour at 400 °C and 800 °C in air. X-ray diffraction (XRD) analysis was carried out using a Bruker AXS D8 ADVANCE X-ray diffractometer, with a Cu  $k_\alpha$  (1.5406 Å), with a counting time of 1 s for each step size of 0.0038 °. Photoluminescent (PL) properties of the films were measured with a Carry eclipse spectrophotometer and the films were excited at room temperature by using a mono-chromatized Xenon flash lamp. The surface

topography and roughness were examined from images captured in contact mode using Shimadzu SPM-9600 atomic force microscopy (AFM). The root mean square (RMS) roughnesses were estimated by analyzing the topography scans of the films surfaces using commercial software. The CL degradation data were collected using an Ocean Optics PC2000 spectrometer attached to the vacuum chamber of the PHI 545 Auger electron spectrometer and the data was recorded using OOI Base32 computer software. The chemical composition analyses and depth profiles were carried out using a PHI 700 nano scanning Auger electron microprobe (NanoSAM) and scanning electron microscopy (SEM), surveys were done with a 25 keV, 10 nA electron beam, a 2 kV Ar ion sputter gun was used and the sputtering rate was 27 nm/min. The samples were excited with an electron beam in the voltage range of 1-3 keV with a 10  $\mu$ A filament current while the CL intensities were monitored as a function of the accelerating voltage. For the CL intensity degradation study, the films were subjected to an electron beam of current density of 47.3 mA cm<sup>-2</sup>, with a working beam voltage of 2 keV and a beam current of 10  $\mu$ A.

## 6.3 Result and discussion

### 6.3.1 Structural and surface topography analysis

The XRD measurements were carried out on the as-deposited (as-prepared) and annealed films. From the XRD analysis, the as prepared film was amorphous. In Figure 6.1, the XRD pattern of the Y<sub>3</sub>(Al, Ga)<sub>5</sub>O<sub>12</sub>:Tb powder is also shown for comparison. The film started to crystallize when it was annealed at 400 °C with the preferential growth in the (420) direction. A clear diffraction pattern of the Y<sub>3</sub>(Al, Ga)<sub>5</sub>O<sub>12</sub> structure was observed for the films annealed at 800 °C. A secondary YAlO<sub>3</sub> impurity phase was also observed after annealing at this temperature. Interdiffusion of Si in the Y<sub>3</sub>(Al, Ga)<sub>5</sub>O<sub>12</sub> film matrix was reported

for annealing temperatures of 800 °C and above [9]. As reported by Y. Hu et al. [4], the amorphous films have many defects in their structure and are sometimes nonstoichiometric in composition. Due to the non-stoichiometric composition oxidation of the atoms can easily occur during post-deposition annealing and rearrange to form stable polycrystalline films. When annealing in air, the atoms can rearrange and the free oxygen in air may also react with the films. As a result, the structure can become more crystalline, as seen in the XRD peak intensities of the annealed films. Figure 6.2 present the AFM images of the

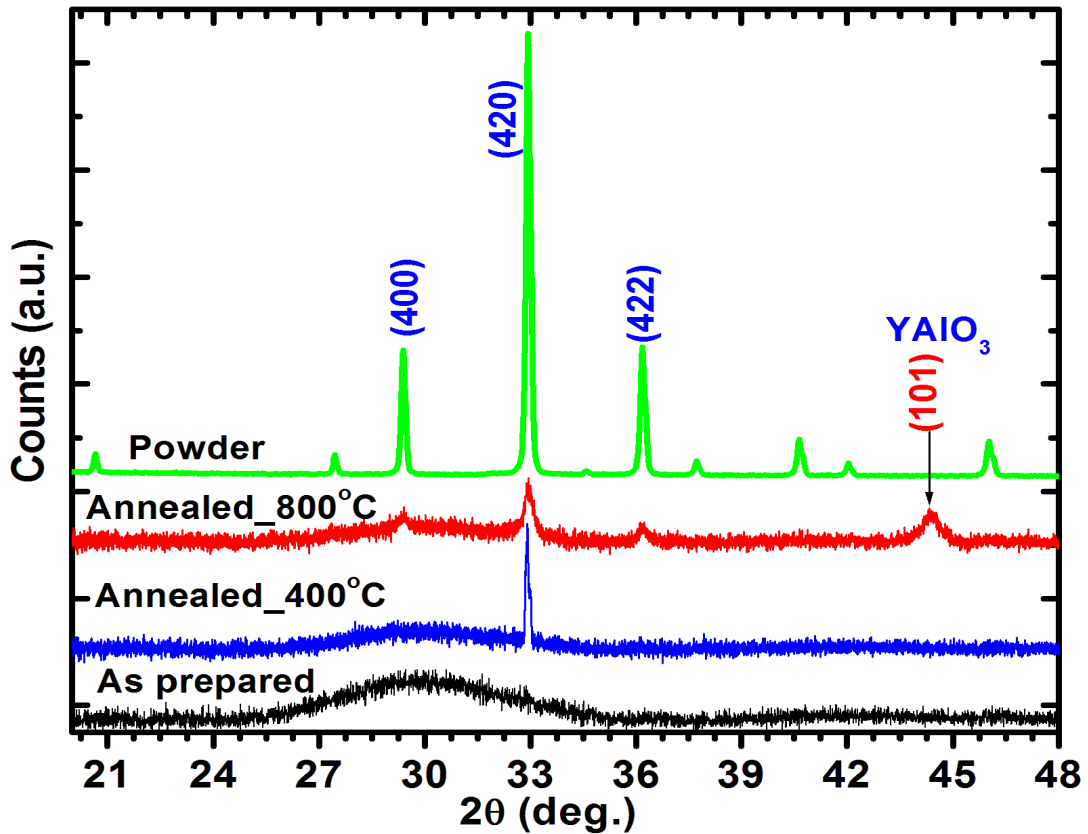


**Figure 6.1:** XRD spectra of  $Y_3(Al, Ga)_5O_{12}:Tb$  phosphor powder, deposited and annealed thin films.

three dimensional surface topography of the as deposited and annealed films. The deposited film shows well defined spherically grains that were uniformly distributed over the surface with root mean square (RMS) roughness of about

9 nm. Annealing at 800 °C induced changes in the surface topography, which show spherically grains covered with a smoother layer with root mean square (RMS) roughness of 6 nm. SEM images of the same surfaces (not same position) of the as-deposited and 800 °C films are shown in the first part of Figures 6.3 (a) and (b), respectively. The SEM images appeared to be smooth with micro- and nano-particulate features on the surfaces with places where it is clear that the thin film is not continuous in thickness. The smoother layer that is seen on

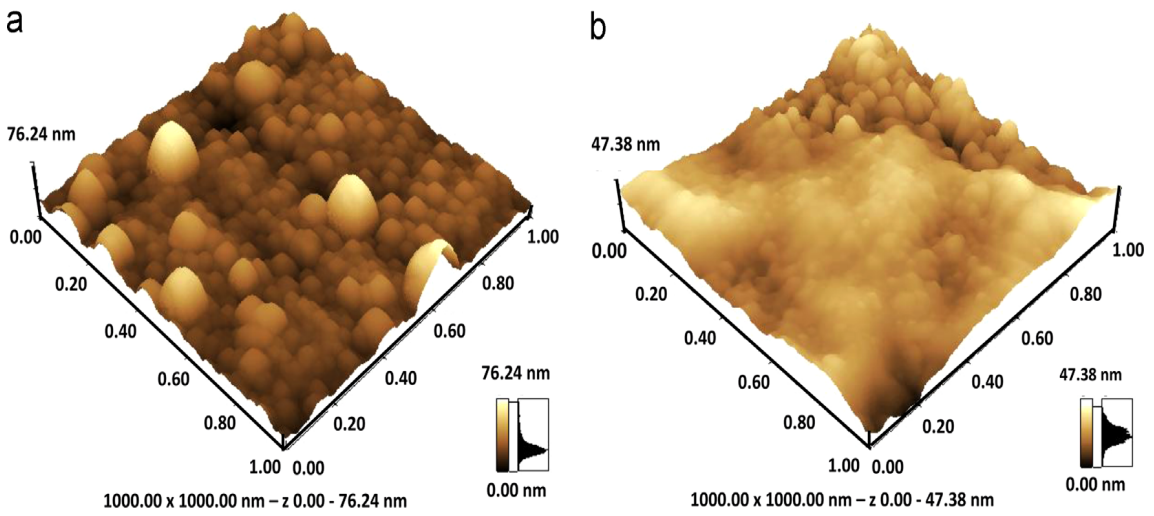


**Figure 6.2:** AFM images of the surface of (a) Y<sub>3</sub>(Al, Ga)<sub>5</sub>O<sub>12</sub>:Tb thin films as deposited and (b) after annealed at 800° C.

the AFM image of the 800 °C film is also clear on the SEM image (position A). Furthermore, the elemental distribution of Al (red), Ga (green) and Y (blue) are represented by the 2D NanoSAM elemental mapping captured with a 5 μm field of view in Figures 6.3 (a) and (b), for the as deposited and 800 °C annealed film, respectively. The elemental mapping of the deposited film shows a homogeneous distribution of the Al, Ga and Y elements, with an exception of some Y enriched rounded particles of different sizes which seem to be formed from local melting and ejected Y-O-Al from the target to the substrate which are typically found in laser ablation experiments [10]. The elemental mapping of the annealed film shows some inhomogeneous distribution of Ga on the surface

## Chapter 6

---

relative to the distribution of the deposited film, indicating that, some areas of the annealed film were enriched with Ga compared with the rest. According to our results (not published yet) the Ga concentration in  $Y_3(\text{Al}_{1-x}\text{Ga}_x)_5\text{O}_{12}:\text{Tb}$  has an influence on the PL intensity. The PL intensity increased with an increase in the Ga concentration up to an optimum amount and then decreased with a further increase in the Ga concentration. It can be concluded that annealing at  $800^\circ\text{C}$  caused diffusion of the Ga to some parts of the surface of the film, and might also have an effect on the PL intensity as pointed out.

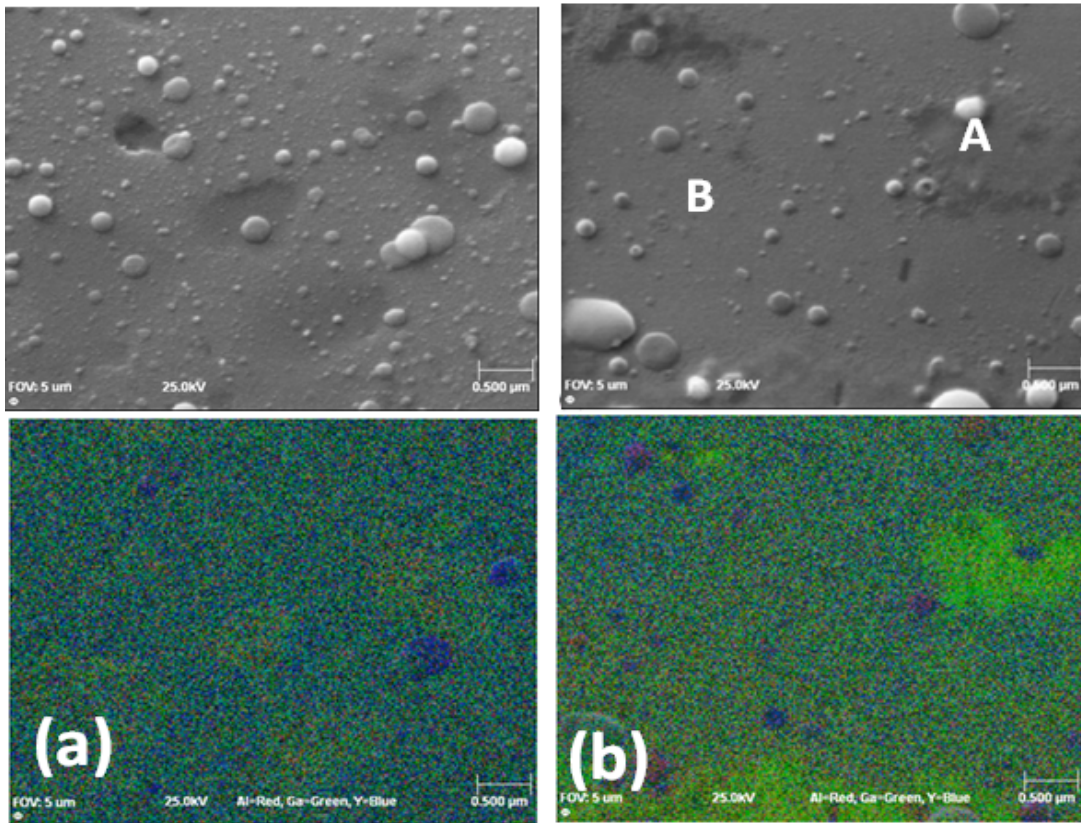


**Figure 6.3:** (a and b) NanoSEM and SAM images for deposited and annealed films at  $800^\circ\text{C}$ , of the combination of Al (red), Ga (green) and Y (blue) with  $5\mu\text{m}$  field of view.

### 6.3.2 Auger peak to peak heights (APPH) analysis

Figure 6.4, shows the measured AES depth profiles of the as deposited and annealed films. The depth profile of the annealed film was done at position B as indicated in the top part of Figure 6.3 (b). The sputtering was started at 0 minutes as indicated on the x-axes of the profiles. In the depth profiles, the main elements in the  $Y_3(\text{Al}_{1-X}, \text{Ga}_X)_5\text{O}_{12}:\text{Tb}$  material, i.e. Y, Al, Ga, O were found, indicating that, a compound of  $Y_3(\text{Al}_{1-X}, \text{Ga}_X)_5\text{O}_{12}:\text{Tb}$  film was formed as compared to a depth profile of the powder [9]. Additionally, there was also adventitious C on the surface. The thickness of the deposited film estimated from the specific depth profile was around 200 nm. Except for the broader interface, indicating some interdiffusion between the thin film and Si from the substrate there was no evidence of concentration changes due to annealing at 800° C. The film thickness in this case was estimated to be 120 nm. The thickness varied across the film layer as can be seen in Figures 6.2 and 6.3.

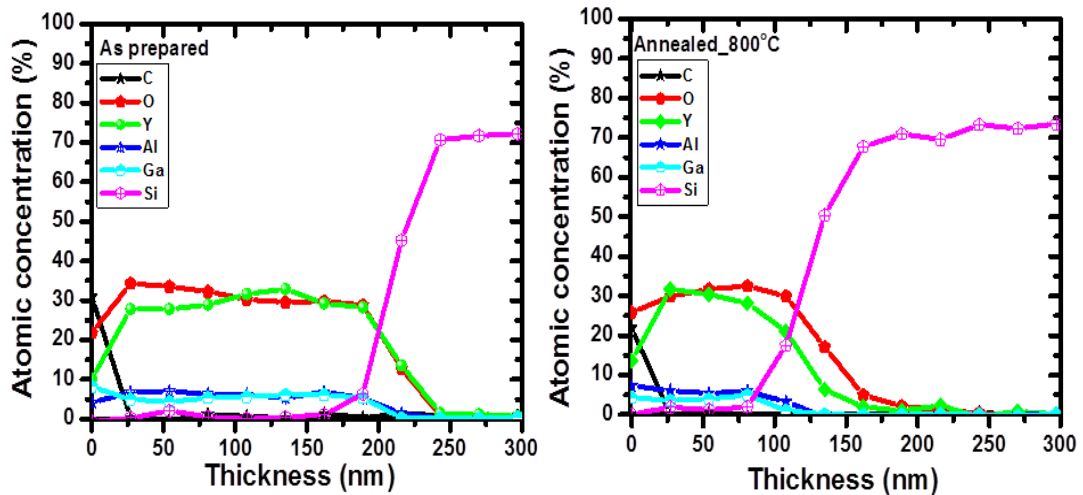


**Figure 6.4:** The AES depth profiles for the as deposited and 800° C annealed  $Y_3(\text{Al}, \text{Ga})_5\text{O}_{12}:\text{Tb}$  film.

### 6.3.3 2D NanoSAM Cross Section of annealed film

Elemental mapping of the cross sections of the annealed film, with the three colors: red, green and blue, represent O, Ga and Si, were performed in 2 and 1  $\mu\text{m}$  field of view, with 2D NanoSAM to determine the elemental distribution of O and Ga elements from the  $\text{Y}_3(\text{Al}, \text{Ga})_5\text{O}_{12}$  annealed films layer and Si in the substrate. The results showed a clear separation between the  $\text{Y}_3(\text{Al}, \text{Ga})_5\text{O}_{12}$  film and the Si substrate. Oxygen (red colour) was evenly distributed in the  $\text{Y}_3(\text{Al}, \text{Ga})_5\text{O}_{12}$  film as shown in Figures 6.5 (a) and (b). Although part of the image is showing the surface of the layer and not totally in focus of the electron beam, the Ga enrichment is clear in some parts on top of the thin film, as indicated by black oval shapes in Figures 6.5 (a) and (b). From Figure 6.5 (b) the variation in the thickness of the film is clear. The specific part of the thin film scanned in the 2 D image varied from about 100 nm as seen from the markers on the images up to for example 200 nm on the bottom of the 1  $\mu\text{m}$  field of view image (excluding the large rounded particle on the surface on the top part of the image). It is a well-known fact that films prepared by PLD differ in thickness [11, 12].

### 6.3.4 PL result

Figure 6.6 compares the PL spectra of the  $\text{Y}_3(\text{Al}, \text{Ga})_5\text{O}_{12}:\text{Tb}$  thin films as a function of the annealing temperature. The PL emission spectrum presented similar characteristics for all annealing temperatures which mean that the symmetry of emitting centers of the  $\text{Tb}^{3+}$  is quite similar. The emission lines are described by the well-known  ${}^5\text{D}_4 \rightarrow {}^7\text{F}_j$  ( $j=6, 5, 4, 3$ ) transitions of the  $\text{Tb}^{3+}$  ion [5, 10]. The main PL emission peak was due to the  ${}^5\text{D}_4 \rightarrow {}^7\text{F}_5$  transition of  $\text{Tb}^{3+}$  and was measured at a wavelength of 544 nm with minor peaks at 489 nm  ${}^5\text{D}_4 \rightarrow {}^7\text{F}_6$ , 591 nm  ${}^5\text{D}_4 \rightarrow {}^7\text{F}_4$  and 625 nm  ${}^5\text{D}_4 \rightarrow {}^7\text{F}_3$ . An enhancement of the PL intensities were observed as a function of annealing temperatures which

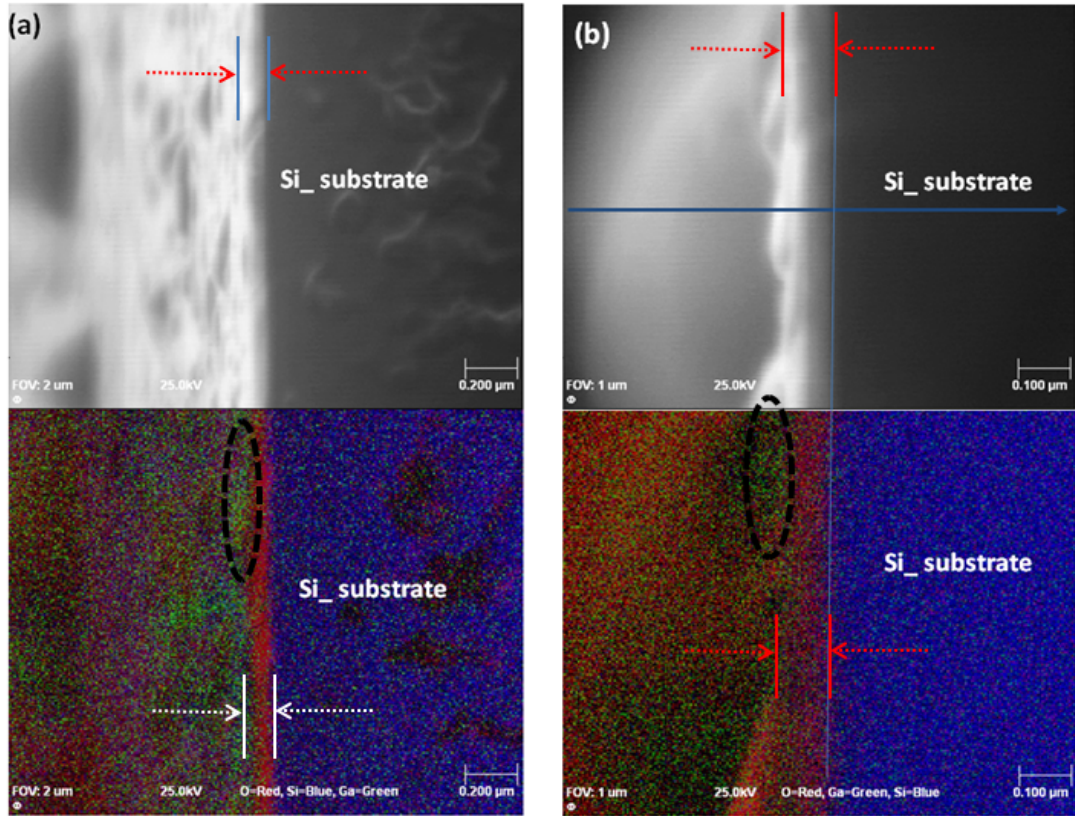


**Figure 6.5:** (a and b) Elemental mapping of the cross sections of the annealed film at 800 °C, with the three colors: red, green and blue, representing O, Ga and Si, in 2 and 1  $\mu\text{m}$  field of view, respectively.

was attributed to the improvement of the crystallinity of the films with an increase in the annealing temperature as presented in Figure 6.1 and a possible variation in Ga concentration as pointed out in the 2D NanoSAM maps. Figure 6.7 represents the chromaticity co-ordinates of the PL spectra for the deposited  $\text{Y}_3(\text{Al}, \text{Ga})_5\text{O}_{12}:\text{Tb}$  film, which were determined using the CIE Coordinate Calculator software [13]. The calculated chromaticity coordinates for the deposited film and the measured commercial phosphor powder are (0.32, 0.57) and (0.32, 0.56) compared to (0.355, 0.557) for the commercial phosphor powder given by the work company [8]. It can be concluded that, the deposited films almost have the same chromaticity coordinates.

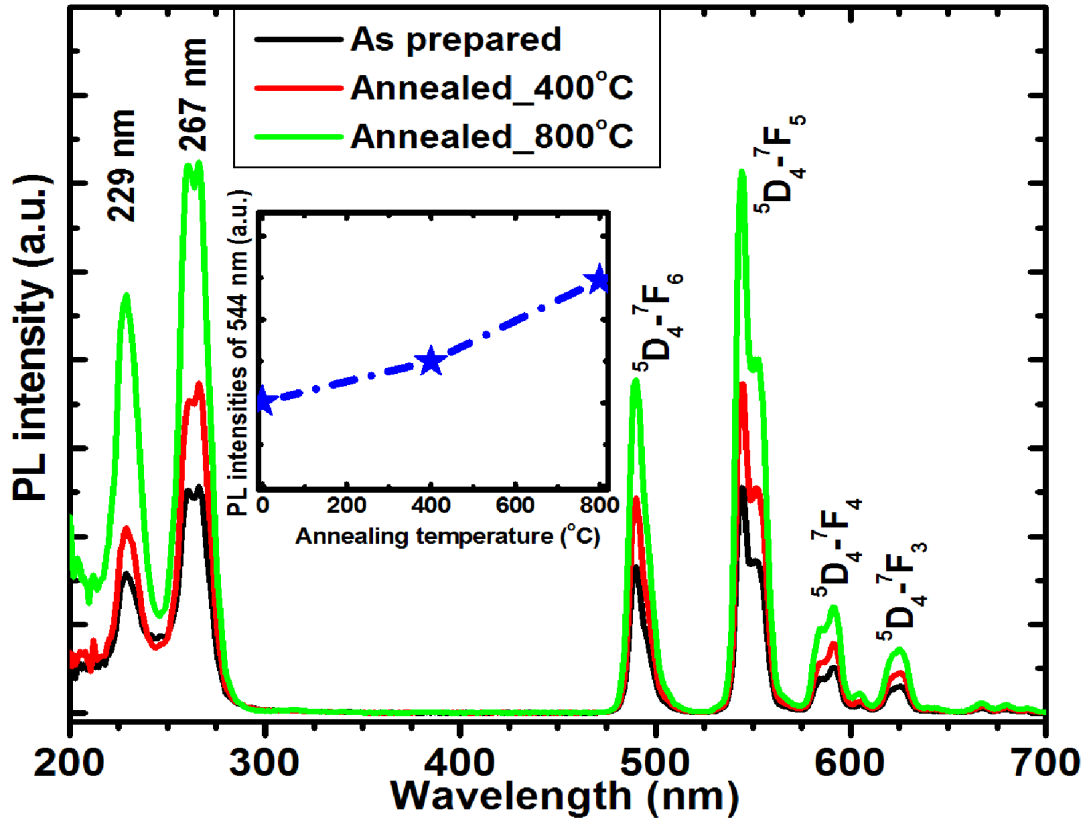
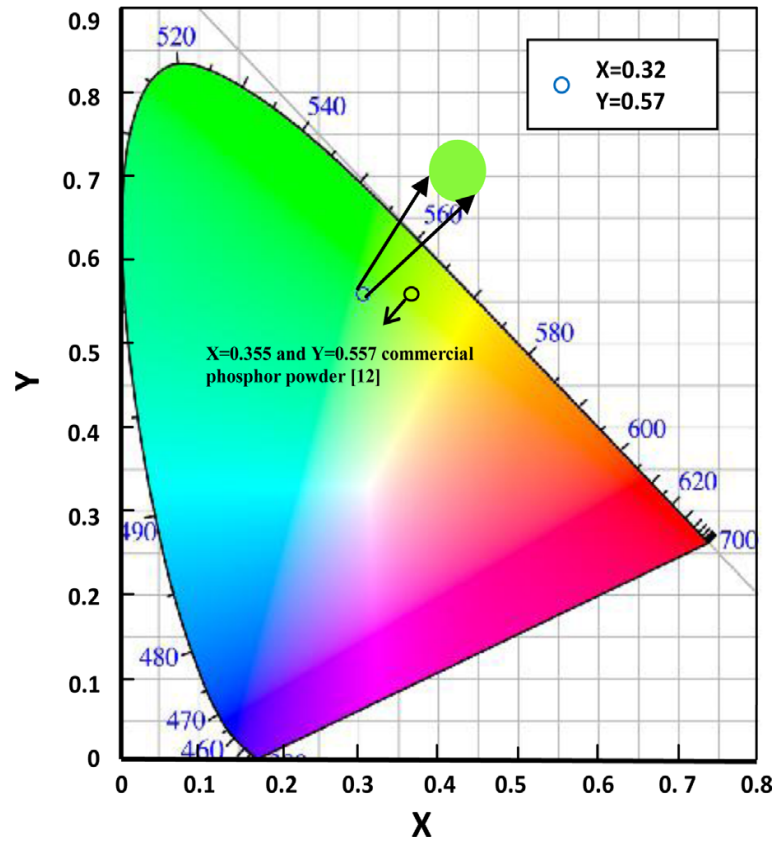


Figure 6.6: PL emissions and PL intensity (inset) as function of annealing temperature.

### 6.3.5 Cathodoluminescence (CL)

Figure 6.8 shows the CL emission spectrum of the deposited  $Y_3(\text{Al}, \text{Ga})_5\text{O}_{12}:\text{Tb}$  film, as function of prolonged electron irradiation (up to  $460 \text{ C}/\text{cm}^2$ ), excited with a 2 keV electron beam at a base pressure of  $1.0 \times 10^{-8}$  Torr. The CL emission spectra are similar to those of the PL with the main peak at 544 nm, suggesting that the electron beam did not change the electron energy level configuration or transitions of the activator ion in the film. The inset of Figure 6.8 shows an exponential decrease of the CL intensity as function of electron dose. The CL intensity was decreased to about 50% after about  $460 \text{ C}/\text{cm}^2$  electron dose. Yousif et al [5] reported on the stability of  $Y_3(\text{Al}, \text{Ga})_5\text{O}_{12}:\text{Tb}$  phosphor powder



**Figure 6.7:** The CIE chromaticity diagram for deposited  $Y_3(\text{Al}, \text{Ga})_5\text{O}_{12}:\text{Tb}$  film.

after 27 hours ( $3000 \text{ C}/\text{cm}^2$  electron dose) of continuous electron irradiation and they attributed it to an electron-beam induced formation of new interleave oxide layers, such as  $\text{AlO}_x$ ,  $\text{YO}_x$  and  $Y_3(\text{Al}, \text{Ga})_5\text{O}_{12}$  on the surface. These oxides acted as protective layers inhibiting further CL intensity degradation during prolonged electron irradiation. The CL emission intensity for the deposited  $Y_3(\text{Al}, \text{Ga})_5\text{O}_{12}:\text{Tb}$  film has been investigated as a function of the accelerating voltage with a filament current fixed at  $10 \mu\text{A}$ , as shown in Figure 6.9. The CL intensity increase with an increase in the accelerating voltage from 1 to 3 keV. The increase of the CL intensity with increasing electron energy is attributed to the deeper penetration of the electron into the film. For CL, the  $\text{Tb}^{3+}$  ion are excited by the excitation produced by the incident electrons. With increasing the

electron penetration depth, the excitation volume increased, which will result in more  $Tb^{3+}$  ions being excited and a subsequent increase in the CL intensity [14].

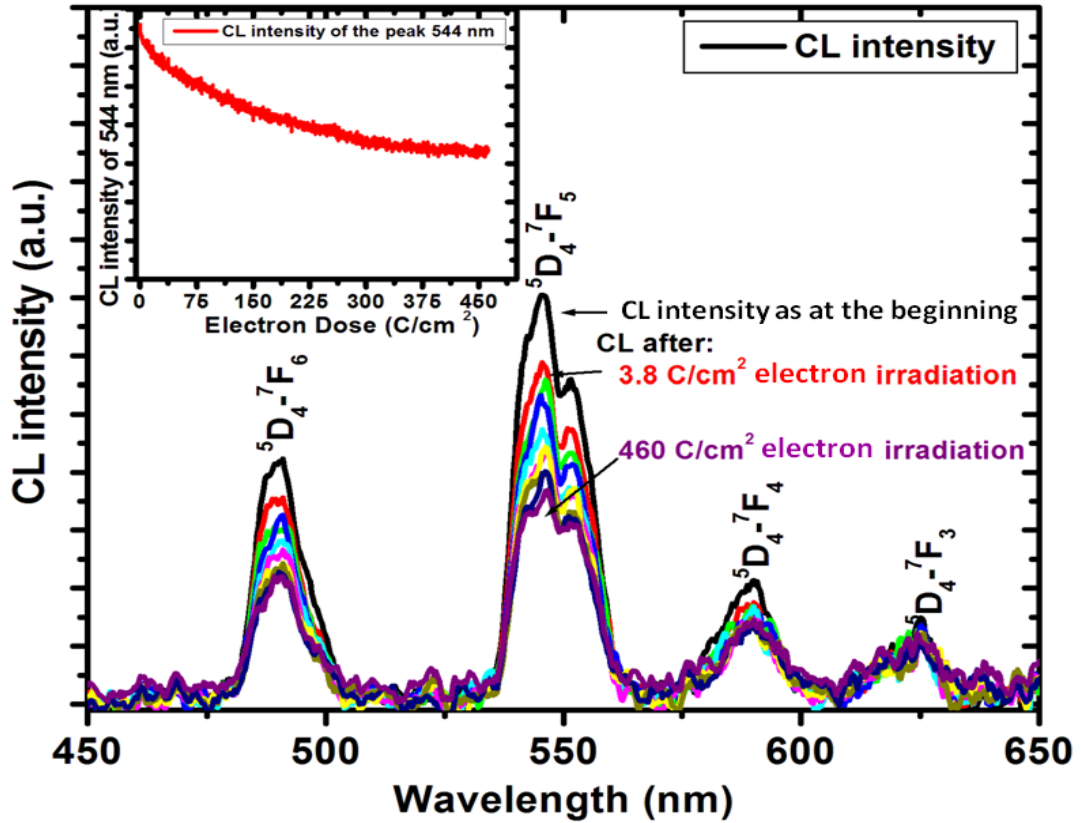


**Figure 6.8:** CL emission and intensity (inset) of the deposited films as a function of prolonged electron irradiation.

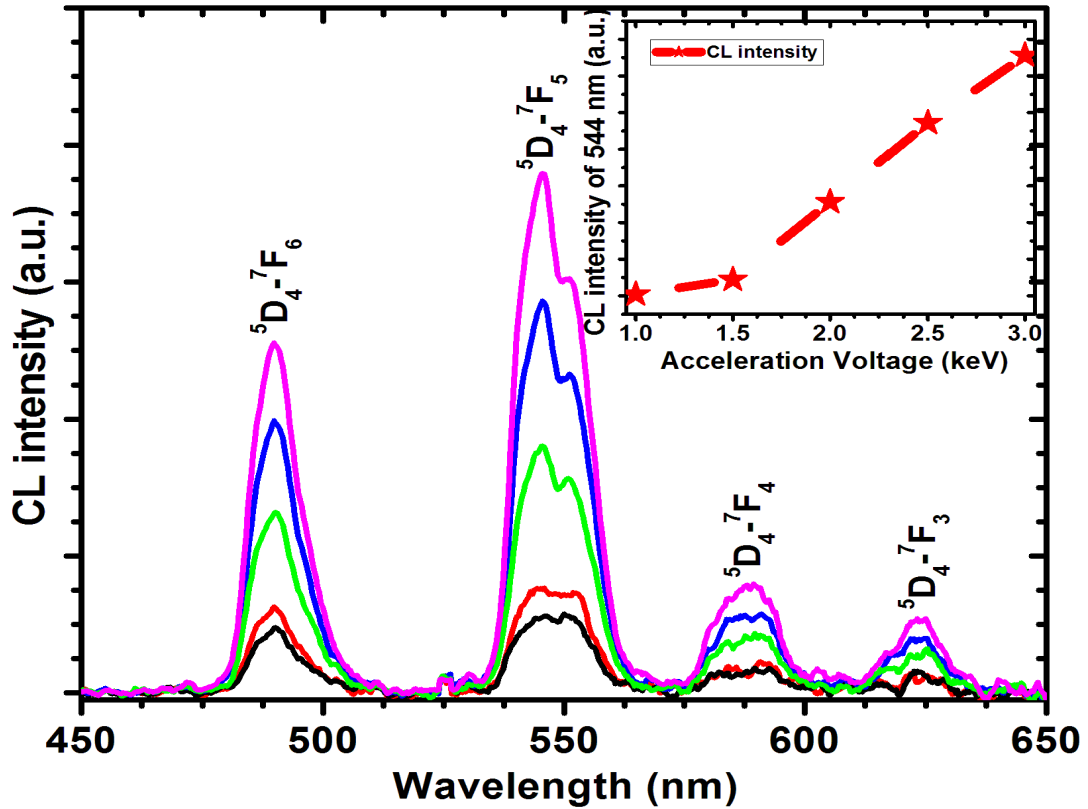


Figure 6.9: The CL emission and intensity (inset) for the deposited  $\text{Y}_3(\text{Al, Ga})_5\text{O}_{12}:\text{Tb}$  film as a function of the accelerating voltage.

## 6.4 Conclusion

Thin films of  $\text{Y}_3(\text{Al, Ga})_5\text{O}_{12}:\text{Tb}$  phosphor were successfully fabricated in an oxygen atmosphere by the PLD method. Post-annealing treatment led to a significant improvement in the luminescence properties of the  $\text{Y}_3(\text{Al, Ga})_5\text{O}_{12}:\text{Tb}$  films as well as a change in the surface topography. The CL emission spectra were similar to the PL emission with a main peak at 544 nm. The decrease in CL intensity as function of prolonged electron irradiation was observed.

## References

- [1] A. M. Chinie, S. Georgescu, A. Mateescu, A. Stefan, Romania Journal of Physics **51** (2006) 827.
- [2] D. Kim, W. Kang, Journal of Bull. Korean Chemistry Soc. **25** (2004) 12.
- [3] J. Y. Choe, D. Ravichandran, S. M. Blomquist, D. C. Morton, K. W. Kirchner, M. H. Ervin, U. Lee, Applied Physics Letters **78** (2001) 24.
- [4] Y. Hu, X. Diao, C. Wang, W. Hao, T. Wang, Vacuum **75** (2004) 183.
- [5] A. Yousif, H. C. Swart, O. M. Ntwaeaborwa, Applied Surface Science **258** (2012) 6495.
- [6] H. C. Swart, E Coetzee, J. J. Terblans, O. M. Ntwaeaborwa, P. D. Nsimama, F. B. Dejene, J. J. Dolo, Applied Physics A Materials Science and Processing **101** (2010) 633.
- [7] O. Katsutoshi, A. Tomohiko, K. Tsuneo, Japanese Journal of Applied Physics **29** (1990) 103.
- [8] A. Yousif, H. C. Swart, O. M. Ntwaeaborwa, E. Coetsee, Applied Surface Science **270** (2013) 331.
- [9] G. A. Hirata, O. A. Lopez, L. E. Shea, J. Y. Yi, T. Cheeks, J. McKittrick, J. Siqueiros, M. Avalos-Borja, A. Esparza, C. Falcony, Journal of Vacuum Science and Technology A **14** (1996) 1694.
- [10] N. D. Zakharov, K. M. Satyalakshmi, G. Koren, D. Hesse, Journal of Materials Research **14** (1999) 11.
- [11] R. E. John, Pulsed Laser Deposition of Thin Films Applications-led Growth of Functional Material, Wiley & Sons, Hoboken, New Jersey, 2007.

## Chapter 6

---

- [12] <http://www.mathworks.com/matlabcentral/fileexchange/29620-cie-coordinate-calculatorS> (accessed 21.10.2012).
- [13] <http://www.phosphor-technology.com/products/crt.htm> (accessed 21.10.2012).
- [14] C. Peng, C. Li, G. Li, S. Li, J. Lin, *Journal of the Royal Society of Chemistry* **41** (2012) 8660.

# Chapter 7

## Conversion of $Y_3(\text{Al}, \text{Ga})_5\text{O}_{12}:\text{Tb}$ to $Y_2\text{Si}_2\text{O}_7:\text{Tb}$ thin film by annealing at higher temperatures

### 7.1 Introduction

Physics and technology of thin phosphor films play an important role in fabrication of smaller devices with high speed especially in the new generations of flat panel displays such as electroluminescent (EL) and field emission displays (FEDs). It is well documented that thin phosphor films have more significant advantages compared to the conventional powder such as high thermal stability, structural density, better adhesion to the underlying substrates and efficient dissipation of heat for high power operation [1]. PLD is a widely used technique to prepare thin phosphor films [2, 3]. Amongst the luminescent materials, yttrium aluminium garnet ( $Y_3(\text{Al}, \text{Ga})_5\text{O}_{12}$ ) or YAG shows great luminescent properties when doped with rare-earth elements [4, 5]. As reported in the literature [6 – 8], the brightness and the saturation characteristics of YAG were improved by the replacement of a portion of the Al with Ga in the matrix.  $Y_3(\text{Al}, \text{Ga})_5\text{O}_{12}:\text{Tb}$  phosphor shows very good cathodoluminescent (CL) stability during prolonged electron bombardment [7] indicating that it is a promising phosphor candidate for FEDs and other applications. It should be noted that the aging of  $Y_3\text{Al}_5\text{O}_{12}:\text{Tb}$  in the epitaxial thin film form is much slower than in the powder form and this is probably due to better dissipation of heat in the epitaxial films [9]. It has been reported that in the initial period of electron irradiation  $Y_3(\text{Al}, \text{Ga})_5\text{O}_{12}:\text{Tb}$  showed slow build-up of the luminescence intensity [9]. This phenomenon might be caused by a process in which the traps are slowly filled against thermal emptying. It was also found that the luminescence intensity could be increased instantaneously by co-doping with  $\text{Yb}^{3+}$  or

$\text{Eu}^{3+}$ . In addition,  $\text{Yb}^{3+}$  or  $\text{Eu}^{3+}$  are capable of decreasing the aging rate of  $\text{Y}_3(\text{Al}, \text{Ga})_5\text{O}_{12}:\text{Tb}$  and  $\text{Y}_3\text{Al}_5\text{O}_{12}:\text{Tb}$ . It is most likely that  $\text{Yb}^{3+}$  and  $\text{Eu}^{3+}$  prevent the feeding of traps responsible for the slow build-up or aging. It would therefore be interesting to monitor the effects of impurities on the luminescent properties of the thin films of either  $\text{Y}_3(\text{Al}, \text{Ga})_5\text{O}_{12}:\text{Tb}$  or  $\text{Y}_3\text{Al}_5\text{O}_{12}:\text{Tb}$  phosphor. In this study,  $\text{Y}_3(\text{Al}, \text{Ga})_5\text{O}_{12}:\text{Tb}$  thin films were pulsed laser deposited on Si(100) substrates in an Ar working atmosphere while the substrate temperature and other processing conditions such as the repetition rate, distance between target to substrate and laser energy density were kept constant during ablation. Post deposition annealing of the samples were found to cause diffusion of Si atoms from the substrate into the thin films. The mechanism of Si diffusion in the formation of silicates reported by Chiam et. al. [10] is still not very clear. Generally, due to the need to break the covalent bonds, silicon mixing in oxides is not expected until a high temperature of 600 °C is reached. However, some studies have shown that this mixing could occur at temperatures as low as 600 °C when silicates are formed during interdiffusion process. This temperature appears to be even lower at 300 °C for the mixing of Y and  $\text{SiO}_2$ . As reported by Shin et al. [11], the formation of single-phase europium silicate crystals from EuO and  $\text{SiO}_2$  requires temperatures as high as 1800 °C for  $\text{Eu}_2\text{SiO}_4$  and 1400 °C for  $\text{EuSiO}_4$ . We could not find reports in the literature about the conversion of  $\text{Y}_3(\text{Al}, \text{Ga})_5\text{O}_{12}:\text{Tb}$  thin films to  $\alpha\text{-Y}_2\text{SiO}_7:\text{Tb}$  by diffusion of Si from the substrate due to high temperature annealing. It is therefore important to develop a better understanding of the kinetics of the film formation, as this may be different for various growth conditions. In order to have a better understanding of the film growth and interfacial reactions, high annealing-temperature studies should be performed to phase separate the possible rapid reactions occurring at high temperatures. Such studies could also reveal path ways for interfacial or bulk film formation, especially for a silicate film. In this work, we report on the high temperature annealing studies of  $\text{Y}_3(\text{Al}, \text{Ga})_5\text{O}_{12}:\text{Tb}$  films on Si(100).

Changes in the excitation and emission peaks after annealing were monitored to determine the effect of the Si interdiffusion in the  $Y_3(Al, Ga)_5O_{12}$  matrix. XRD and XPS were used to analyze the changes that occur in the structural properties of the thin films as a result of post deposition annealing.

## 7.2 Experimental

A commercial  $Y_3(Al, Ga)_5O_{12}:Tb$  powder phosphor, obtained from Phosphor Technology was pressed without binders using an in-house built sample holder and was used as an ablation target. The target was annealed at 600 °C for 2 hrs in air to get rid of all adventitious water containing species that might be present in the pellet and was then placed inside the chamber of the PLD system on a rotating target holder that can also move linearly (up and down). Note that the rotational as well as linear motion of the target rod restricted the laser ablation induced degradation of the target surface. Si(100) wafers were used as substrates after cleaning with ethanol for 15 min, in an ultrasonic water bath and then blown dry with nitrogen ( $N_2$ ) gas. The deposition chamber was evacuated to a base pressure of  $1.4 \times 10^{-5}$  mbar and then backfilled with Ar gas to a pressure of 20 mbar. The  $Y_3(Al, Ga)_5O_{12}:Tb$  target was in the Ar working atmosphere using a 266 nm Nd:YAG 266 pulsed laser. The laser frequency, number of pulses fluency, substrate temperature and target-to-substrate distance were fixed at 10 Hz, 10000,  $0.767 \text{ J/cm}^2$ , 300 °C and 4.5 cm, respectively. The deposited thin films were annealed in air for 3 hrs at (a) 800 °C, (b) 1000 °C and (c) 1200 °C. XRD analysis was carried out using a Bruker AXS D8ADVANCE X-ray diffractometer, with a  $Cu \text{ } k\alpha_1$  ( $1.5406 \text{ \AA}$ ) in the  $2\theta$  range from  $17^\circ - 37.5^\circ$ , with a counting time of 1 s for each step size of  $0.015^\circ$ . Photoluminescent (PL) properties of the films were measured using a Carry eclipse spectrophotometer at room temperature excited by mono-chromatized Xenon flash lamp. The surface morphology and roughness were examined from

images captured in contact mode using Shimadzu SPM-9600 AFM. The root mean square (RMS) roughnesses were estimated by analyzing the topography scans the films surfaces using commercial software. The CL degradation data were collected using Ocean Optics PC2000 spectrometer attached to the vacuum chamber of the PHI 545 Auger electron spectrometer and the data were recorded using OOI Base32 computer software. Thermoluminescence (TL) data were collected with a TL 10091, NUCLEONLX spectrometer and the data were fitted with a TL Glue Curve Analyzer. XPS was used to analyze the electronic states of the thin films before and after annealing using a PHI 5000 Versaprobe-Scanning ESCA Microprobe. The survey scans were recorded with a 100  $\mu\text{m}$ , 25 W, 15 kV beam using monochromatic Al  $K_{\alpha 1}$  radiation ( $h\nu = 1486.6$  eV) and for the higher resolution spectra the hemispherical analyzer pass energy was maintained at 11.8 eV (C1s, O1s, Y3d and Si2p) for 50 cycles. Measurements were performed using either a 1 eV/step and 45 min. acquisition time (binding energies ranging from 0-1400 eV) for survey scans or a 0.1 eV/step and 20-30 min. acquisition times for the high resolution scans and 90 min. The pressure during acquisition was typically under  $1.33 \times 10^{-8}$  mbar. MULTIPAK software [12] was used to fit/deconvolute the peaks. Depth profiling experiments were conducted to determine the thicknesses of the films and to obtain information on the variation of chemical composition with the depth below the initial surface. The film surfaces were sputtered using an Ar ion gun (2 kV energy ions) at the rate of about 0.8 nm/min.

## 7.3 Result and discussion

### 7.3.1 Structural and morphology analysis

Figure 7.1 shows the XRD spectra of the  $\text{Y}_3(\text{Al}, \text{Ga})_5\text{O}_{12}$  powder, the as deposited and annealed  $\text{Y}_3(\text{Al}, \text{Ga})_5\text{O}_{12}$  thin films. The XRD pattern of the pow-

der is consistent with the cubic (Ia-3d(230))  $Y_3(Al, Ga)_5O_{12}$  phase and ICSD data file No. 029248 [13]. No diffraction peaks were observed from the as deposited films suggesting that the film was amorphous. Two diffraction peaks located at  $29.32^\circ$  and  $32.82^\circ$  were obtained from the film annealed at  $800^\circ C$  improvement in the film crystal structure. The film was preferentially orientated in the (420) direction. When the annealing temperature was increased to  $1000^\circ C$  diffraction three diffraction peaks oriented in the (400), (420) and (422) were obtained. Totally different diffraction pattern was observed when the annealing temperature was increased further to  $1200^\circ C$  indicating that  $Y_3(Al, Ga)_5O_{12}$  was converted into new compound(s) at this temperature. The peaks labelled with an asterisk (\*) in the spectrum are in agreement with the  $Y_2Si_2O_7$  pattern of the ICSD file no. 361476 (DATA) indicating that  $Y_2Si_2O_7$  was formed as a result of atomic interdiffusion between the substrate and the film when the films were annealed between  $800^\circ C$  and  $1200^\circ C$ . An additional new peak marked with an exclamation mark (!) is similar to the (100) diffraction peak from  $SiO_2$ . The surface topography of the as deposited and annealed thin films was studied using AFM. Figure 7.2 (a) and (b) show respectively the three dimensional AFM images of the as deposited thin film and the film annealed at  $1200^\circ C$ , which were captured over an area of  $3 \times 3 \mu m$ . Figure 7.2 (a) shows well defined spherically grains that are uniformly distributed over the surface with a root mean square (RMS) roughness of 20 nm. The surface topography changed completely after annealing at  $1200^\circ C$  as seen in Figure 7.2 (b), indicating that a new surface structure that did not have defined grain boundaries was formed. The surface roughness was in the order of 9 nm. It can be concluded that the annealing has an influence on the surface structure, the grains shape and sizes of the thin film.

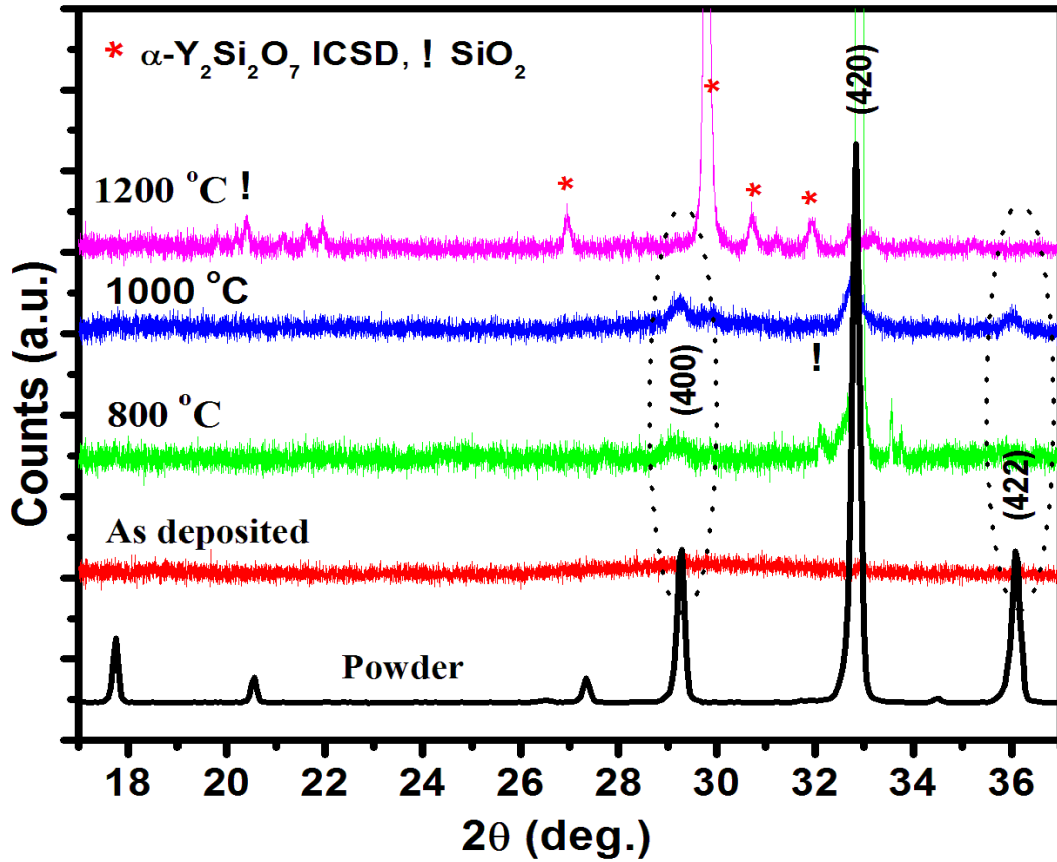
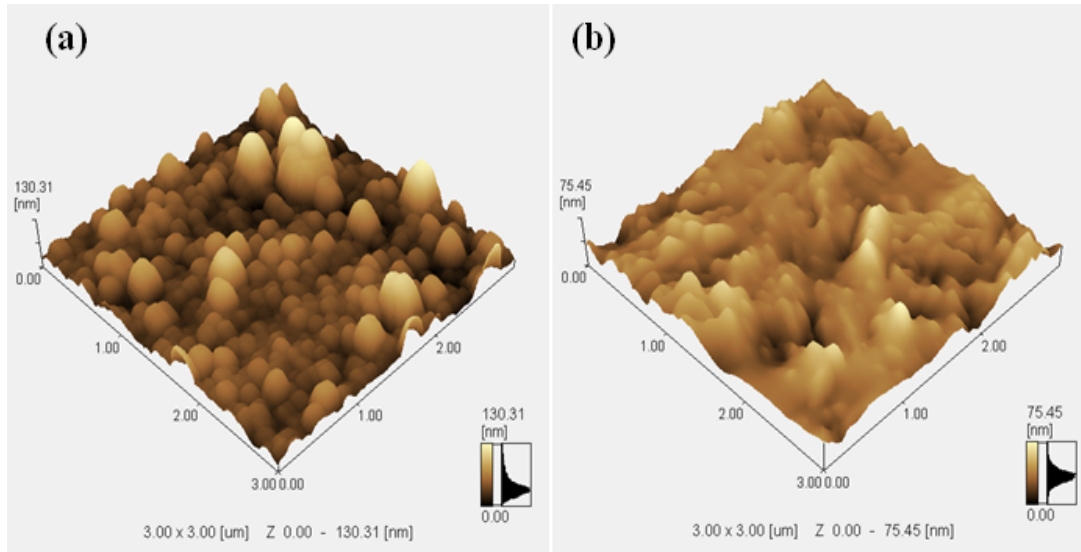


Figure 7.1: XRD spectra of  $\text{Y}_3(\text{Al, Ga})_5\text{O}_{12}:\text{Tb}$  phosphor powder, unannealed and annealed thin films with the standard ICSD data of  $\alpha\text{-Y}_2\text{SiO}_7$ .

### 7.3.2 PL and CL results

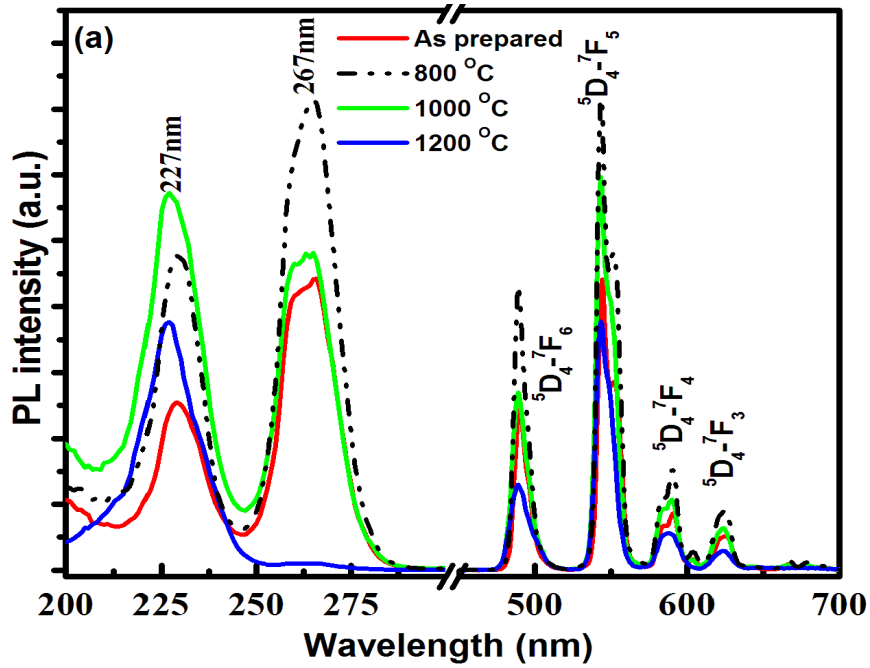
Figure 7.3(a) shows the PL excitation and emission spectra of  $\text{Tb}^{3+}$  for the as deposited (unannealed) films and for those annealed at 800 °C, 1000 °C and 1200 °C. The excitation spectrum consists of two ultraviolet (UV) bands at 227 nm and 267 nm. The films were excited using the wavelength that gave the maximum intensity between the two bands. The emission spectra consist of peaks at 489 nm, 544 nm, 590 nm and 625 nm which correspond to the ( $^5\text{D}_4 \rightarrow ^7\text{F}_6$ ), ( $^5\text{D}_4 \rightarrow ^7\text{F}_5$ ), ( $^5\text{D}_4 \rightarrow ^7\text{F}_4$ ) and ( $^5\text{D}_4 \rightarrow ^7\text{F}_3$ ) transitions of  $\text{Tb}^{3+}$  respectively [7, 14, 15]. The green emission at 544 nm due to the  $^5\text{D}_4 \rightarrow ^7\text{F}_5$  transition is the strongest. The main emission peak and that at 561 nm are



**Figure 7.2:** AFM images of the surface of (a)  $\text{Y}_3(\text{Al, Ga})_5\text{O}_{12}:\text{Tb}$  thin films as prepared and (b) after annealed at  $1200\text{ }^\circ\text{C}$ .

split due to the influence of the crystal field [15] and this was obvious from the film annealed at  $800\text{ }^\circ\text{C}$  whose structure resembles that of the  $\text{Y}_3(\text{Al, Ga})_5\text{O}_{12}:\text{Tb}$  powder. The splitting is not that obvious in the rest of the PL emission spectra from the films annealed at other temperatures probably because of the change in structure (as discussed above) and hence the crystal field. Furthermore, it is well known that, the lanthanide elements (rare earth) have a partially filled inner  $4f^n$  shell surrounded by completely filled outer  $5s^2$  and  $5p^6$  orbitals which prevent the sharp  $4f-4f$  line emissions of the  $\text{Tb}^{3+}$  from the anionic environment i.e. are relatively independent of the host material and are determined by the energy transition between the  $4f$  states only. On the other hand, the energy of the  $5d$  levels depends strongly on the nature of the host due to a greater radial extension of the  $5d$  orbital, which may be used to explain the changes in the excitation bands observed in Figure 7.3. The relative ratios of the maximum intensities of the two excitation bands annealed at different temperatures are shown in Figure 7.3 (b). Before annealing the excitation band at  $267\text{ nm}$  was more intense than the  $227\text{ nm}$  and the ratios of their maximum intensities of the

267 to 227 nm excitations were 1.7, 1.5, 0.8 and 0.03 after annealing at 800 °C, 1000 °C and 1200 °C respectively. After annealing the excitation band at 227 nm become more dominate, which is the characteristic absorption transition of  $Tb^{3+}$  from the  $4f^8$  ground state to the excited  $4f^75d^1$  state in  $\alpha - Y_2Si_2O_7:Tb$  phosphor [16].



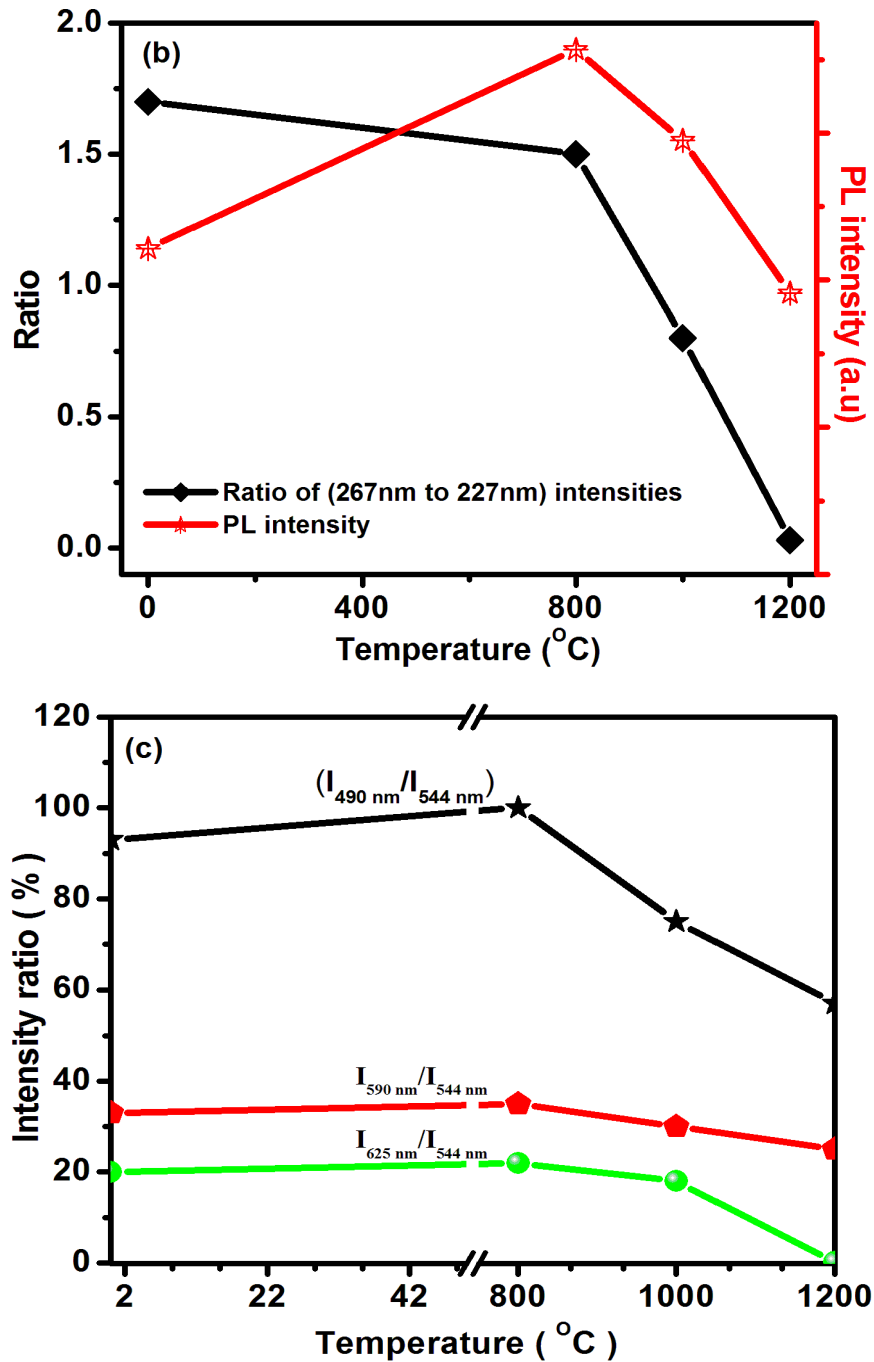


**Figure 7.3:** (a) PL emission and excitation spectra of as prepared and annealed thin films. (b) The relative ratio of the intensities of the 267:227 nm excitation bands, showing the relative change of the excitations bands from 267 nm to 227 nm. (c) Relative emission ratio intensities as a function of the different annealing temperatures of the films.

In order to investigate the change of the films structures on the  $Tb^{3+}$  emission intensities after annealing at different temperatures, the ratio of the maximum intensity of the strongest green emission peak at 544 nm to that of other peaks at 489 nm, 590 nm and 625 nm were calculated. Figure 7.3 (c) shows the graph of the ratio of the maximum intensity as a function of temperature (i.e. change in the films structure). The intensity ratio of  $I_{490nm}/I_{544nm}$  and  $I_{625nm}/I_{544nm}$  gradually decreased when the annealing temperature was increased from 800 °C to 1200 °C. On the other hand, the intensity ratio of  $I_{590 nm}/I_{544nm}$ , is less affected by the change in the films structure compared to other peak intensity ratios. The CL emission spectra of  $Y_3(Al, Ga)_5O_{12}:Tb$  thin films before and after a prolonged exposure to  $900 C/cm^2$  electron dose for the as deposited and annealed (1200 °C) films are shown in Figures 7.4 (a) and (b), respectively. The

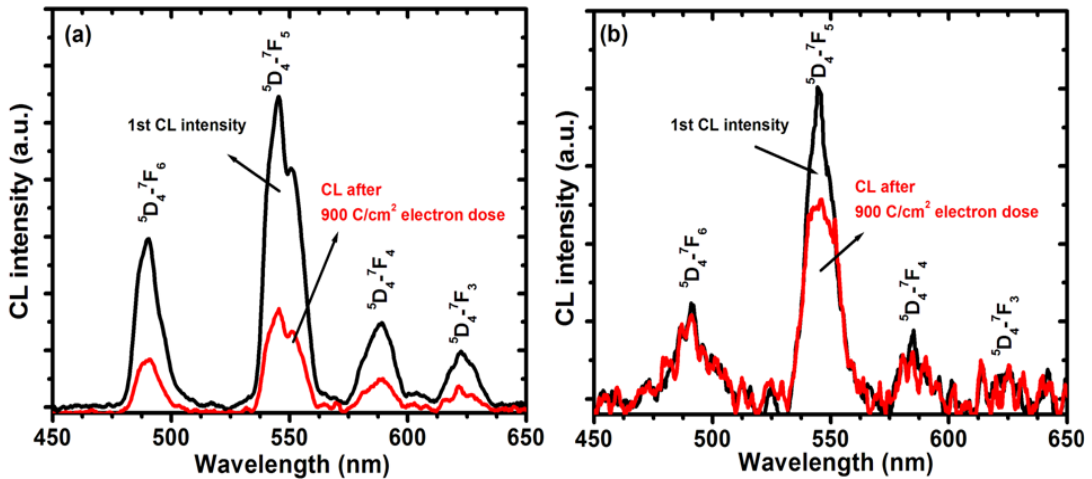


**Figure 7.4:** (a) and (b) CL intensities before and after electron beam exposure of the  $Y_3(Al, Ga)_5O_{12}:Tb$  unannealed and annealed films (1200 °C), respectively.

CL intensity is given in arbitrary units (a.u.) because there was no calibrated light source inside the UHV chamber when measurements were taken. The CL emission spectra are similar to those of the PL with a main emission peak at 544 nm, suggesting that the electron beam did not change the electron energy level configuration or transitions of the activator ion in the film. Exposure

to the electron beam of  $900 \text{ C/cm}^2$  electron dose has reduced the intensity of the main emission peak (544 nm) of the as-deposited film in Figure ?? (a) by approximately 70%, while the decrease of the emission peak intensity from the annealed film was minimal. However, the CL intensity of the annealed film was much less than that of the as-deposited film. Figure 7.5 shows the CL intensities as a function of electron beam exposure for the as-deposited and annealed  $\text{Y}_3(\text{Al}, \text{Ga})_5\text{O}_{12}:\text{Tb}$  films. The rate of degradation of CL intensity was much faster for the as-deposited film compared to that of the annealed film and this was probably due to the crystallinity and different crystal structure of the films. The CL intensity of the  $\text{Y}_3(\text{Al}, \text{Ga})_5\text{O}_{12}:\text{Tb}$  powder was comparatively stable when exposed to electron beam [7]. The degradation of the CL intensity during prolonged electron bombardment is not new and is well described by Swart et al. [17]. The degradation is due to ESSCR (electron stimulated surface chemical reactions).

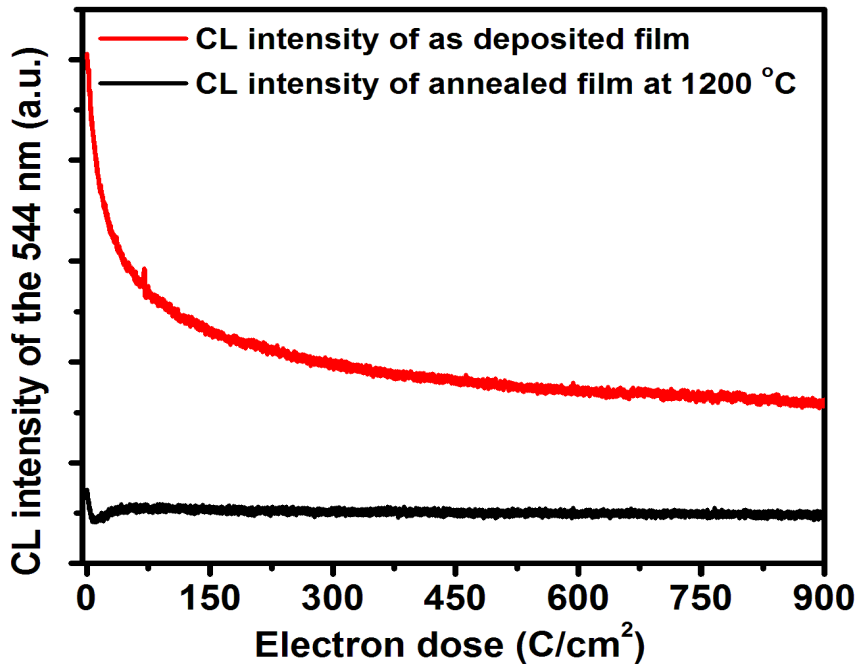


**Figure 7.5:** CL intensities as a function of electron beam exposure for the  $\text{Y}_3(\text{Al}, \text{Ga})_5\text{O}_{12}:\text{Tb}$  unannealed and annealed films (1200 °C).

### 7.3.3 Thermoluminescence (TL)

TL is the thermally stimulated emission of light after absorption of energy from a radiation source [17]. The intensity of light as a function of time or temperature is called a glow curve. This glow curve can be studied to determine the internal traps created in an emitting material that has been exposed to ionizing radiation. The glow curves are traditionally analyzed with an empirical method in which the order of kinetic can be determined. According to the simple thermoluminescence model [18] when thermal energy is applied to the TL material the trapped electrons are excited to the conduction band and have different possibilities to be de-excited. One is the recombination with the hole accompanied by the TL light emission and the other one is retrapping in which the electron return to similar traps. Two descriptions were given to the way of trapped electrons to be de-excited, one is the first order kinetics where the probability of retrapping the electron is negligible and the glow curve has a narrow peak shape due to a rapid recombination process. The other is the second order kinetics where the retrapping dominates, the recombination with the holes is suppressed and the curve has a wider decay tail peak. Between these two types, the general order kinetics is introduced for providing a proper analytic continuation from the discrete two types of kinetics. The TL light intensities for the first, second and general order kinetic processes have been given by Randall-Wilkins, Garlick-Gibson and May Partridge [18] respectively and are expressed as

$$I(t) = nse^{-E/k_g T} \quad (7.1)$$

$$I(t) = (n^2/N)se^{-E/k_g T} \quad (7.2)$$

$$I(t) = n^b s' e^{-E/k_g T} \quad (7.3)$$

where  $E$  is the activation energy or trap depth (eV),  $K_g$  is Boltzmanns constant (eV  $K^{-1}$ ),  $t$  the time (s),  $T$  the absolute temperature (K),  $s$  a constant characteristic of the electron trap, called the pre-exponential frequency factor or attempt-

---

to-escape frequency,  $n$  the concentration of trapped electrons at time  $t$  ( $m^{-3}$ ),  $b$  the kinetic order,  $a$  a parameter with values typically between 1 and 2,  $s$  the so-called effective pre-exponential factor for general order kinetics ( $m^{3(b-1)}s^{-1}$ ) and  $N$  the total trap concentration ( $m^{-3}$ ). The integration of equations (7.1), (7.2) and (7.3) for a linear heating rate  $\beta$ , is respectively [18]

$$I(t) = n_0 s \exp(-E/K_g T) \exp \left[ -s/\beta \int_{T_0}^T \exp(-E/K_g T') dT' \right] \quad (7.4)$$

$$I(t) = n_0^2 s' \exp(-E/K_g T) \exp \left[ -s/\beta \int_{T_0}^T \exp(-E/K_g T') dT' \right] \quad (7.5)$$

$$I(t) = s'' n_0 \exp(-E/K_g T) \exp \left[ 1 + s''(b-1)/\beta \int_{T_0}^T \exp(-E/K_g T') dT' \right]^{(-b/(b-1))} \quad (7.6)$$

The luminescence glow peaks for the as-deposited and annealed thin films are presented in Figure 7.6. The TL spectrum of the  $Y_3(Al, Ga)_5O_{12}:Tb$  powder phosphor is shown in the inset. The glow curves were obtained in the linear heating range with an acquisition from 32 °C to 375 °C at a heating rate of 2 °C  $s^{-1}$ , after the samples were exposed to UV radiation for 5 min. In order to verify that the TL signal observed on the irradiated films was not coming from the Si substrate, the Si wafer (substrate) was also irradiated by UV for 5 min. The TL response of the Si wafer was subtracted from the films data. In the inset of Figure 7.6, the characteristic glow curve of the  $Y_3(Al, Ga)_5O_{12}:Tb$  powder exhibited two peaks centered at 77 °C, which is the maximum, and 243 °C. The glow curves for the films shows broad peaks in the range of 150 °C to 350 °C, 50 °C to 373 °C for the as deposited films and the films that were annealed at 800 °C, 1000 °C and 1200 °C. respectively. The experimental results were fitted by a set of kinetic models (the first, second and the general kinetic order) as presented in Figure 7.7. Tables 7.1, 7.2, 7.3 and 7.4 give the kinetic parameters for the fitted peaks. As seen from tables 1 to 5 defect levels were located between 0.5 and 1.5 eV and were different for different annealing temperatures. It is clear that the kinetic behaviors of the films glow curves changed during an increase in

the annealing temperature, probably due to the presence of the Si in the films as well as the new phases that formed during annealing.

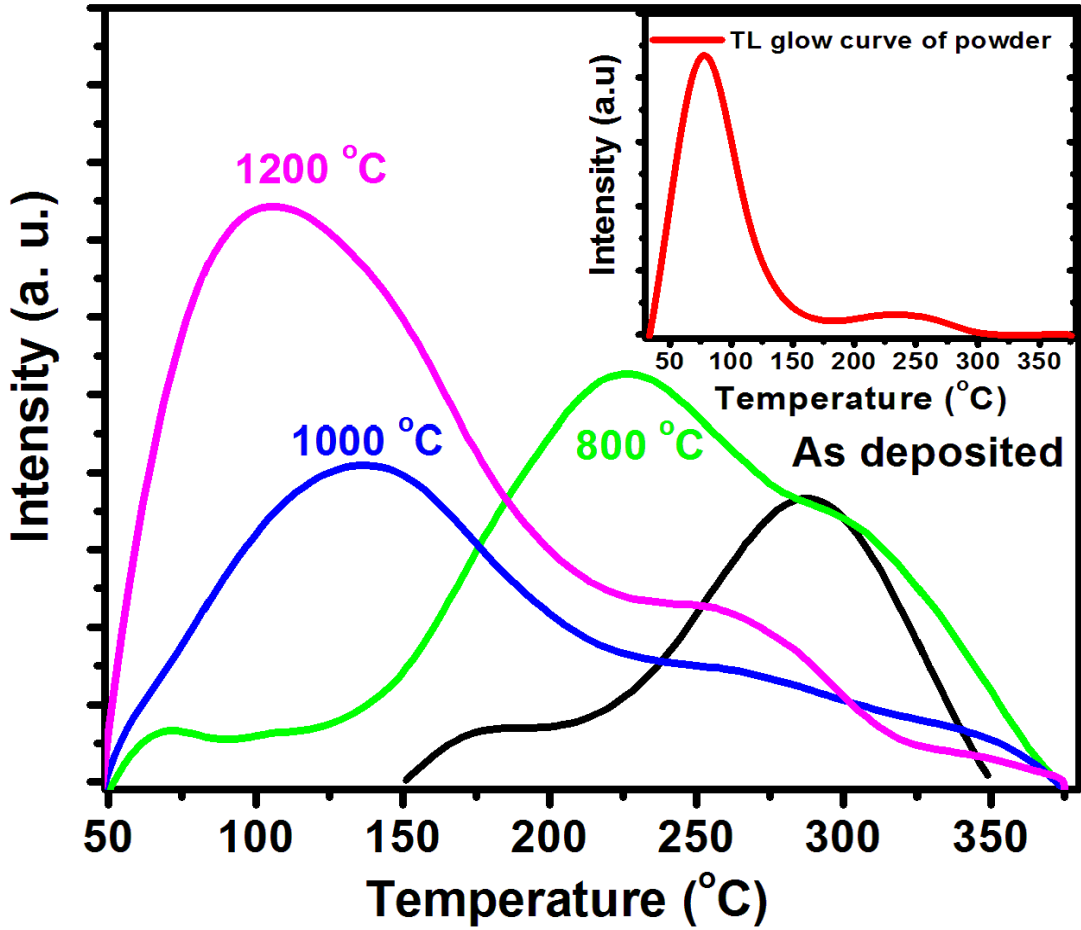


**Figure 7.6:** Change in thermally stimulated luminescence glow curves for unannealed and annealed thin films after different annealing temperatures, 800 °C, 1000 °C and 1200 °C, respectively.

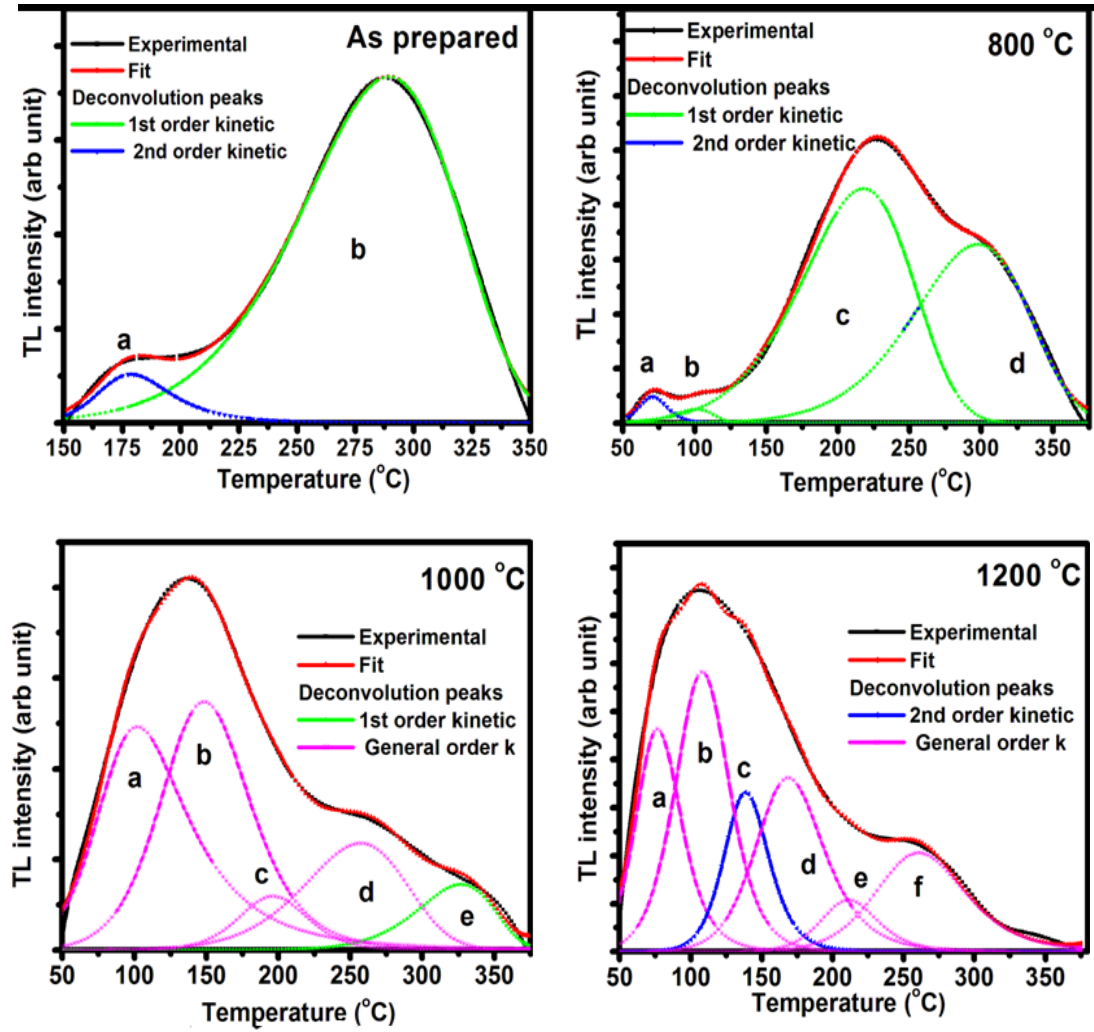


**Figure 7.7:** Deconvolution of the films glow curves with a set of kinetics models for unannealed and annealed thin films after different annealing temperatures, 800 °C, 1000 °C and 1200 °C, respectively.

Table 7.1: The kinetic parameters for the unannealed fitted peak.

Unannealed fitted peak	Kinetic model	$n_0$ ( $10^6 \text{cm}^{-3}$ )	E (eV)	s ( $10^6 \text{s}^{-1}$ )	$s'$ ( $10^{11} \text{s}^{-1}$ )
a	2 <sup>nd</sup> order kinetic	8.0	1.5	-	9.6
b	1 <sup>nd</sup> order kinetic	0.5	0.8	4.0	-

Table 7.2: The kinetic parameters for the annealed fitted peak (800 °C).

Annealed fitted peak at 800 °C	Kinetic model	$n_0$ ( $10^4 \text{cm}^{-3}$ )	E (eV)	s ( $10^{10} \text{s}^{-1}$ )	$s'$ ( $10^{16} \text{s}^{-1}$ )
a	2 <sup>nd</sup> order kinetic	1.1	1.5	-	5.7
b	1 <sup>nd</sup> order kinetic	0.3	0.8	2.9	-
c	1 <sup>nd</sup> order kinetic	8.4	0.5	$0.6 \times 10^{-5}$	-
d	1 <sup>nd</sup> order kinetic	0.2	0.7	3.6	-

### 7.3.4 XPS analysis

The XPS depth profiles for the phosphor powder, as deposited (unannealed) and annealed thin films are shown in Figures 5.6 and 7.8. In all the depth profiles, the main elements present in  $\text{Y}_3(\text{Al}, \text{Ga})_5\text{O}_{12}:\text{Tb}$ , i.e. Y, Al, Ga, O and even the dopant  $\text{Tb}^{3+}$  were detected. In addition, the adventitious C and Si from the substrate were also detected. The depth profile of the powder is presented

Table 7.3: The kinetic parameters for annealed fitted peak (1000 °C).

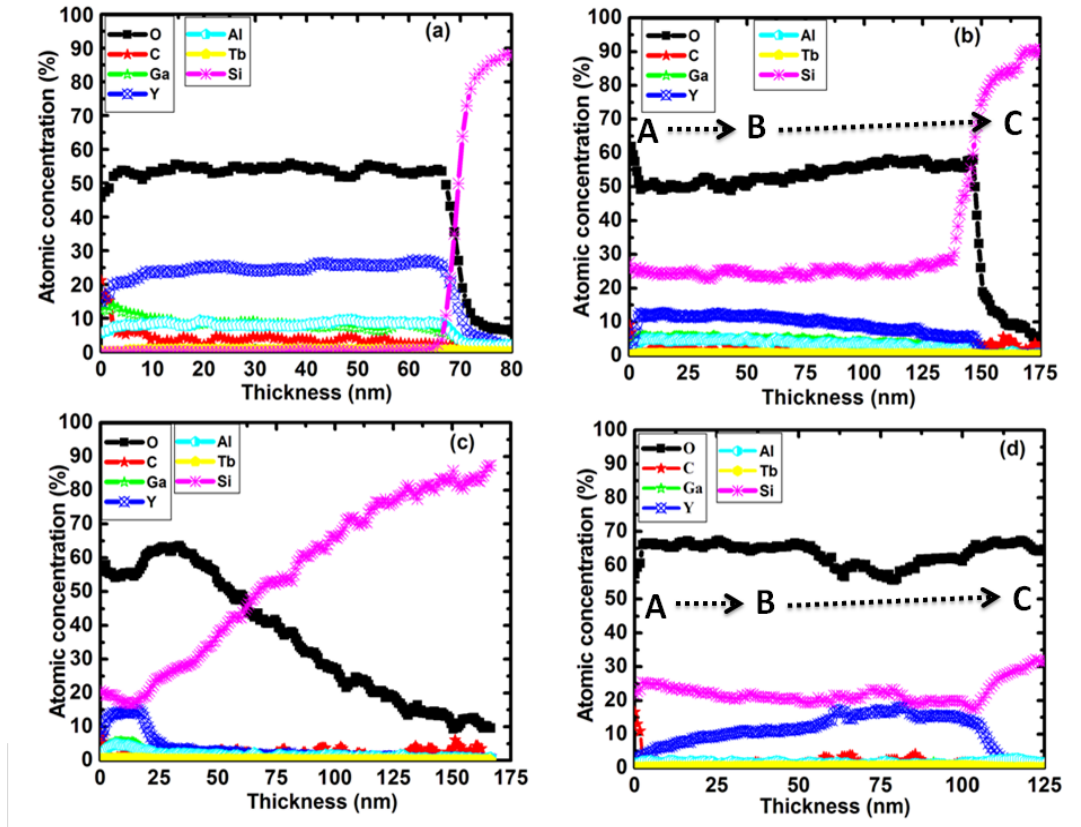
Annealed fitted peak at 1000 °C	Kinetic model	$n_0$ ( $10^5 \text{cm}^{-3}$ )	E (eV)	s ( $10^8 \text{s}^{-1}$ )	$s''(10^{16} \text{s}^{-1})$	b
a	General order	0.5	0.6	-	1.9	2.0
b	General order	5.7	1.1	-	0.3	1.8
c	General order	0.9	1.0	-	$1.5 \times 10^{-3}$	1.7
d	General order	2.7	0.7	-	0.01	1.1
e	1 <sup>st</sup> order kinetic	1.2	1.1	2.4	-	-

Table 7.4: The kinetic parameters for annealed fitted peak (1200 °C).

Annealed fitted peak at 1200 °C	Kinetic model	$n_0$ ( $10^5 \text{cm}^{-3}$ )	E (eV)	s ( $10^8 \text{s}^{-1}$ )	$s''(10^{16} \text{s}^{-1})$	b
a	General order	4.9	0.9	-	1.0	2.1
b	General order	7.3	1.3	-	0.002	-
c	2 <sup>ad</sup> order kinetic	3.5	0.8	5.7	-	1.9
d	General order	5.9	1.0	-	0.021	2.0
e	General order	1.4	1.4	-	3.9	1.9
f	General order	4.3	1.0	-	0.0001	1.8

in figure ?? and it was used as a reference for the atomic concentration of the target. The depth profile composition of the as deposited film in Figure 7.8 (a) has a slight enrichment in O and Ga compared to the the concentrations of O and Ga from the powder. It can be confirmed from this figure that the stoichiometry of the target,  $\text{Y}_3(\text{Al}, \text{Ga})_5\text{O}_{12}:\text{Tb}$  material was transferred and the

film was grown there was no diffusion of Si in during the ablation process. The depth profile for the annealed film at 800 °C presented in Figure 7.8 (b) shows the diffusion of Si from the substrate into the film layer, probably through the grain boundaries. In this instance, it can be seen that, a new film's composition starts to develop which is different from the original material. Figure 7.8 (c) shows the compositional profiles of the thin films after thermal annealing at 1000 °C, which confirms that new phases were formed. After post-deposition annealing at 1200 °C, only Y, O, and Si were present as shown in Figure 7.8 (d). This indicates that the composition of this film was different from that of the original film (i.e. before annealing) and this result is consistent with the XRD data which showed that new phases were formed after annealing the films at temperatures greater than 800 °C. In order to monitor the reaction and diffusion of Si in the thin  $Y_3(Al, Ga)_5O_{12}:Tb$  films at the three different annealing temperatures of 800 °C, 1000 °C and 1200 °C the high resolution XPS peaks were monitored. Si 2p peaks were selected and presented as three dimensions depth profiles for the films annealed at 800 °C and 1200 °C, after 60 min, 155 min, 37 min and 135 min as shown in the first and second parts of Figures 7.9 (a-d). Figures 7.9 (a and c) shows the presence of Si atoms in the  $Y_3(Al, Ga)_5O_{12}:Tb$  film structure. It is clear from the Si peak position and shape that the new compounds formed were different for different films and also that the same compound formed in a particular film was not homogeneous. By using the depth profiles as represented in Figure ??, it can be concluded that, the energy positions of the Si 2p ( $\sim 100$  to 106 eV) are related to a combination of Y-Si-O and Si-O and there was no evidence for combination of Si with the rest of the elements. As reported by J. J. Chambers et. al. [20], when a reactive metal is deposited onto silicon and oxidized at elevated temperatures, the metal can react with silicon and oxidizes. This can be used to explain the results of the annealed films, which shows more Si diffusion through the thin films structure and leading to the formation of films with a significant fraction of Y-Si-O bonds as presented in the depth profiles.



**Figure 7.8:** The XPS depth profiles for  $Y_3(Al, Ga)_5O_{12}:Tb$  thin film phosphors (a) as prepared, (b-d) annealed in air at 800 °C, 1000 °C and 1200 °C, respectively. A, B and C show the beginning and end positions of the 3D XPS profiles.

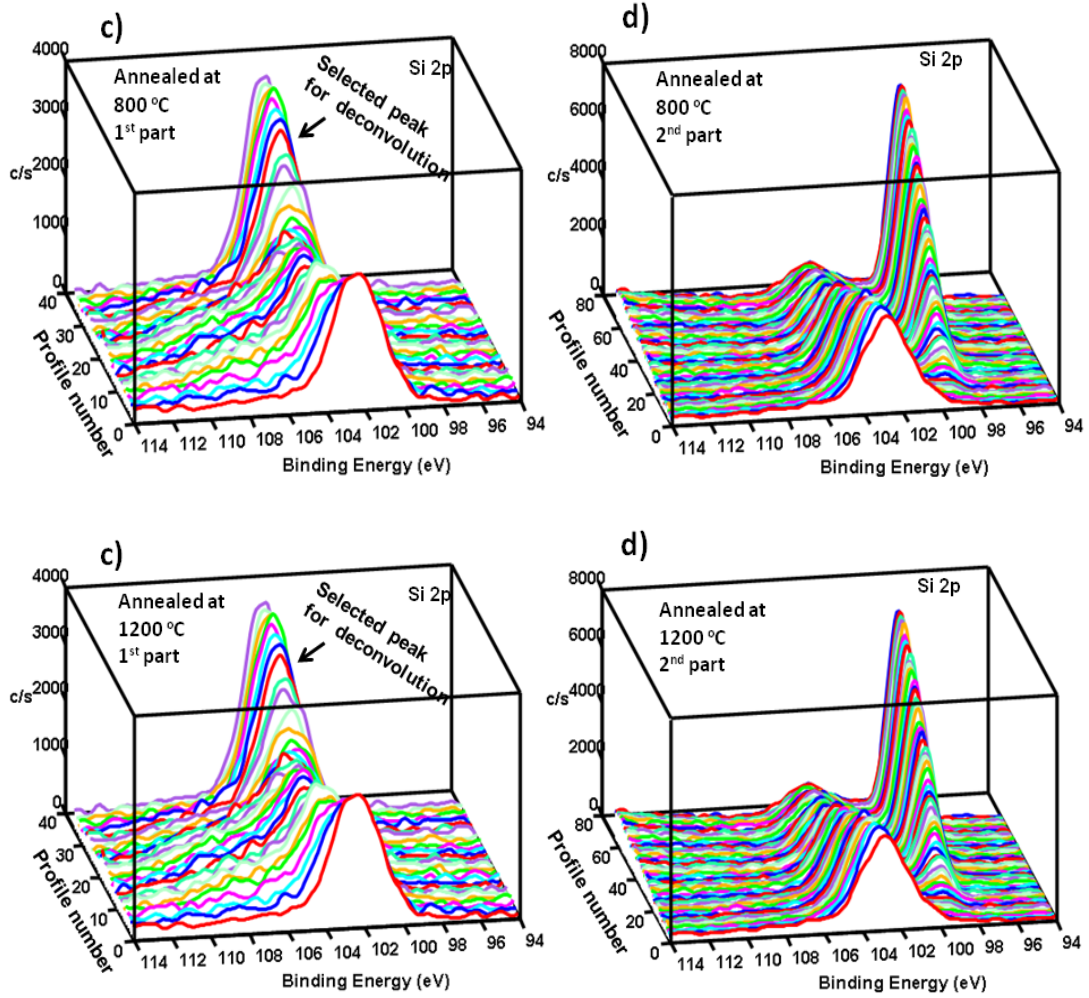


**Figure 7.9:** XPS depth profiles of selected Si (2p) signals of the films (a and b) annealed at 800 °C (c and d) annealed at 1200 °C. 1st Part from A to B and 2nd Part from B to C as indicated in Figure 7.8

Deconvolution of selected Si 2p peaks in  $Y_3(Al, Ga)_5O_{12}:Tb$  after heat treatment at 800 °C and 1200 °C are given in Figure 7.10 (a) and (b). The positions of the selected peaks are indicated on the depth profiles and the 3D XPS data. The binding energies for the deconvolution peaks are listed in Table 5. The Si 2p peak can be fitted with four and three peaks for the film annealed at 800 °C and 1200 °C, respectively. The four fitted peaks are ascribed to the Si bonding in  $SiO_x$ ,  $SiO_2$ ,  $\alpha-Y_2SiO_7$  and Y-Si-O [11, 19]. The three fitted peaks can be attributed to the Si bonding in  $SiO_2$ ,  $\alpha-Y_2SiO_7$  and Y-Si-O [11, 19]. The XPS depth profiles results show that annealing caused the formation of new interleave oxide layers, such as  $SiO_x$ ,  $SiO_2$ ,  $\alpha-Y_2SiO_7$  and Y-Si-O which were not observed in the original film structure. These oxide layers are responsible for the change in surface morphology, the ratio of the excitation band and the film's XRD pattern.

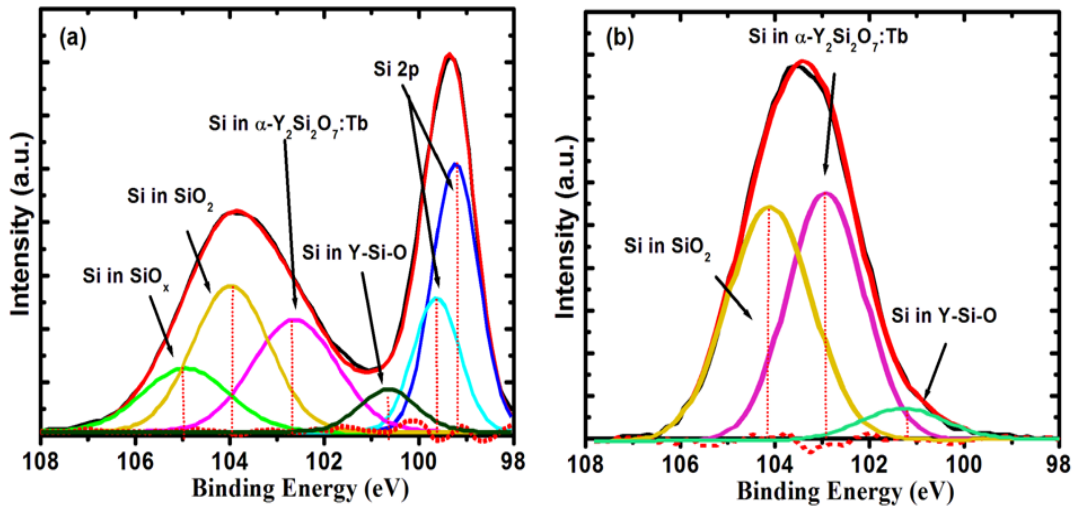


**Figure 7.10:** Deconvolution of selected Si (2p) signals of the film (a) annealed at 800 °C and (b) annealed at 1200 °C.

Table 7.5: Binding energies for Si 2p XPS peaks in  $Y_3(Al, Ga)_5O_{12}:Tb$  after heat treatment at 800 °C and 1200 °C.

Binding energies for Si 2p	Annealed at 800 °C peak (a)	Annealed at 1200 °C peak (b)
Possible component with possible data values from different references	Si-Si 2p <sub>1/2</sub> and 2p <sub>3/2</sub> at 99.2 and 99.6 eV [11, 20] $\alpha$ -Y <sub>2</sub> Si <sub>2</sub> O <sub>7</sub> :Tb at 102.7 eV SiO <sub>2</sub> at 103.9 eV [21] SiO <sub>x</sub> at 104.9 eV	Y Si O at 101.3 eV Y <sub>2</sub> Si <sub>2</sub> O <sub>7</sub> :Tb 102.8 eV SiO <sub>2</sub> at 104.1 eV [21]

---

## 7.4 Conclusion

The conversion of  $Y_3(Al, Ga)_5O_{12}:Tb$  thin film to  $\alpha$ -Y<sub>2</sub>SiO<sub>7</sub> : Tb<sup>3+</sup> thin film was observed when the films were annealed at temperatures higher than 800 °C. This conversion resulted in the change in the excitation band ratio of the PL and the trap positions. The crystal structures of the  $Y_3(Al, Ga)_5O_{12}:Tb$  films were changed at elevated temperature due to the reaction between the Y and O from  $Y_3(Al, Ga)_5O_{12}:Tb$  films and the Si substrate. A new compound,  $\alpha$ -Y<sub>2</sub>SiO<sub>7</sub> : Tb<sup>3+</sup>, different from the original material ( $Y_3(Al, Ga)_5O_{12}:Tb$ ), was formed and this was confirmed by XRD, the PL properties and XPS analysis.

## References

- [1] J. Y. Choe, D. Ravichandran, S. M. Blomquist, D.C. Morton, K. W. Kirchner, M. H. Ervin, U. Lee, Journal of Applied Physics Letters **78** (2001) 24.
- [2] Z. Nan-Fei, L. Yong-Xiang, Y. Xiao-Feng, Journal of Chinese Physics Let-

- ters **25** (2008) 703.
- [3] H. Kwak, S. Kim, H. Yoon, S. Park, H. Choi, *Journal of Electroceramics* **23** (2009) 397.
- [4] O. Katsutoshi, A. Tomohiko, K. Tsuneo, *Japanese Journal of Applied Physics* **29** (1990) 103.
- [5] H. Matsukiyo, H. Toyama, Y. Ueharab, H. Yamamotoc, *Journal of Luminescence* **229** (1997) 72.
- [6] Q. Li, F. Qiu, J. Zhang, X. Pu, X. Liu, W. Zhang, *Journal of Alloys and Compounds* **474** (2009) 441.
- [7] A. Yousif, H. C. Swart, O. M. Ntwaeaborwa, *Applied Surface Science* **258** (2012) 6495.
- [8] H. Yamamoto, H. Matsukiyo, *Journal of Luminescence* **48** (49) (1991) 43.
- [9] L. Yong, B. You, W. Zhao, W. Zhang, M. Yin, *Chinese Journal of Chemical Physics* **21** (2008) 376.
- [10] S. Y. Chiam, W. K. Chim, A. C. H. Huan, J. S. Pan, J. Zhang, *Journal of Applied Physics Letters* **88** (011904) (2005).
- [11] Y. C. Shin, D. H. Kong, W. C. Choi, T. G. Kim, *Journal of Korean Physical Society* **48** (2006) 1246.
- [12] Multipak Version 9, Physical Electronics, Inc., Chanhassen, USA, 2006-2010.
- [13] M. Marezio, J.P. Remeika, P.D. Dernier, *Acta Crystallographica* **24** (1968) 1670(ICSD-29248).

- [14] G.A. Hirata, O. A. Lopez, L. E. Shea, J. Y. Yi, T. Cheeks, J. McKittrick, J. Siqueiros, M. Avalos-Borja, A. Esparza, C. Falcony, *Journal of Vacuum Science and Technology A* **14** (1996) 1694.
- [15] F. Huang, L. Dong, Z. Fu, H. Wang, W. Wang, J. Y. Wang, *Ceramic Processing Research* **10** (2009) 807.
- [16] Y. Li, B. You, W. Zhao, W. Zhang, M. Yin, *Chinese Journal of Chemical Physics* **21** (2008) 376.
- [17] H. C. Swart, E. Coetzee, J. J. Terblans, O. M. Ntwaeaborwa, P. D. Nsimama, F. B. Dejene, J. J. Dolo, *Applied Physics A: Materials Science and Processing* **101** (4) (2010) 633.
- [18] V. Pagonis, G. Kitis, C. Furetta, *Numerical, Practical Exercises in Thermoluminescence*, Springer Science Business Media Inc., USA, 2006.
- [19] K. S. Chunga, H. S. Choea, J. I. Leeb, J. L. Kimb, *Radiation Measurements* **42** (2007) 731.
- [20] J. J. Chambers, G. N. Parsons, *Journal of Applied Physics* **90** (2001) 918.
- [21] O. M. Ntwaeaborwa, G. H. Mhlongo, S. S. Pitale, M. S. Dhlamini, R. E. Kroon, H. C. Swart, Cathodoluminescent Properties of  $\text{SiO}_2:\text{Ce}^{3+}$ ,  $\text{Tb}^{3+}$ ,  $\text{SiO}_2:\text{Ce}^{3+},\text{Pr}^{3+}$  and  $\text{SiO}_2:\text{PbS}$ , in: Naoki Yamamoto (Ed.), *Cathodoluminescence*, Intech Publishers, 2012, pp. 233-252, ISBN: 979-953-307-319-3 (Chapter 9).

# Chapter 8

## Effect of different annealing temperatures on the optical properties of $Y_3(\text{Al}, \text{Ga})_5\text{O}_{12}:\text{Tb}$

### 8.1 Introduction

Luminescent films play an important role in high resolution display devices. Yttrium aluminium garnet ( $Y_3\text{Al}_5\text{O}_{12}$ ) or YAG shows great luminescent properties when doped with rare-earth elements [3, 4]. Furthermore, the replacement of a portion of the Al with Ga in the matrix of  $Y_3(\text{Al}, \text{Ga})_5\text{O}_{12}:\text{Tb}$  phosphor shows very good CL stability during prolonged electron bombardment [5]. The thermal annealing process is widely used to improve the crystal quality and to decrease structural defects in materials. During the annealing process, dislocations, and other structural defects move in the material and adsorption/decomposition may occur at the surface, thus the structure and the stoichiometric ratio of the material will change [6]. As reported in the literature [1], the interdiffusion of atomic species between the Si substrate and  $Y_3(\text{Al}, \text{Ga})_5\text{O}_{12}:\text{Tb}$  thin films were observed for post annealing at higher temperatures, which is responsible for the conversion of the  $Y_3(\text{Al}, \text{Ga})_5\text{O}_{12}:\text{Tb}$  film to a  $Y_2\text{Si}_2\text{O}_7:\text{Tb}$  film. The change in the films structure has an impact on the films optical properties. Yousif et al. [2] reported that annealing improved the PL intensities as well as the crystallinity of the  $Y_3(\text{Al}, \text{Ga})_5\text{O}_{12}:\text{Tb}$  films. The interdiffusion of Si with the phosphor layer is, however, problematic and a diffusion barrier layer, such as  $\text{SiO}_2$ , between the phosphor and the Si is needed. The effect of annealing on the structural and optical properties of PLD  $Y_3(\text{Al}, \text{Ga})_5\text{O}_{12}:\text{Tb}$  thin films, deposited on  $\text{SiO}_2/\text{Si}(100)$  substrates is presented. Structure and surface morphology of the films were studied by XRD, SEM, AFM and NanoSAM. The PL emission as function of annealing temperature was also recorded.

## 8.2 Experimental

The Si (100) wafers used as substrates were first cleaned as described elsewhere [2, 5]. Then SiO<sub>2</sub> were prepared by thermal oxidation on cleaned Si (100) wafers by wet oxygen bubbled through water at 80 °C for 1 h, at a temperature of 1000 °C. The PLD technique was used for the preparation of the films. The deposition chamber was evacuated to a base pressure of  $1.17 \times 10^{-5}$  mbar and then backfilled with O<sub>2</sub> to a pressure of  $5.3 \times 10^{-2}$  mbar. The Y<sub>3</sub>(Al, Ga)<sub>5</sub>O<sub>12</sub>:Tb (obtained from Phosphor technology, the Tb concentration value is not available at this stage, a full characterization and electron stability test of the powder is presented in ref [5]) target was ablated in the O<sub>2</sub> working atmosphere using a 266 nm Nd:YAG pulsed laser. The laser frequency, number of pulses, fluency, substrate temperature and target-to-substrate distance were fixed at 10 Hz, 20000, 0.767 J/cm<sup>2</sup>, 300 °C and 4.5 cm, respectively. The deposited thin films were annealed for 3 hrs at 800 °C, 900 °C and 1000 °C in air. XRD analysis was carried out using a Bruker AXS D8ADVANCE X-ray diffractometer. The PL properties of the films were measured using a Carry eclipse spectrophotometer at room temperature. The surface topography was examined using a Shimadzu SPM-9600 AFM. The chemical composition analysis was carried out using a PHI 700 NanoSAM with a 25 keV, 10 nA electron beam.

## 8.3 Result and discussion

The elemental distribution of Si (red), Ga (green) and Al (blue) are represented by the 2D NanoSAM elemental mapping captured with a 10 μm field of view in Figure 8.1, for the as deposited, 800 °C , 900 °C and 1000 °C annealed films, respectively. The elemental mapping of the deposited film shows a homogeneous distribution of the Ga and Al elements, with an exception of some Al enriched rounded particles of different sizes which seem to be formed from local melting

and ejected O-Al from the target to the substrate which are typically found in laser ablation experiments [7]. Annealing caused stress in the films and aggravated cracking occurred as presented in the images of the annealed samples in Figures 8.1. This type of behavior was not detected for the films deposited directly on the Si (100) without SiO<sub>2</sub> even after annealing [1]. Nevertheless, annealing at 800 °C and above caused diffusion of the different elements and a slight enrichment of Ga on the film surface was measured. This phenomena was also reported by Yousif et al. [2]. Areas with Si enrichment were obtained on all the annealed samples. The SiO<sub>2</sub> therefore did not completely stop the interdiffusion between the substrate and phosphor thin films. The XPS depth profiles for the as deposited and annealed thin films are shown in Figures 8.2 (a, b, c and d). In all the depth profiles, the main elements present in Y<sub>3</sub>(Al, Ga)<sub>5</sub>O<sub>12</sub>:Tb, i.e. Y, Al, Ga, and O were detected. It is clear from the depth profiles that the thicknesses of the annealed films and the concentrations of Ga and Si in the 900 and 1000 °C, Figures 8.2 (c) and (d), were different. The difference in the film thickness can be attributed to the high degree of diffusion of the elements present in the phosphor material and also due to interdiffusion of the substrate and the phosphor material, leaving uneven films that varied in thickness and concentration as also pointed out in the Si enriched areas (red) in Figure 8.1. The Si enriched areas were thinner compared with the other areas. In order to monitor the secondary Y<sub>2</sub>Si<sub>2</sub>O<sub>7</sub> impurity phase that develop between the thin Y<sub>3</sub>(Al, Ga)<sub>5</sub>O<sub>12</sub>:Tb film and the SiO<sub>2</sub>/Si substrate that was annealed at 900 °C, the high resolution XPS O 1s and Y 3d peaks are also presented as three dimensional depth profiles in Figures 8.3. The depth profiles show the change in O and Y positions as function of depth. The 2s Si peak overlap with the Y 3d peak. A thin layer of the Y<sub>2</sub>Si<sub>2</sub>O<sub>7</sub> phase is clearly visible (especially in the O 1s 3 D profile) between the Y<sub>3</sub>(Al, Ga)<sub>5</sub>O<sub>12</sub>:Tb and SiO<sub>2</sub>/Si substrate. Figure 8.4 shows XRD patterns of the as deposited and annealed Y<sub>3</sub>(Al, Ga)<sub>5</sub>O<sub>12</sub>:Tb thin films at 800 °C , 900 °C and 1000 °C for 3 hours. A crystalline film with

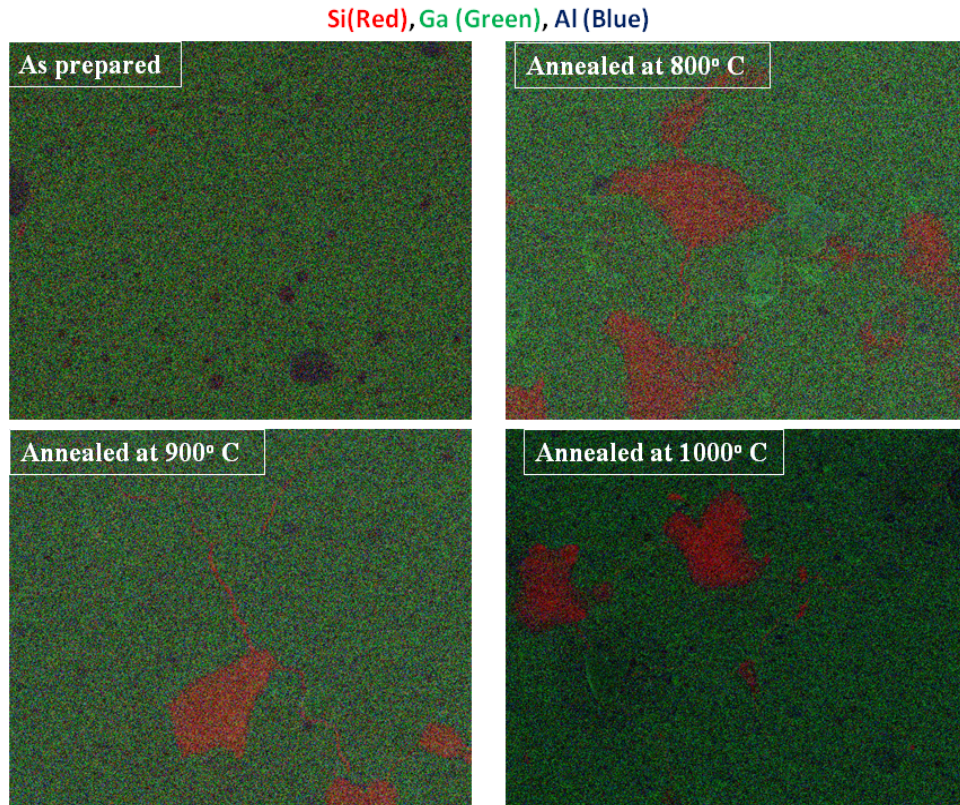


**Figure 8.1:** NanoSEM and SAM images for deposited and annealed films at 800 °C, 900 °C and 1000 °C of the combination of Si (red), Ga (green) and Al (blue) with 10  $\mu\text{m}$  field of view.

preferential growth in the (420) direction was observed for the as prepared film. Growth in the (400), (420) and (422) orientation occurred during annealing at 800 °C and continuing growing at higher annealing temperatures. The peaks are in agreement with the XRD pattern of the  $\text{Y}_3(\text{Al}, \text{Ga})_5\text{O}_{12}:\text{Tb}$  powder [5]. A secondary  $\gamma - \text{Y}_2\text{Si}_2\text{O}_7$  [8] or  $\alpha - \text{Y}_2\text{Si}_2\text{O}_7$  [9] impurity phase which is labeled with an asterisk (\*) in the spectrum was also observed after annealing at 900 °C and 1000 °C. Figure 8.5(a-d) shows the AFM micrographs of the surface of the as deposited and annealed  $\text{Y}_3(\text{Al}, \text{Ga})_5\text{O}_{12}:\text{Tb}$  thin films. The regions evaluated shows that the surface layer was uniform and the substrate was well covered with particles. Except for some rounded bigger particles of different sizes which also

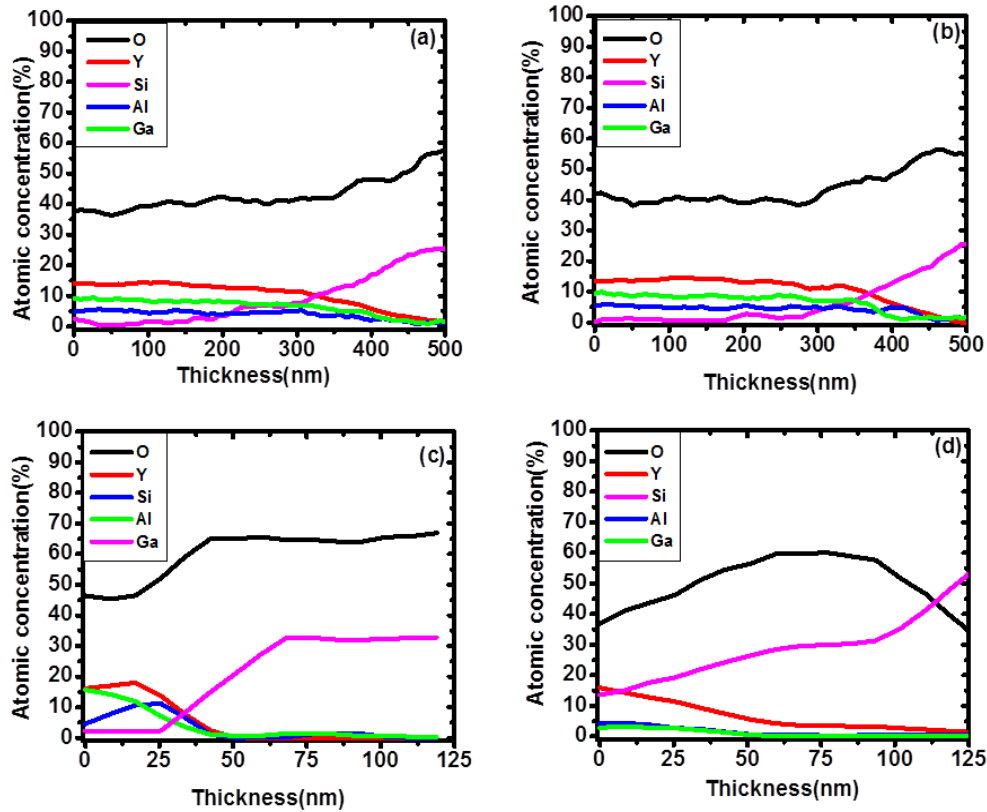


**Figure 8.2:** The depth profiles for the as deposited 800, 900 and 1000 °C annealed  $Y_3(Al, Ga)_5O_{12}:Tb$  films respectively.

seem to consist of smaller spherically grains, the as deposited films consist of a granular structure of spherical grains with various grain sizes, with root mean square (RMS) value of about 7 nm, Figure 8.5 (a). Annealing at 800 °C induced changes in the surface topography, which shows spherically homogeneous grain sizes with RMS of 3 nm as presented in Figure 8.5 (b), furthermore, the smaller spherically grains in the rounded particles seem to be coalesced. As reported by Hasnat and Podder [10], at higher annealing temperatures grains have higher energies than the individual atoms, so growing nuclei come into contact to form bigger grains, as presented in Figure 8.5 (c), with the RMS about 10 nm. The grains on the surface merge together so that the boundaries of the grains were not clear for the film annealed at 1000 °C which can be seen in Figure 8.5

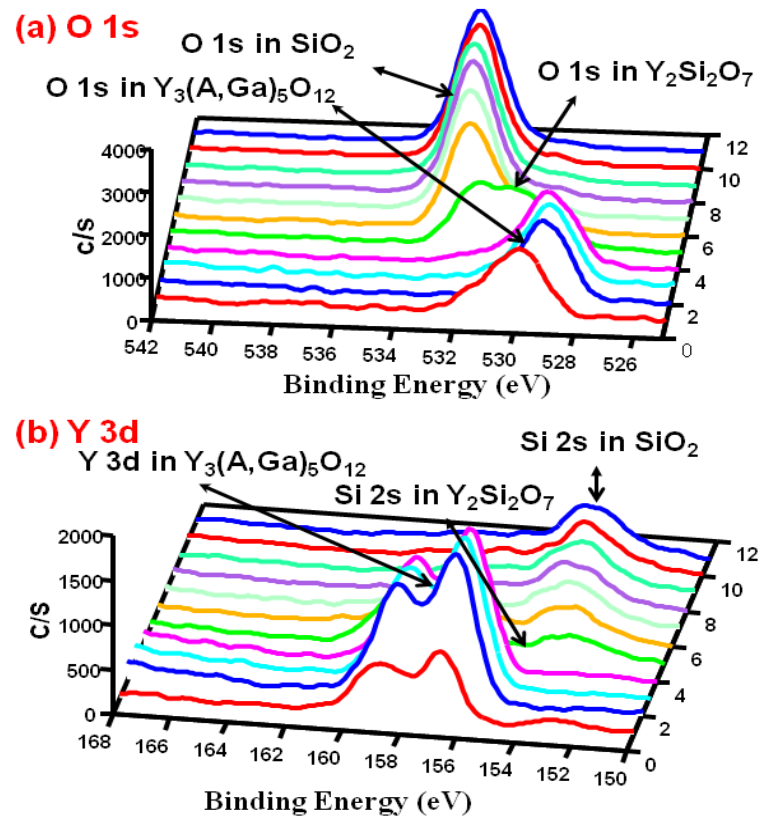


**Figure 8.3:** XPS depth profiles of selected O (1s) and Y(3d) signals of the films annealed at 900 °C.

(d), the RMS still about 10 nm. It can be conclude that, the higher annealing temperature provides more activation energy to atoms to grow larger grains as confirm with the AFM images leaving some areas with less covering material as confirmed with the SAM images. Moreover, annealing at 800 °C and 1200 °C, for the films grows on the Si (without  $\text{SiO}_2$ ) substrate [2], also induced changes in the surface topography in different ways. Spherical grains covered with a smoother layer confirmed by AES to be a Ga-O layer for the films annealed at 800 °C, Figure 8.5 (e) [2] and completely change in surface topography after annealing at 1200 °C (which confirmed to be  $\text{Y}_2\text{Si}_2\text{O}_7$ ) [1] as seen in Figure 8.5 (f).

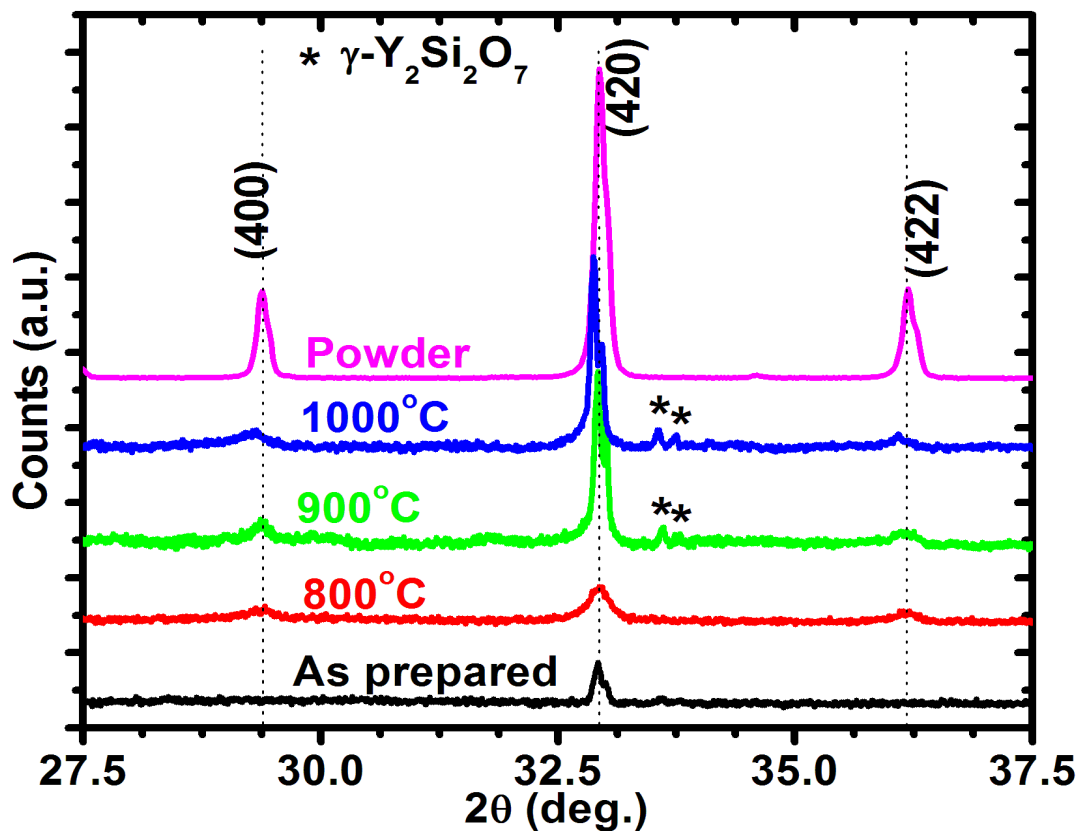
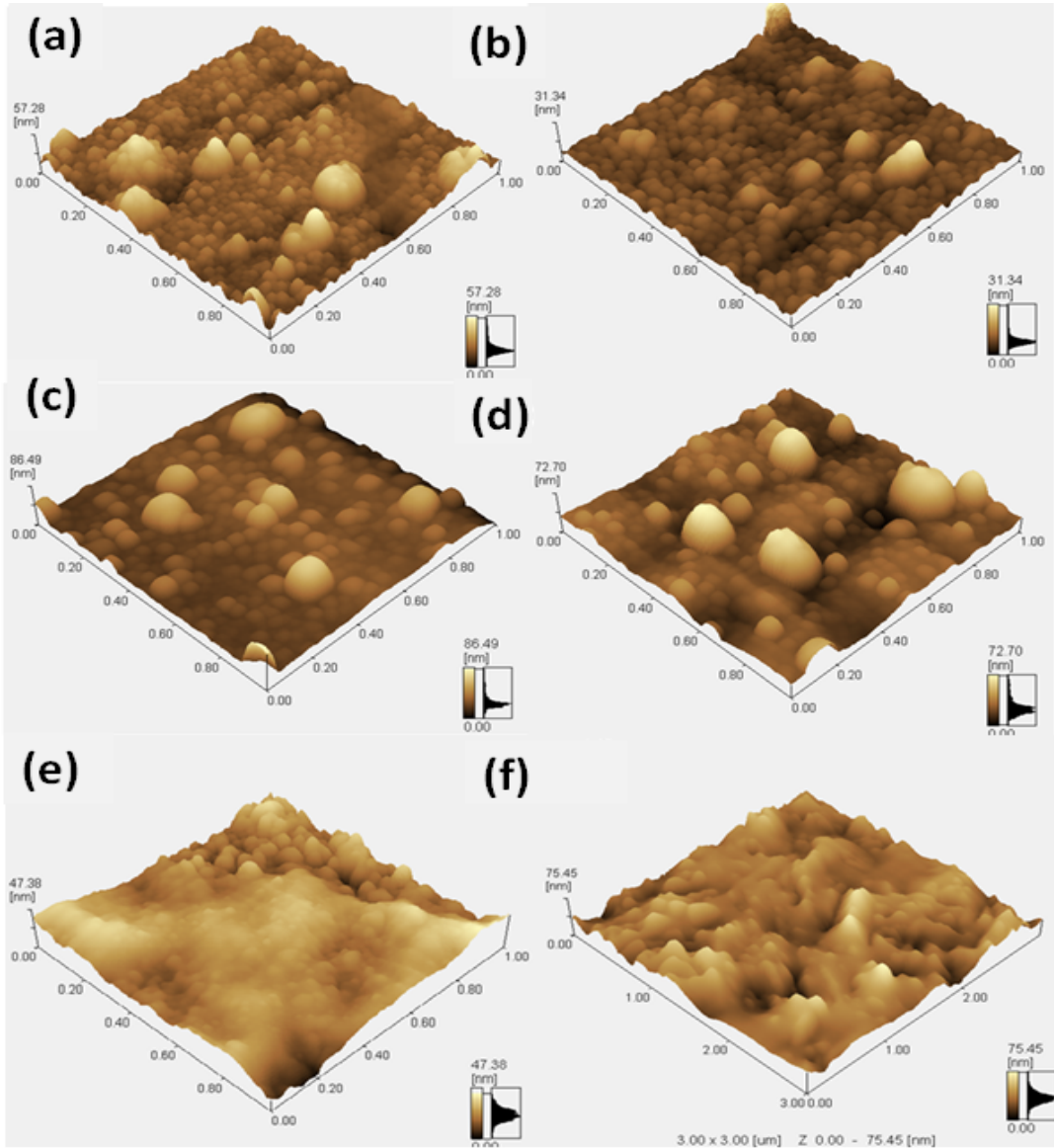
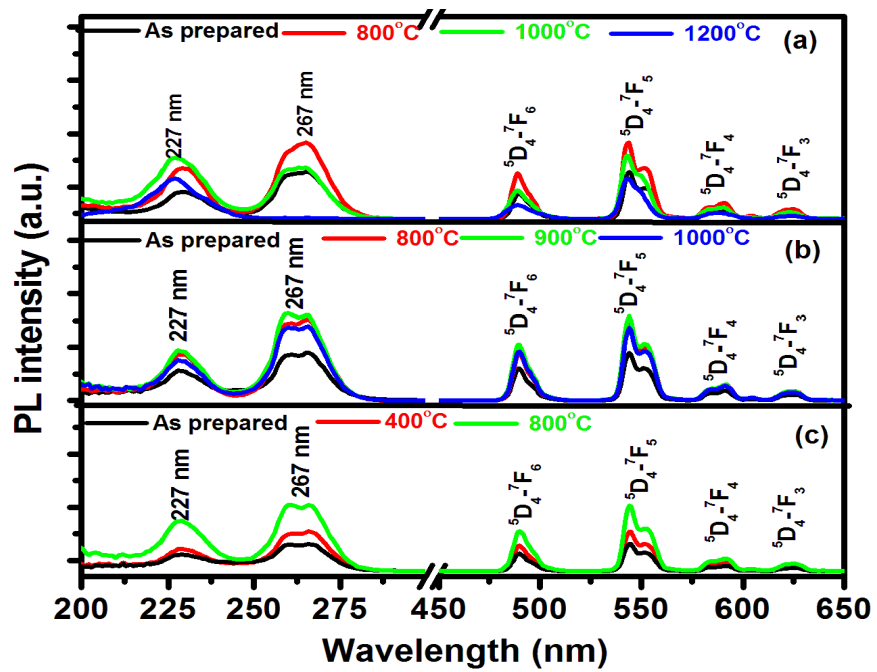


Figure 8.4: XRD spectra of  $\text{Y}_3(\text{Al, Ga})_5\text{O}_{12}:\text{Tb}$  phosphor powder, as prepared and annealed thin films.



**Figure 8.5:** AFM images of the surface of (a)  $Y_3(Al, Ga)_5O_{12}:Tb$  thin films on  $SiO_2/Si$  substrate, annealed for 3 hours, (a) as deposited and (b), (c) and (d) after annealed at 800 °C, 900 °C and 1000 °C respectively. (e) and (f) images for the same materials on Si substrate annealed for 1 at 800 °C and the others at 1200 °C for 3 hrs respectively.

Figures 8.6(a-c) shows the PL emission and excitation spectra for annealed films on Si and SiO<sub>2</sub>/Si substrates after different annealing conditions as indicated. The emission lines are attributed to the well-known  $^5D_4 \rightarrow ^7F_J$  ( $J = 6, 5, 4, 3$ ) transitions of the Tb ions [1, 2, 4, 7], which present similar characteristics for all annealing temperatures. This is owing to the fact that, the lanthanide elements (rare earth) have a partially filled inner  $4f^n$  shell surrounded by completely filled outer  $5s^2$  and  $5p^6$  orbitals which prevent the sharp  $4f-4f$  line emissions of the Tb<sup>3+</sup> from the anionic environment. Therefore they are relatively independent of the host material and are determined by the energy transition between the  $4f$  states only. On the other hand, the energy of the  $5d$  levels depends strongly on the nature of the host due to a greater radial extension of the  $5d$  orbital, which may be used to explain the significant changes in the excitation bands observed in Figure 8.6(b). The film that was deposited on the Si substrate and annealed at 1200 °C for 3 h, shows a significant change in the excitation bands. Before annealing, the excitation band at 267 nm was more intense than the 227 nm and the ratios of the maximum intensities of the 267 to 227 nm excitations were 1.7, 1.5, 0.8 and 0.03 for unannealed and after annealing at 800 °C, 1000 °C and 1200 °C respectively. After annealing the excitation band at 227 nm become more dominate, which indicated that, the emitting centers of the Tb<sup>3+</sup> were in a different environment as was confirmed to be a Y<sub>2</sub>Si<sub>2</sub>O<sub>7</sub>:Tb phosphor [1]. The film deposited on the Si substrate, and annealed at 800 °C for 1 h, start to follow the same trend, Figure 8.6(c). Although there was a Y<sub>2</sub>Si<sub>2</sub>O<sub>7</sub> impurity phase sandwich layer between the SiO<sub>2</sub>/Si substrate and the thin film only a slight change in the ratio of the 267 to 227 nm excitations bands was observed for the films that were deposited on the SiO<sub>2</sub>/Si substrate and annealed for 3 hours. A summary of the relative ratios and maximum intensities for the films are presented in Figures 8.6 (d) and (e). The maximum PL intensity of the films may increased with an increasing number of pulses due to a thicker deposited layer at larger number of pulses as observed by Dlammini et al. [11].



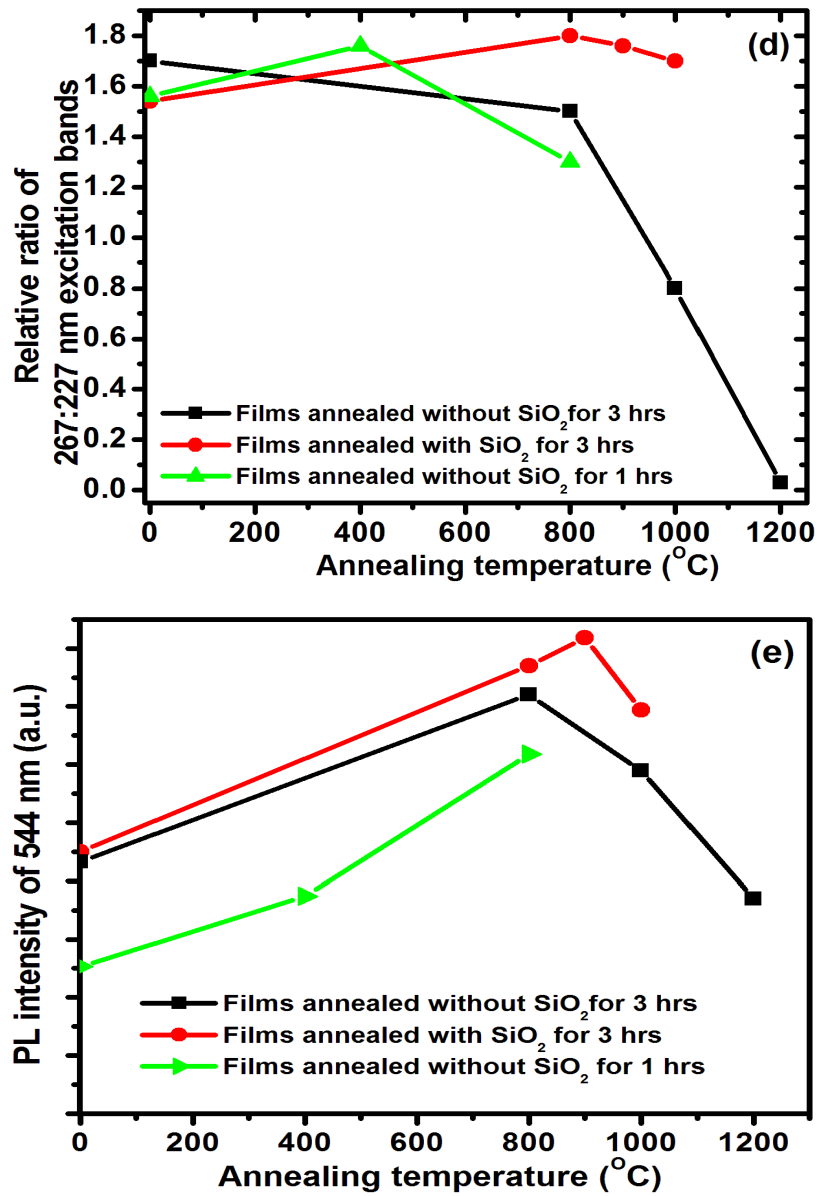


**Figure 8.6:** PL excitation and emission spectra of as prepared and annealed thin films for the films prepared on (a) SiO<sub>2</sub>/Si, (b) and (c) on Si substrates. The films in (a) and (b) annealed for three hours while the film in (c) annealed for 1 hour. (d) and (e) show the relative ratio of the intensities of the 267:227 nm excitation bands and the relative emission ratio intensities as a function of the different annealing temperatures, respectively.

## 8.4 Conclusion

The elemental mapping showed that the annealing process caused regions of Si enrichment in the films. No significant change in the PL excitation bands at 267 nm and 227 nm were measured for the SiO<sub>2</sub>/Si substrate. A thin impurity phase was sandwiched between the SiO<sub>2</sub>/Si substrate and the thin film. Diffusion of material on the SiO<sub>2</sub> lead to an in-homogeneous film in thickness and composition. It is also clear that SiO<sub>2</sub> buffer layer did not completely prevent diffusion, and that the intended YAG-like phase was partly destroyed. In the case of the Si substrate, without the SiO<sub>2</sub>, the thin films were completely converted to a different phase with the consequent change in excitation peaks.

## References

- [1] A. Yousif, H. C. Swart, O. M. Ntwaeaborwa, E. Coetsee, *Applied Surface Science* **270** (2013) 331.
- [2] A. Yousif, H. C. Swart, O. M. Ntwaeaborwa, *Journal of Luminescence* **143** (2013) 201.
- [3] O. Katsutoshi, A. Tomohiko, K. Tsuneo, *Japanese Journal of Applied Physics* **29** (1990) 103.
- [4] H. Matsukiyo, H. Toyama, Y. Ueharab, H. Yamamotoc, *Journal of Luminescence* **229** (1997) 72.
- [5] A. Yousif, H. C. Swart, O. M. Ntwaeaborwa, *Applied Surface Science* **258** (2012) 6495.
- [6] L. P. Peng, L. Fang, X. F. Yang, Y. J. Li, Q.L. Huang, F. Wu, C.Y. Kong, *Journal of Alloys and Compounds* **484** (2009) 575.

- [7] G. A. Hirata, O. A. Lopez, L. E. Shea, J. Y. Yi, T. Cheeks, J. McKittrick, J. Siqueiros, M. Avalos-Borja, A. Esparza, C. Falcony, *Journal of Vacuum Science and Technology A* **14** (1996) 1694.
- [8] Z. Sun, Y. Zhou, M. Li, *Journal of Materials Research* **21** (2006) 6.
- [9] D. Hreniak, P. Gluchowski, W. Strek, M. Bettinelli, A. Kozlowski, M. Kozlowski, *Journal of Materials Science-Poland* **24** (2006) 2.
- [10] A. Hasnat, J. Podder, *Advances in Materials Physics and Chemistry* **2** (2012) 226.
- [11] S. T. S. Dlamini, H. C. Swart, O. M. Ntwaeaborwa, *Physica B: Physics of Condensed Matter*, in press.

## Chapter 9

### Effect of annealing on the structure of $Y_3(\text{Al}, \text{Ga})_5\text{O}_{12}:\text{Tb}$ thin film grown by PLD

#### 9.1 Introduction

Luminescent materials have received a worldwide technological interest for a broad range of everyday applications. Among them, Yttrium aluminium garnet material (YAG) activated with  $\text{Tb}^{3+}$  is one of the most heavy-duty phosphors which are widely used in displays applications [1–3]. The brightness and saturation characteristics were improved by the replacement of a portion of Al with Ga in the YAG host to improve the saturation characteristics at higher electron beam density excitations [4, 5]. On the other hand, this partial replacement of Al with Ga slightly increased the deterioration of luminescence efficiency under electron bombardment [1]. However,  $Y_3(\text{Al}, \text{Ga})_5\text{O}_{12}:\text{Tb}$  phosphor powder, showed very good cathodoluminescent (CL) stability, during prolonged electron bombardment [2]. Most phosphor materials consist of multi-components and their luminescence efficiency is largely affected by the right stoichiometry and growth mode. One of the most important things in the deposition of a phosphor thin film is the stoichiometric transfer of target material to the substrate [6]. It is well known that the PLD technique can produce a wide variety of complex compounds with controlled composition and properties. In this study, PLD  $Y_3(\text{Al}, \text{Ga})_5\text{O}_{12}:\text{Tb}$  thin films were grown with a set of fixed processing conditions. Thermal heating was used to improve the crystal quality and to decrease structural defects in the films. It is well known that, during the annealing process, dislocations, and other structural defects move in the material and adsorption/decomposition may occur at the surface, thus the structure and the stoichiometric ratio of the material may change [6]. As reported in the lit-

erature [3], the interdiffusion of atomic species between the Si substrate and  $Y_3(Al, Ga)_5O_{12}:Tb$  thin films were observed for post annealing at higher temperatures, which has an impact on the films optical properties. Yousif et. al. [7] reported that annealing improved the PL intensities as well as the crystallinity of the  $Y_3(Al, Ga)_5O_{12}:Tb$  films, but changes in the surface topography was observed after the annealing process, which showed spherically grains covered with inhomogeneous distribution of Ga on the surface relative to the distribution of the deposited film. Another study on the annealing effect of the  $Y_3(Al, Ga)_5O_{12}:Tb$  film [8], showed that stress and aggravated cracking occurred during annealing, which left regions enriched with Si after annealing at the higher temperatures. In this work, we report on the effect of different annealing times on the optical, morphological and the structural properties of the  $Y_3(Al, Ga)_5O_{12}:Tb$  film annealed at 800 °C.

## 9.2 Experimental

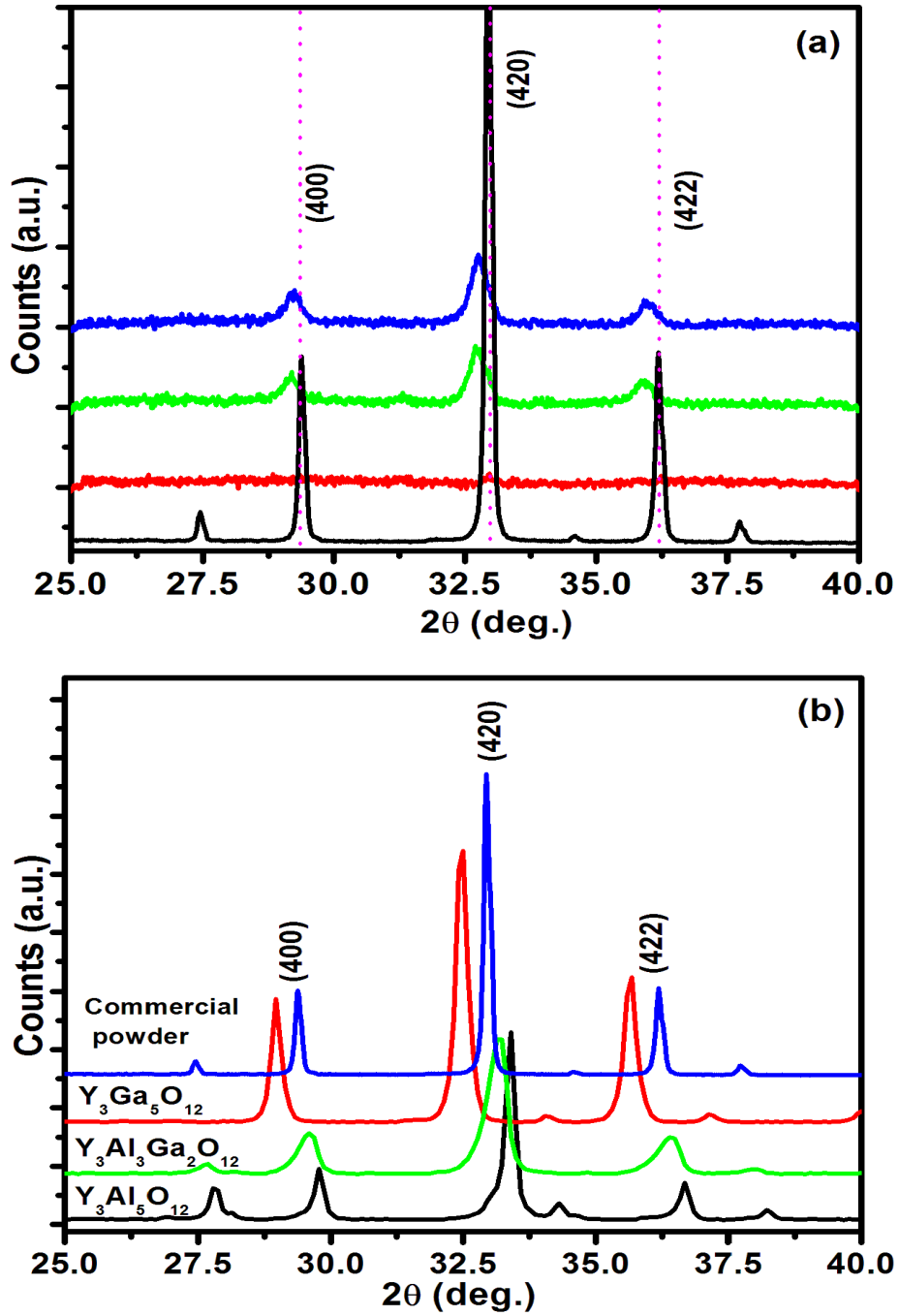
The Si (100) wafers used as substrates were first cleaned as described elsewhere [3, 7]. The PLD technique was used for the preparation of the films. The deposition chamber was evacuated to a base pressure of  $1.3 \times 10^{-5}$  mbar and then backfilled with  $O_2$  to a pressure of  $5.3 \times 10^{-2}$  mbar. The  $Y_3(Al, Ga)_5O_{12}:Tb$  target was ablated in the  $O_2$  working atmosphere using a 266 nm Nd:YAG pulsed laser. The laser frequency, number of pulses fluency, substrate temperature and target-to-substrate distance were fixed at 10 Hz, 20000,  $0.767 \text{ J/cm}^2$ , 300 °C and 4.5 cm, respectively. Some of the deposited thin films were annealed for 2 and 3 hrs at 800 °C in air.  $Y_3(Al, Ga)_5O_{12}:Tb$  was also synthesized by using an urea-nitrate solution combustion synthesis technique.  $Y(NO_3)_3 \cdot 4H_2O$ ,  $CON_2H_4$  and  $Ga(NO_3)_3 \cdot 5H_2O$  were used as starting materials, which were dissolved in diluted water during stirring and heating to obtain a mixing aqueous homogenous precursor solution. The solution was placed in a furnace preheated at 500 °C.

After the combustion process was completed, the obtained solid precursors were then ground and fired at 900 °C for 2 h in air to produce the final samples. X-ray diffraction (XRD) analysis was carried out using a Bruker AXS D8ADVANCE X-ray diffractometer. The PL properties of the films were measured using a Carry eclipse spectrophotometer at room temperature. The surface topography was examined using a Shimadzu SPM-9600 atomic force microscope (AFM).

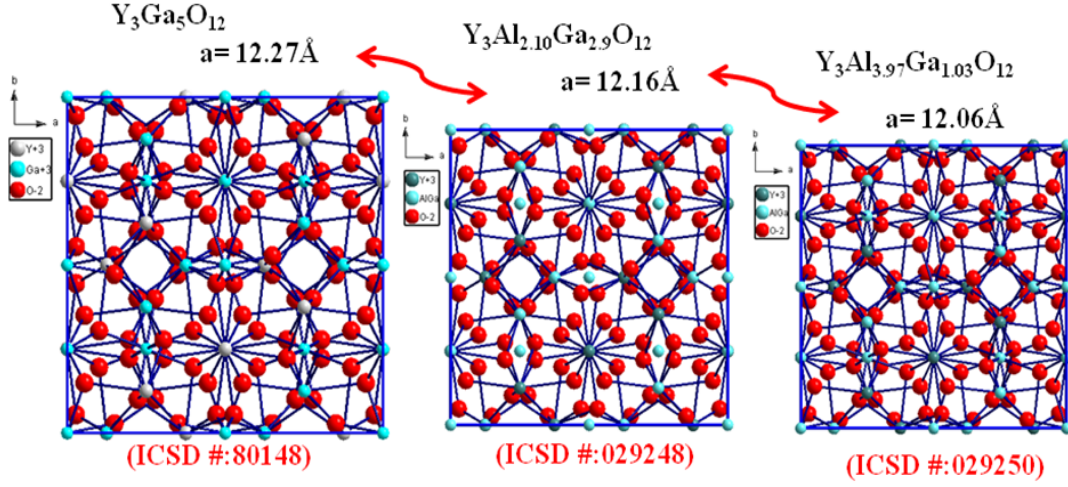
### 9.3 Results and discussion

Figure 9.1(a) shows the XRD patterns of the powder, the as deposited and the annealed  $Y_3(Al, Ga)_5O_{12}:Tb$  thin films. A small (420) diffraction peak at the same position as the powder was observed for the as deposited film. The annealed films shows three diffraction peaks at 29.3°, 32.7 °, and 35.9° which correspond to the (400), (420) and (422) crystalline planes [2], respectively. Furthermore, an increase in the annealing time resulted in an increase in the intensity of the (420) diffraction peak as shown in Figure 9.1 (a), which clearly indicates that the crystallinity of the  $Y_3(Al, Ga)_5O_{12}:Tb$  film was enhanced with an increase in the annealing time. The estimated average crystallite size of the  $Y_3(Al, Ga)_5O_{12} : Tb$  was obtained by using Scherrers equation [9] and was found to be  $\sim 23$  nm and  $\sim 25$  nm for the 2 and 3 hrs annealed films, respectively. Furthermore, a slight shift in the peak position to a lower diffraction angle was observed for the annealed films compared with the  $Y_3(Al, Ga)_5O_{12}:Tb$  commercial powder. Figure 9.1 (b) represent the XRD patterns for the commercial and synthesised  $Y_3(Al, Ga)_5O_{12}:Tb$  powder with different Ga concentrations, which show a shift of the peaks to lower diffraction angles with an increase in the Ga concentration. This is due to the fact that the ionic radius of  $Ga^{3+}$  (0.062 nm) is larger than the ionic radius of  $Al^{3+}$  (0.053 nm) [10]. Therefore with an increase in Ga concentration a change in the host lattice is expected. Figure 9.2 demonstrates the effect of the Ga concentration on the lattice parameter, showing the

host site with  $a=12.27 \text{ \AA}$  ,  $12.16 \text{ \AA}$  and  $12.06 \text{ \AA}$  for  $\text{Y}_3\text{Ga}_5\text{O}_{12}$  [11],  $\text{Y}_3\text{Al}_3\text{Ga}_2\text{O}_{12}$  [12] and  $\text{Y}_3\text{Al}_{3.97}\text{Ga}_{1.03}\text{O}_{12}$  [12] respectively. As a result of an increase in the Ga concentration, the inter-planar spacing will increase and a shift towards lower angles in the diffraction peak will be observed as pointed out by Braggs law. It can be concluded that, the shift towards the lower diffraction angles in the XRD patterns of the annealed films probably indicating that the films are enrichment with Ga compared with the as prepared film. The NanoSAM elemental mapping of films showed some inhomogeneous distribution of Ga on the surface of the deposited films, indicating that some areas of the films were enriched with Ga [7]. Ga with a very low melting point of  $29.76 \text{ }^\circ\text{C}$ , maybe transferred as agglomerated clusters during the PLD process and with annealing treatment, start to interact with the rest of materials to form structures that are enrichment with Ga.



**Figure 9.1:** (a) XRD patterns of the  $Y_3(\text{Al}, \text{Ga})_5\text{O}_{12}:\text{Tb}$  phosphor powder, and  $Y_3(\text{Al}, \text{Ga})_5\text{O}_{12}:\text{Tb}$  films as prepared and annealed at 800 °C. (b) XRD patterns of the commercial and prepared  $Y_3(\text{Al}, \text{Ga})_5\text{O}_{12}:\text{Tb}$  powder, showing the change in the peak position with different Ga concentrations.



**Figure 9.2:** Change in lattice parameter of the garnet crystal structure with different Ga concentrations.

Figure 9.3 (a-c) shows the AFM micrographs of the surface of the as deposited and annealed  $Y_3(\text{Al}, \text{Ga})_5\text{O}_{12}:\text{Tb}$  thin films. The regions evaluated show that the surface layer was uniform and the substrate was well covered with particles. The as deposited films consist of a granular structure of grains with various grain sizes. Annealing at 800 °C for 2 and 3 hrs induced changes in the root mean square (RMS) roughness and the surface topography. The RMS changed from 16 nm to 21 and 30 nm respectively. The surface topography shows larger grain sizes compared with the as prepared film, due the fact that, grain growth takes place by diffusion when the temperature is high enough and or the heat treatment time is long enough [13]. Figure 9.5 (a) shows the excitation and emission spectra, for the as prepared  $\text{Tb}^{3+}$  in  $Y_3\text{Al}_x\text{Ga}_y\text{O}_{12}$  host with different Ga and Al concentration. The emission lines were obtained for the excitation wavelength of 260, 267 and 272 nm for  $Y_3\text{Ga}_5\text{O}_{12}:\text{Tb}$ ,  $Y_3\text{Al}_3\text{Ga}_2\text{O}_{12}:\text{Tb}$  and  $Y_3\text{Al}_5\text{O}_{12}:\text{Tb}$  respectively. Four main PL bands for both green and blue emission are clearly resolved which are associated with the f-f internal orbital transitions of  $\text{Tb}^{3+}$  ions. They are attributed to the well-known  $(^5\text{D}_4 \rightarrow ^7\text{F}_J)(J = 6, 5, 4, 3)$  and  $(^5\text{D}_3 \rightarrow ^7\text{F}_J)(J = 6, 5, 4, 3)$  transitions of the  $\text{Tb}^{3+}$  ions [2, 3], which present

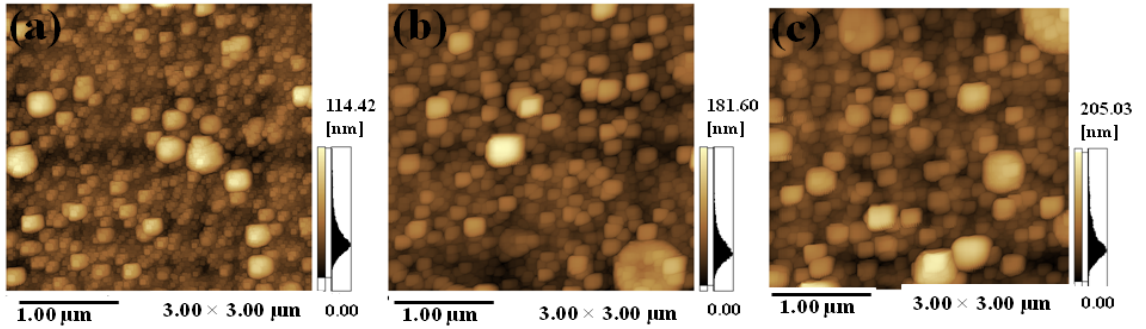


**Figure 9.3:** AFM images of the surface of the  $Y_3(\text{Al}, \text{Ga})_5\text{O}_{12}:\text{Tb}$  films (a) as prepared and annealed at  $800\text{ }^\circ\text{C}$  for (b) 2 hrs and (c) 3 hrs.

similar characteristics for the Tb in  $Y_3\text{Al}_x\text{Ga}_y\text{O}_{12}$  with different Al and Ga concentration except the increase in the intensities with an increase in the Ga concentration up to an optimum amount and then decreased with a further increase in the Ga concentration. This is due to the fact that, the lanthanide elements (rare earth) have a partially filled inner  $4f^n$  shell surrounded by completely filled outer  $5s^2$  and  $5p^6$  orbitals which shielded the sharp  $4f-4f$  line emissions of the  $\text{Tb}^{3+}$  from the anionic environment. Therefore they are relatively independent of the host material and are determined by the energy transition between the  $4f$  states only. On the other hand, the energy of the  $5d$  levels depends strongly on the nature of the host due to a greater radial extension of the  $5d$  orbital which can be seen in the excitation bands of as prepared powder with different Al and Ga concentrations. Mayolet et al. [14] studied the  $4f^75d$  configuration in  $Y_3\text{Al}_x\text{Ga}_y\text{O}_{12}:\text{Tb}$  and they concluded that there are five excitation band energies ( $E_1, E_2, E_3, E_4$  and  $E_5$ ) which clearly depend strongly on different concentrations of Ga. Figures 5(b-d) are the excitation bands changes for different concentrations of Ga, as redrawn from Ref. [14]. Their results may be summarized as follows:

1. For a high Al composition: the  $E_1, E_2, E_3$  and  $E_4$ , excitation bands, correspond to the excitation of the  $4f^75d$  states of  $\text{Tb}^{3+}$  whereas,  $E_5$  is

hidden by the inter-band transition  $E_g$  in the host.

- For a high Ga composition:  $E_1, E_2, E_{3,4}$  ( $E_3, E_4$  collapse) and  $E_5$  (shoulder) correspond to the excitation of a  $4f^8 \rightarrow 4f^7 5d$  transition of  $Tb^{3+}$  ions.

If the peak positions, as determined from the excitation spectra, are known for the different excitation bands, it may be used to explain the appearance of the new excitation band at 200 nm for the annealed films compared to as prepared film in Figure 9.5 (a), as indication that the annealed films were rich with Ga. Figure 9.5 (e) shows the  $E_5$  excitation spectra of the  $Y_3Al_xGa_yO_{12}:Tb$  with different concentration of Ga as indicated, which clearly confirms the above statements.

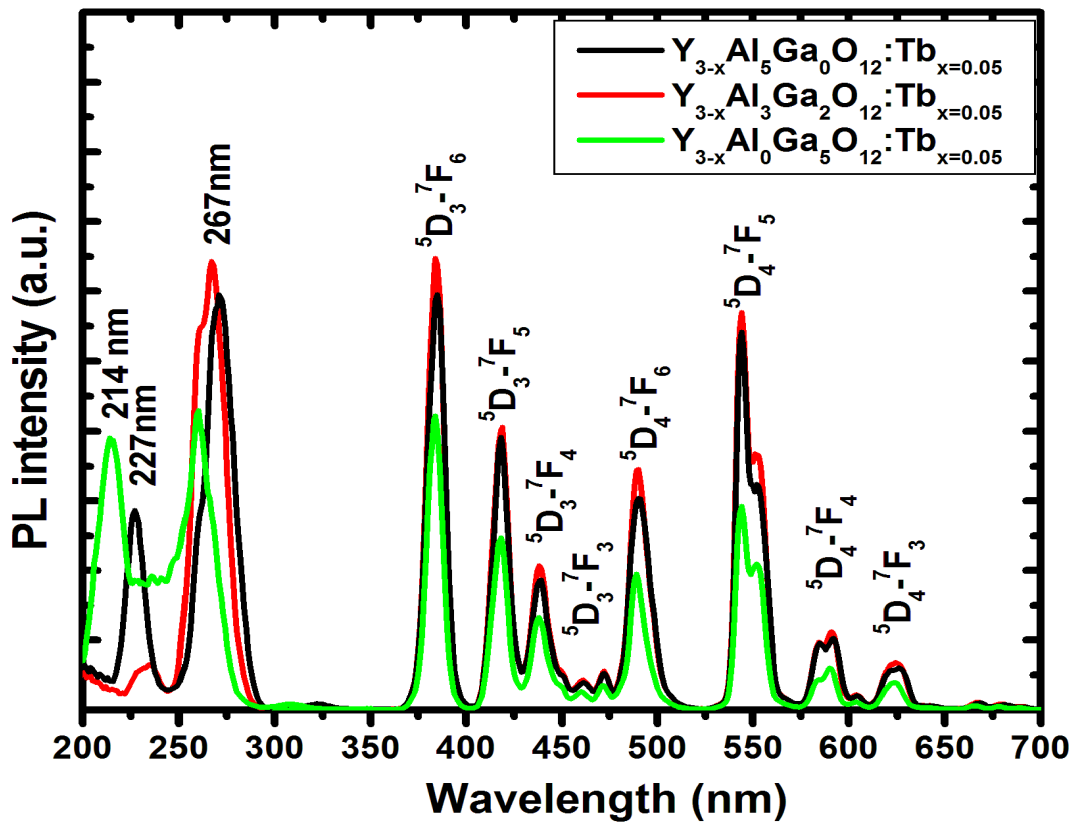
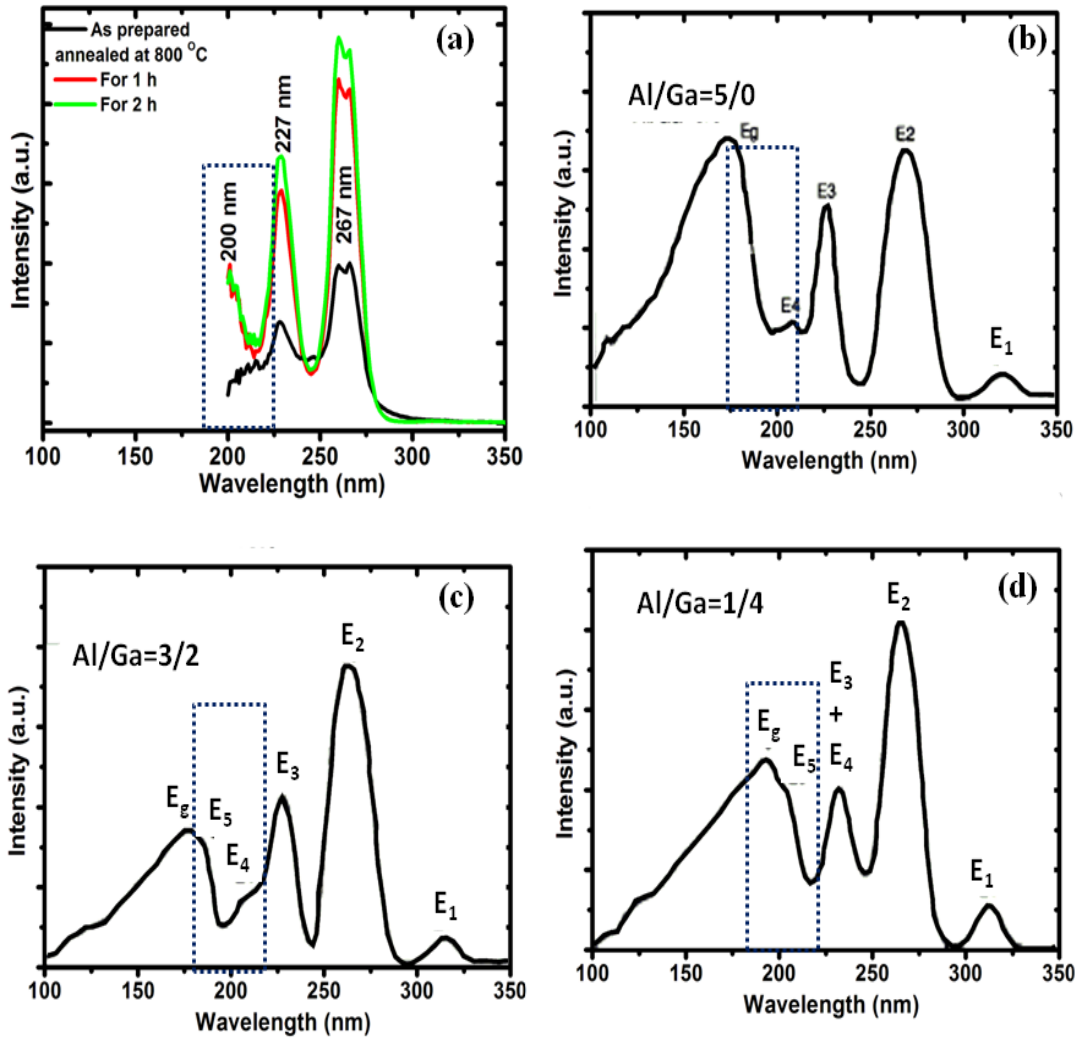


Figure 9.4: PL excitation and emission of the prepared  $Y_{3-x}Al_xGa_zO_{12}:Tb_{x=0.05}$  powder with different Ga concentration.



**Figure 9.5:** (a) PL excitation of the  $Y_3(Al,Ga)_5O_{12}:Tb$  films as prepared and annealed at 800 °C for 1 h and 2 h. (b)-(d) PL excitation of the  $Y_3(Al,Ga)_5O_{12}:Tb$  powder with different Ga concentration.

## 9.4 Conclusion

The influence of different annealing time on the optical and structure properties was observed as a new excitation band located at 200 nm and a shift in the diffraction peak position to lower diffraction angles, respectively. Both of them were attributed to an increase in the Ga concentration of the annealed films. An increase in the grain size with an increase in annealing time was also observed from the film morphology.

## References

- [1] O. Katsutoshi, A. Tomohiko, K. Tsuneo, Japanese Journal of Applied Physics **29** (1990) 103.
- [2] A. Yousif, H. C. Swart, O.M. Ntwaeaborwa, Applied Surface Science **258** (2012) 6495.
- [3] A. Yousif, H. C. Swart, O.M. Ntwaeaborwa, E. Coetsee, Applied Surface Science **270** (2013) 331.
- [4] H. Matsukiyo, H. Toyama, Y. Ueharab, H. Yamamoto, Journal of Luminescence **229** (1997) 72.
- [5] Q. Li, F. Qiu, J. Zhang, X. Pu, X. Liu, W. Zhang, Journal of Alloys and Compounds **474** (2009) 441.
- [6] L. P. Peng, L. Fang, X. F. Yang, Y. J. Li, Q. L. Huang, F. Wu, C. Y. Kong, Journal of Alloys and Compounds **484** (2009) 575.
- [7] A. Yousif, H. C. Swart, O. M. Ntwaeaborwa, Journal of Luminescence **143** (2013) 201.

- [8] A. Yousif, H. C. Swart, O. M. Ntwaeaborwa, *Physica B: Physics of Condensed Matter*, in press.
- [9] P. Y. Jia, J. Lin, X. M. Han, M. Yu, *Thin Solid Films* **483** (2005) 122.
- [10] R. Hansel, S. Allison, G. Walker, *Journal of Materials Research Society* **K06-06** (2008) 107.
- [11] A. Nakatsuka, Yoshiasa, S. Takeno, *Acta Crystallogr., Sec. B: Structural Science*, **51** (1995) 737.
- [12] M. Marezio, j. P. Remeika, P. D. Deernier, *Acta Crystallogr., Sec. B* **24** (1968) 1670.
- [13] F. X. Gil, D. Rodriguez, J. A. Planell, *Journal of Scripta Metallurgica et Materialia* **33** (1995) 1361.
- [14] A. Mayolet, W. Zhang, E. Simoni, J.C. Krupa, P. Martin, *Journal of Optical Materials* **4** (1995) 757.

# Chapter 10

## Summary and suggestions for future work

### 10.1 Summary of results and significant achievements

The results obtained in this project are summarised below:

- Surface states of  $Y_3(\text{Al}, \text{Ga})_5\text{O}_{12}:\text{Tb}$  phosphor under electron beam bombardment were investigated. The results reveal that this phosphor displayed good CL stability against prolonged electron bombardment which indicated that, it is a promising candidate for FEDs and other lighting applications.
- Thin films of  $Y_3(\text{Al}, \text{Ga})_5\text{O}_{12}:\text{Tb}$  were fabricated by PLD technique, these films are the first to date to be grown/deposited by PLD.
- The results of deposited films showed that the morphology, structure and the luminescence properties of the thin films were influenced by the working atmosphere (base pressure,  $\text{O}_2$ , Ar and  $\text{N}_2$ ) during the deposition procedure. The highest luminescent emission intensity was obtained from the film grown in the  $\text{O}_2$  working atmosphere. Deposition in vacuum gave a smoother surface with a roughness value around 6 nm and deposition in oxygen gave big agglomerated grains with defined grain boundaries and roughness of about 30 nm.
- The heat treatment at 400 °C and 800 °C for 2 hrs on the films deposited on Si(100) substrates, showed some inhomogeneous distribution of Ga on the surface indicating that, some areas of the annealed film were enriched with Ga compared with as deposited film. Moreover, the anneal-

ing led to a significant improvement in the luminescence properties of the  $Y_3(Al, Ga)_5O_{12}:Tb$  films as well as a change in the surface topography. The CL emission spectra were similar to the PL emission with a main peak at 544 nm. The decrease in CL intensity as function of prolonged electron irradiation was observed.

- The heat treatment at 800 °C, 1000 °C to 1200 °C for 3 hrs on the films that were deposited on Si (100) substrates, showed interdiffusion of atomic species between the Si(100) substrate and the  $Y_3(Al, Ga)_5O_{12}:Tb$  thin film which has an impact on the film's optical and structures properties. The  $Y_2Si_2O_7:Tb$  as identified by XRD, was formed as a result of the diffusion of Si atoms.
- The heat treatment at 800 °C, 900 °C and 1000 °C for 3 hrs for as deposited films that were grown on  $SiO_2/Si(100)$  substrates, showed that annealing caused stress in the films resulting in aggravated cracking. There were regions with enriched Si after annealing at the higher temperatures.

## 10.2 Suggestions for future work

1. In order to obtain the optimized parameters of  $Y_3(Al, Ga)_5O_{12}:Tb$  thin films, the influence of substrate temperature, the numbers of pulses, substrate to target distance and laser fluence need to be studied.
  2. A detailed study about micrometer and sub-micrometer sized particulates that are present on the surface and inside the  $Y_3(Al, Ga)_5O_{12}:Tb$  film should be investigated.
  3. Further studies can be done by investigating the CL stability of the synthesised  $Y_3(Al, Ga)_5O_{12}:Tb$  with different Ga concentrations during prolonged electron bombardment.
-

## Chapter 10

---

4. Thin films of  $Y_3(Al, Ga)_5O_{12}:Tb$  can be prepared by other preparation techniques and the effect of annealing can be investigated and compared with the results mentioned earlier.

## Publications

### Publications from this work

1. A. Yousif, H. C. Swart, O. M. Ntwaeaborwa, *Appl. Surf. Sci.* **258** (2012) 6495.
2. A. Yousif, H. C. Swart, O. M. Ntwaeaborwa, E. Coetsee. *Appl. Surf. Sci.*, **270** (2013) 331.
3. A. Yousif, H. C. Swart, O. M. Ntwaeaborwa, *J. Lumin.* **143** (2013) 201.
4. A. Yousif, H. C. Swart, O. M. Ntwaeaborwa, *J.Pysica B* **439** (2014) 77.

### Conference Proceedings

1. A. Yousif, H. C. Swart, O. M. Ntwaeaborwa, E. Coetsee, SAIP Conference, 09–13 July 2012 University of Pretoria, South Africa.
2. A. Yousif, H. C. Swart, O. M. Ntwaeaborwa, SAIP Conference, 8–12 July 2013 University of Zululand, South Africa.

### Presentation at conferences/Workshops

1. 4<sup>th</sup> African Laser center Student Workshop (09–13 November 2011 Zevenwacht Wine Estate, Stellenbosch, Western Cape, South Africa).
  2. 4<sup>th</sup> International Conference on Nano-science and Nanotechnology (01–04 April 2012 University of the Free State Bloemfontein).
  3. The 57<sup>th</sup> Annual Conference of the South Africa Institute of Physics (09–13 July 2012 University of Pretoria)
-

## Chapter 10

---

4. 5<sup>th</sup> African Laser Center Student Workshop (14–18 November 2012 UNAM, Windhoek, Namibia).
5. 5<sup>th</sup> South African Conference on Photonic Materials (29 April–3 May 2013 Kariega Game Reserve, South Africa).
6. The 58<sup>th</sup> Annual Conference of the South Africa Institute of Physics (8–12 July 2013 University of Zululand).
7. 6<sup>th</sup> African Laser Center Student Workshop (21–24 November 2013 Zevenwacht Wine Estate, Stellenbosch, Western Cape, South Africa).

## Goodfellow Award for chapter 4

I received the Goodfellow Award for the Most Outstanding Publication in a Scientific Journal from a PhD degree, chapter 4 in this project.

---

# Goodfellow

Materials for Scientific and Industrial Research and Manufacturing

### Dr A. Yousif receives Goodfellow Award in South Africa

Huntingdon, UK ... 15 August 2012 ... Dr A. Yousif (University of the Free State) recently received the Goodfellow Award for the Most Outstanding Publication in a Scientific Journal from a PhD degree\*. This award is the most prestigious in the field of Condensed Matter Physics/Materials Science (CMPMS) presented at the annual South African Institute of Physics (SAIP) Conference.

Goodfellow congratulates Dr Yousif on the hard work put in to receive the award, and wishes him every success for the future.



Dr A. Yousif (left). With him is Professor Japie Engelbrecht (NMMU Physics), Chairperson of the CMPMS (middle) and Professor Simon Connell, president of the SAIP (right).

The Goodfellow Award is the top honor bestowed by CMPMS at the South African Institute of Physics conference each year, and is funded by the Goodfellow Group of Companies, suppliers of high-quality metals, polymers, ceramics and other materials to universities and research facilities worldwide. It was first given at the SAIP conference in 2000, and is a tangible example of the company's commitment to recognizing and promoting talented young scientists.

For more information about Goodfellow, go to [www.goodfellow.com](http://www.goodfellow.com). For more information about the South African Institute of Physics, go to [www.saip.org.za](http://www.saip.org.za).

\* Dr A. Yousif, H.C. Swart, O.M. Ntwaeaborwa, *Surface state of  $Y_3(Al,Ga)_5O_{12}$ : Tb phosphor under electron beam bombardment*